WTe_2: Candidate for topological superconductivity

Inauguraldissertation

zur
Erlangung der Würde eines Doktors der Philosophie
vorgelegt der
Philosophisch-Naturwissenschaftlichen Fakultät
der Universität Basel

von

Martin Alexander Endres
aus Deutschland

Basel, 2022

Genehmigt von der Philosophisch-Naturwissenschaftlichen Fakultät
auf Antrag von
Prof. Dr. Christian Schönenberger
Prof. Dr. Patrick Maletinsky
Prof. Dr. Yoichi Ando
Prof. Dr. Thomas Schäpers

Basel, den 18.10.2022

Prof. Dr. Marcel Mayor
Dekan

Contents

1 Introduction

The invention of the classic computer constitutes largely the progress and prosperity of today. Its fundamental working principle relies on the conjunction of single bits that can either take the values 0 or 1. Ever more complex problems are addressed by up-scaling the number of bits on a computer chip, but an efficient time scale for obtaining a solution to complex problems remains a limiting factor [1]. As the famous physicist Richard Feynman pointed out [2], the crux lies in nature being based on probabilities. Rather than using a classic computer to calculate the probability for a configuration in a complex system, he proposed the solution to simulate nature with a computer that itself is based on probabilities.

Based on the laws of quantum mechanics, it is theoretically possible to build a quantum computer made up of quantum bits (qubits) that can accept the states $|0\rangle$ and $|1\rangle$ or any superposition of both [3]. A quantum computer is predicted to be highly superior to a classical computer for certain problems such as the factorization of numbers [1], as it is used in encrypting data, or simulating complex quantum mechanical systems, as for example in large molecules for the drug development [4].

The predicted impact of this novel form of computation has created a great interest in research for possible platforms to implement such a qubit, which fundamentally requires a quantum mechanical two level system. The research community and technology companies pursue the development of multiple systems in parallel, such as for example superconducting qubits, ion traps or spin qubits [5]. At this stage, it is not yet clear which technology will succeed if a universal winner can be determined at all. A common complication in the systems is the trade-off between coupling strength of single qubits to the external controls, which determines their operation speed, and the coherence of the quantum mechanical state, which is affected by the coupling to the environment [6]. While the number of physical qubits on a chip increases, the control of decoherence in the system becomes increasingly challenging and requires complex error correction codes with high redundancy and a large number of qubits [6, 7].

A promising alternative for a fault-tolerant computation platform could be provided by a topological qubit [8]. The field of topology is rooted in mathematics and aims to classify objects based on fundamental attributes that remain unimpaired, even if said object is smoothly deformed. Here, the quantum mechanical information is stored non-locally by elusive Majorana fermions, making it resilient against local perturbations [8]. Majorana fermions are no elementary particles but can emerge as excitations in a topological superconductor. While it remains up to debate if this superconducting pairing exists naturally, theoretical proposals have been developed to engineer such a state in various material platforms[9–13]. Additionally to the potential application of topological superconductors in quantum computation, they promise to extend our fundamental understanding of such exotic particles in solid state systems and superconductivity.

The focus of this thesis lies on the layered transition metal-dichalcogenide tungsten ditelluride WTe_2 and its potential role in engineering a topological superconductor. The material is proposed to be a higher-order topological insulator hosting gapless states along its crystal hinges [14–18]. Surprisingly, we find that the material turns superconducting when it is brought in contact to palladium, combining topology and superconductivity in a single, promising material platform. We use the effect to fabricate highly transparent Josephson junctions out of this material system, and we study the devices in transport measurements at cryogenic temperatures.

Outline of the thesis

We begin this thesis in the first half of Ch. 2 by introducing the theoretical concepts of superconductivity and Josephson junctions, followed by their implications for the following experiments. Special emphasis is placed on the current-phase relation and the conclusions that can be drawn from it about the electronic structure of the weak link material. The second half of the chapter is focused on the field of topology and the intriguing properties of WTe_2.

For each experiment we fabricate tailored devices, as described in Ch. 3, beginning with the exfoliation of bulk WTe_2 crystals followed by their processing by lithography to obtain functioning samples for low temperature transport measurements.

In Ch. 4 we present experimental proof that WTe_2 on palladium bottom contacts turns superconducting. We fabricate Josephson junctions to study the stability of the superconducting state in magnetic field and temperature.

Next, we build fully integrated tunnel junctions, using insulating hexagonal boron nitride (hBN) as a tunnel barrier in Ch. 5. Tunnelling spectroscopy on these devices allows the thickness dependent investigation of the novel superconducting state in WTe_2 on palladium and the results complement the understanding gained through the previous transport measurements.

Chapter 6 is dedicated to the origin of superconductivity in the material system. We find that palladium diffuses into the WTe_2 crystal, forming the superconducting compound $PdTe_x$. Based on this diffusion, we develop a fabrication technique to form highly transparent superconducting contacts to WTe_2.

The high quality contacts are used in Ch. 7 to embed WTe_2 into a superconducting quantum interference device (SQUID) with the goal to measure the current-phase relation. We find complex inductance effects that are attributed to $PdTe_x$ and that create excited vorticity states in the SQUID.

Finally, we finish the thesis in Ch. 8 with a summary of the data and an outlook for future experiments.

2 Introduction to superconductivity and WTe_2

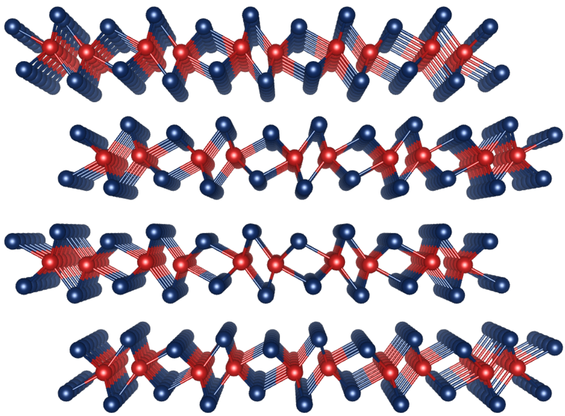

We start this chapter by introducing superconductivity and the Josephson effect as the basic concepts throughout the following thesis. In particular, we describe the current-phase relation of a Josephson junction as a unique device property that is governed by the transport of Cooper pairs across the junction weak link.

In the second part of the chapter, we examine the key ideas of topology and focus on the material system of choice in this thesis: the transition-metal dichalcogenide (TMDC) WTe_2. The material is proposed to be a higher-order topological insulator hosting topologically protected hinge states. The possibility to tune WTe_2 into a superconducting state make it an promising platform to study novel transport phenomena. We close this introduction by presenting the latest work of WTe_2 on palladium bottom contacts, forming the experimental basis for the following chapters.

2.1. Superconductivity

H. K. Onnes was the first to observe for certain materials that their electrical resistance vanishes below a material specific critical temperature T_c [19]. These materials are called superconductors and perfectly expel an external magnetic field B [20]. Phenomenologically, these two features, dissipationless transport and perfect diamagnetism, were first explained by the London theory [21, 22], which introduced the London penetration depth λ_L to which the magnetic field can enter the superconductor before being screened.

Later, the macroscopic nature of superconductivity was apprehended by Ginzburg and Landau [23] through a global wave-function $\Psi(\vec{r},t) = \sqrt{n_\mathrm{s}(\vec{r},t)}\, e^{i\theta(\vec{r},t)}$. Their theory introduced a characteristic coherence length ξ, on which Ψ can change, such as it is the case close to the surface of a superconductor or at the interface to a normal conductor. As a result, it was found that superconductors can be categorized as type I or II [24]. Superconductivity in type I materials breaks down sharply when an external magnetic field exceeds a critical value B_c. The phase transition in type II superconductors on the other hand proceeds continuously above the first critical field B_{c1}. In these materials, vortices that each carry a single flux quantum $\Phi_0 = h/(2e)$, penetrate the material until superconductivity breaks down at a higher critical field B_{c2}. Abrikosov realized that both phases could be distinguished by the ratio $\kappa = \lambda/\xi = 1/\sqrt{2}$, with $\kappa < 1/\sqrt{2}$ indicating type I superconductivity and $\kappa < 1/\sqrt{2}$ type II superconductivity [24].

Bardeen, Cooper and Schrieffer [25, 26] developed a microscopic theory for superconductivity that is based on an attractive electron-electron interaction mediated by the crystal lattice through phonons. Figure 2.1 a) illustrates the process, in which an electron in the state $|k_1, \sigma_1\rangle$ is scattered by a wave-vector q under emission of a phonon. The phonon is reabsorbed by a second electron in the state $|k_2, \sigma_2\rangle$ that is displaced in momentum by $-q$. The process creates bound electron pairs, in which the electrons have opposite momentum of the same magnitude. The so called Cooper pairs condensate into a common ground state around the Fermi energy E_F, called the BCS ground state. A direct consequence of the attractive interaction is the energy cost of 2Δ required to split up a Cooper pair. As a result, an energy gap emerges in the superconducting density of states $\mathcal{D}_\mathrm{S}$, as shown in Fig. 2.1 b), described by [22]

$$\mathcal{D}_\mathrm{S}(E) = \mathcal{D}_\mathrm{N}(E_\mathrm{F}) \frac{|E|}{\sqrt{E^2 - \Delta^2}} \Theta(E - \Delta) \tag{2.1}$$

with Θ being the Heaviside function and $\mathcal{D}_\mathrm{N}$ the normal state density of states. Excitations above the superconducting gap Δ are described as quasi-particles, which are a superposition of electrons and holes.

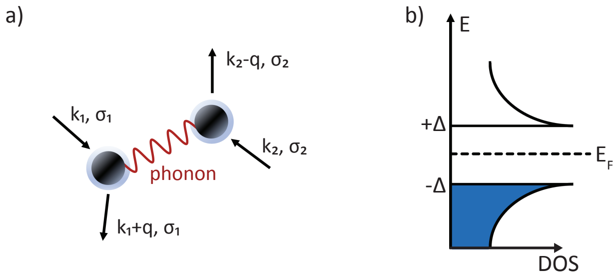

Figure 2.1. Cooper pair formation and gapped quasi-particle spectrum in BCS theory. a) Feynman diagram of two electrons bound as a Cooper pair. Panel a) adapted from Ref. [27]. b) Quasi-particle density of states (DOS) with Cooper pairs living at the Fermi energy E_{F}. The energy cost to split up a Cooper pair is 2Δ.

2.1.1. Josephson junctions

Brian D. Josephson [28] realized the importance of the phase parameter θ in the superconducting wave-function Ψ. Contrary to the belief of the time, Cooper pairs can tunnel between weakly coupled superconductors in a coherent process with significant probability. Devices in which this effect can be probed are called Josephson junctions (JJs). They consist out of two superconductors, connected by a weak link, which can be an insulator, a constriction or a conductor, as shown in Fig. 2.2 panels a) through c). Josephson predicted in his initial work for a superconductor-insulator-superconductor (S-I-S) junction that, even in the absence of a voltage difference between the two superconductors, a current

$$I(\varphi) = I_{\mathrm{c}} \ \sin(\varphi) \tag{2.2}$$

can flow across the junction. $I(\varphi)$ depends on the phase difference $\varphi = \theta_2 - \theta_1$ (compare Fig. 2.2 a)) between the superconducting contacts and the maximum supercurrent that can be carried by the JJ, the critical current I_c. Throughout this thesis, we use the Josephson effect and study in particular the phase dependence $I(\varphi)$ of Josephson junctions with WTe_2 as the weak link. In the following sections we examine how the current-phase relation changes depending on the weak link between the superconductors.

2.1.2. Andreev reflection

A fundamental aspect of a Josephson junction is the mechanism with which a current is transported across the N-S interface. An incoming electron with energy $|\varepsilon| < \Delta$, measured relative to E_{F} cannot enter the superconductor due

Figure 2.2. Josephson junctions. Different types of weak links connecting two superconductors: a) an insultor, b) a constriction or c) a conductor. Figure adapted from Ref. [29].

to the absence of available states. The electron has to be reflected back into the normal conductor.

The contradiction between the current across the N-S interface and the gapped density of states in a superconductor is overcome by the process of Andreev reflection. The incoming electron of energy ε is transferred across the interface into the superconductor together with a second electron of energy $-\varepsilon$, forming a Cooper pair. In order to fulfil charge and momentum conservation, the incoming electron is retro-reflected as a hole with energy $-\varepsilon$ and opposite momentum.

In reality, elastic scattering at the interface due to for example oxides, residues from the fabrication or lattice mismatch between different materials [30] have to be taken into account. A theory that includes such an imperfect interface has been developed by Octavio, Blonder, Tinkham and Klapwijk [31–33]. They have introduced a variable delta potential $V(x) = H\delta(x)$ of hight H at the N-S boundary to account for scattering. The interface transparency T can be connected to the scattering potential through $T = 1/(1 + Z^2)$, with $Z \equiv H/\hbar v_\mathrm{F}$ and v_F being the Fermi velocity of the scattered electron [30]. In case of a perfect transmission, the charge $2e$ is transferred across the N-S interface into the superconductor, doubling the conductance relative to the case when the superconductor is in the normal state.

2.1.3. Andreev bound states

Having introduced the transport across a single N-S interface, we extend the picture to a Josephson junction consisting of two superconductors that are connected by a normal conducting weak link of length l. An electron (e) impinging on the N-S interface is retro-reflected as a hole (h) that itself is retro-reflected at the opposite N-S interface as an electron. Through consecutive Andreev reflections, Cooper pairs of charge $2e$ are transferred between the two superconductors, as illustrated in Fig. 2.3 a). The confinement of the weak link gives rise to discrete Andreev bound states inside the superconducting energy gap, as illustrated in Fig. 2.3 b).

When an electron is Andreev reflected at the N-S interface, the retro-

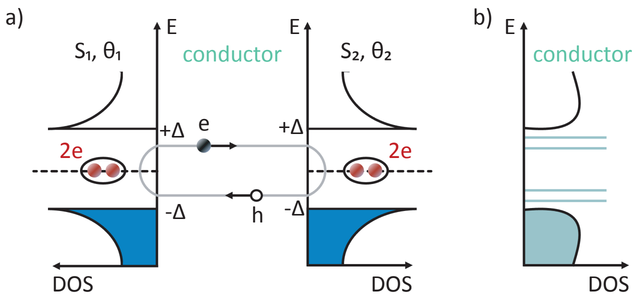

Figure 2.3. Emergence of sub-gap states in the weak link due to Andreev reflection. a) Charge carriers in the conducting weak link experience Andreev reflection at the N-S interface. If the accumulated phase of the charge carrier for a full cycle is equal to or multiple of 2π, stable bound states form in the weak link below the superconducting gap, as illustrated in b). Figure adapted from Ref. [34].

reflected hole acquires a phase $\phi_\mathrm{h} = \phi_\mathrm{e} - \arccos(\varepsilon/\Delta) + \theta$ [35], where ϕ_e and θ denote the phases of the incoming electron and the superconductor, respectively. The conjugate process takes place at the S-N interface where one electron of the Cooper pair fills a hole state and a second electron is transmitted into the normal conductor, gaining a phase $\phi_\mathrm{e} = \phi_\mathrm{h} - \arccos(\varepsilon/\Delta) - \theta$ [35].

For each full cycle through the junction, the accumulated phase has to fulfil the following condition for constructive interference [36]:

$$-2\ \arccos\left(\frac{\varepsilon_\mathrm{n}^{\pm}(\varphi)}{\Delta}\right) + (k_\mathrm{e}(\varepsilon^{\pm}) - k_\mathrm{h}(\varepsilon^{\pm}))l \pm \varphi = 2\pi n;\ n = 0, \pm 1, \pm 2, ... \quad (2.3)$$

The sign of ϕ depends on the initial condition of the electron moving to the left or to the right and $k_\mathrm{e} - k_\mathrm{h} \sim \frac{2\varepsilon}{\Delta\xi}$ [37].

The formation of bound states has an important implication, as it describes how a normal conductor can transport Cooper pairs dissipationless and coherently between two superconductors [38, 39].

In general, the Andreev bound state spectrum is highly dependent on the properties of the weak link. Macroscopic size effects of the junction determine the number and phase-dependence of sub-gap states while on a microscopic level, the contact transparency at the N-S interface and scattering mechanisms in the weak link have to be considered [40, 41]. These effects are reflected by interplay of the three length scales ξ, the electronic mean free path ℓ in the weak link and the junction length l. Depending on the ratio of ξ and ℓ relative to l the junction can be classified either to be in the short or long limit and further to be ballistic or diffusive [42], as summed up in table 2.1.

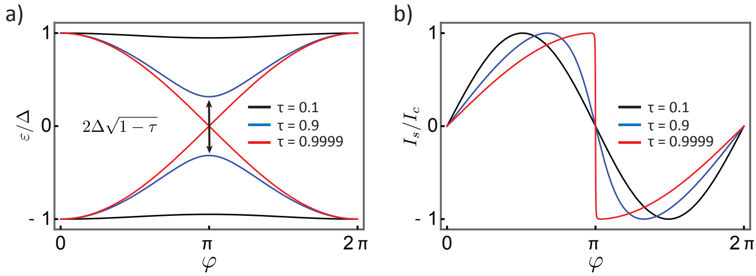

Figure 2.4. Andreev bound states in the short junction limit a) Sub-gap Andreev bound states for different channel transmissions τ. b) Supercurrent carried by each respective bound state through the junction.

	$l \ll \xi$	$l \gg \xi$
$l \ll \ell$	short ballistic	long ballistic
$l \gg \ell$	short diffusive	long diffusive

Table 2.1. Classification of Josephson junction regimes. The Andreev bound state spectrum is determined by the ratio of the junction length l relative to the superconducting coherence length ξ and the mean-free path ℓ.

Short junction limit

For $l \ll \xi$, Eq. 2.3 reduces to

$$\varepsilon^{\pm} = \pm\Delta\cos(\varphi/2) \tag{2.4}$$

and describes the formation of a pair of two-fold degenerate bound states per transverse mode inside the superconducting gap. In reality, the transmission probability $\tau \in [0, 1]$ per channel is usually assumed to be non-perfect, such that the energy spectrum is described by [37, 42, 43]

$$\varepsilon^{\pm} = \pm\Delta\sqrt{1-\tau\sin^2(\varphi/2)}. \tag{2.5}$$

Figure 2.4 a) plots the bound state spectrum as a function of phase difference φ for three different transmission probabilities τ. In the case of perfect transmission $\tau = 1$, the left and right moving electron states ε_+ and ε_- are degenerate at $\varphi = \pi$. When quasi-particle scattering is included through $\tau \neq 1$, the two energy levels are no longer independent, resulting in a pronounced anti-crossing behavior with an energy gap of $\delta = 2\Delta\sqrt{1-\tau}$ opening up at $\varphi = \pi$ [37].

Long junction limit

In the opposite limit of $l \gg \xi$, the energy spectrum becomes more complex. Additional bound states form inside the superconducting gap and the continuum states above the gap start to participate in current transport [37]. An approximate solution of Eq. 2.3 can be found when considering $l \ll \ell$ and small energies $\varepsilon \ll \Delta$. Using the approximations $k_\mathrm{e} - k_\mathrm{h} \approx k_\mathrm{F}\varepsilon/E_\mathrm{F}$ and $\arccos(\varepsilon/\Delta) = \pi/2$ [36] results in

$$\varepsilon^{\pm} = \frac{\hbar\nu_\mathrm{F}}{2l}[\pi(2n+1) \pm \varphi]. \tag{2.6}$$

While the number of bound states and the complexity increases compared to the short junction limit, the general characteristics, for example the influence of a finite channel transmission, remain the same as described before [36, 37, 41, 44, 45].

2.1.4. Current-phase relation

In transport measurements, the underlying physics of a JJ are accessible through the dependence of the supercurrent I_s on the phase φ, known as current-phase relation (CPR). Independent of the junction specifics, the CPR can be characterized by the following properties [46]:

1. The order parameter describing the superconducting contact does not change when the phase is forwarded by 2π and neither is therefore the supercurrent carried by the junction:

$$I_\mathrm{s}(\varphi) = I_\mathrm{s}(\varphi + 2\pi) \tag{2.7}$$

2. A change in supercurrent polarity is accompanied by a sign change in the phase difference between the contacts, implying that the CPR has to be an odd function:

$$I_\mathrm{s}(\varphi) = -I_\mathrm{s}(-\varphi) \tag{2.8}$$

3. Based on the first two arguments, the supercurrent vanishes when $\varphi = n\pi$,

$$I_\mathrm{s}(n\pi) = 0, \tag{2.9}$$

with $n \in \mathbb{Z}$.

As was shown in the previous section, an electron can enter the superconductor through the process of Andreev reflection and is coherently transported across the weak link by Andreev bound states. The contribution of each bound state to the supercurrent can be calculated via [47]

$$I_\mathrm{s}(\varphi) = \frac{ge}{\hbar}\frac{d}{d\varphi}\varepsilon(\varphi), \tag{2.10}$$

2

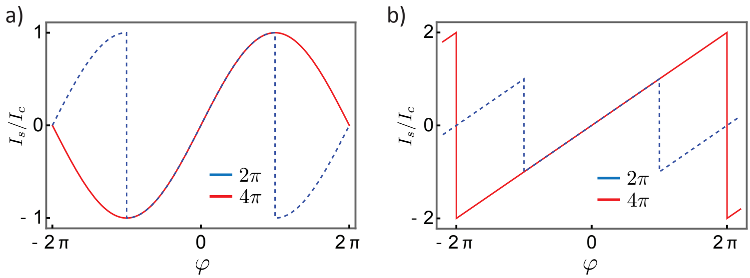

Figure 2.5. Current-phase relation of a topological Josephson junction. CPR of a trivial 2π periodic Josephson junction with transmission $\tau = 1$ (blue, dashed) and a 4π periodic topological Josephson junction in the a) ballistic short junction and b) long junction limit. Figure adapted from Ref. [47].

where $g = 2$ is accounting for the spin degeneracy. Figure 2.4 b) illustrates this connection for the short junction limit. Plotted is the supercurrent I_s, normalized to the critical current I_c of the junction, as a function of φ for the Andreev spectrum shown in a). In a short junction with N multiple channels, the resulting I_s can be calculated from [43]

$$I_\mathrm{s} = \frac{e\Delta}{2\hbar} \sum_{n=1}^{N} \frac{\tau_\mathrm{n} \sin(\varphi)}{\sqrt{1 - \tau_n \sin^2(\varphi/2)}}, \tag{2.11}$$

with τ_n being the transparency of the n^th channel. The direct connection between the CPR and the low-energy Andreev bound states has become a prominent tool to investigate the electronic properties of predicted topological materials [48–50]. We investigate the CPR of WTe_2/Pd JJs in Ch. 7.

The signature of a two-dimensional topological insulator are the helical edge states that reside along the boundary of the sample. They are protected against local perturbations, as long as time-reversal symmetry applies to the system. Ballistic transport through the weak link manifests itself in a prominent 2π-periodic saw-tooth CPR pattern. Figures 2.5 a) and b) plot the CPR of a JJ in the short and long junction limit, respectively, as a dashed line. The situation changes, if the helicity of the edge states is taken into account and superconductivity is successfully induced into the topological edge states [12]. In this case, not Cooper pairs with a flux periodicity of $h/2e$, equal to a phase change of $\varphi = 2\pi$, are shuttled across the weak link, but instead single electrons due to Majorana zero modes, which double the flux periodicity to h/e [47, 51, 52].

The result is a 4π-periodic CPR, as shown in Figs. 2.5 a) and b) as solid lines for the two junction regimes. Additionally, a distinct feature develops for the topological junction in the long limit, where the fermion-parity anomaly doubles the maximum current amplitude compared to the topologically trivial case [47].

Throughout the above discussion, the presented results were obtained in the limit of zero-temperature. An extension to finite temperatures can be found in Refs. [36, 43, 46, 53].

2.1.5. Interference effects through an applied magnetic field

The current-phase relation of a JJ can be measured in a superconducting quantum interference device (SQUID). A SQUID consists of two JJs embedded into a superconducting loop, as illustrated in Fig. 2.6 a). In the following section we introduce the concept of such devices in an applied magnetic field.

The supercurrent through a SQUID is a well defined quantity. In its previously defined form (compare to Eq. 2.2), φ is not gauge-invariant and cannot unambiguously determine I_s in an applied magnetic field. Gauge-invariance is introduced through [22]

$$\varphi = \theta_2 - \theta_1 - \frac{2\pi}{\Phi_0} \int \vec{A}\, d\vec{s}, \tag{2.12}$$

with $\vec{A}$ being the vector potential, $\vec{B} = \vec{\nabla} \times \vec{A}$, and $\Phi_0 = h/2e$ the flux quantum. The gauge-invariant phase differences $\varphi_{1,2}$ for the two junctions involved can be determined as [22]

$$\varphi_2 - \varphi_1 = \frac{2\pi\Phi}{\Phi_0} (\mathrm{mod}\ [2\pi]). \tag{2.13}$$

The integral over the vector potential is evaluated along a closed contour $\mathcal{C}$, indicated by the red dashed line in Fig. 2.6 a), and is equal to the enclosed flux Φ by the loop. The superconducting electrodes are assumed to be thicker than the London penetration depth λ_{L}, such that the current density inside the electrodes vanishes.

Using Eq. 2.13, the maximum supercurrent I_{c} through the SQUID is given by maximizing the sum of individual currents through the JJs with respect to φ_1 [54]

$$I_{\mathrm{c}}(\Phi) = \max_{\varphi_1} \left[I_{\mathrm{c}}^1 f_1(\varphi_1) + I_{\mathrm{c}}^2 f_2 \left(\varphi_1 + \frac{2\pi\Phi}{\Phi_0} \right) \right], \tag{2.14}$$

where $f_{1,2}(\varphi)$ denote the current-phase relations of the two JJs. In the case of $f_{1,2} = \sin(\varphi)$ and equal critical currents of the junctions $I_{\mathrm{c}}^1 = I_{\mathrm{c}}^2 \equiv I_{\mathrm{c}}^\star$, the maximum current through the SQUID is described by [22]

$$I_{\mathrm{c}}^{\mathrm{SQUID}} = I_{\mathrm{c}}^\star \left| \cos\left(\pi \frac{\Phi}{\Phi_0} \right) \right|, \tag{2.15}$$

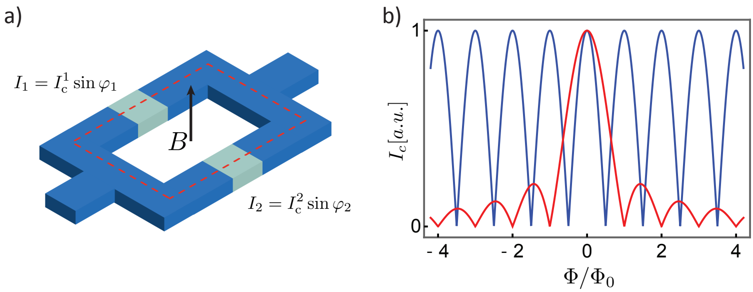

Figure 2.6. Interference effects in an applied magnetic field. a) Schematic illustration of a SQUID, consisting of two JJs embedded into a superconducting loop. The integration contour $\mathcal{C}$ is indicated by the red dashed line. b) Critical current I_c as a function of the applied flux Φ/Φ_0 for a SQUID (blue) and a single JJ (red) with sinusoidal CPR.

as shown in Fig. 2.6 b) in blue.

Following the same argument of a closed contour $\mathcal{C}$ as in the SQUID, the maximum supercurrent of a JJ with sinusoidal CPR is given by [22]

$$I_c^{JJ}(\Phi) = I_c^\star \left| \frac{\sin(\frac{\pi\Phi}{\Phi_0})}{\frac{\pi\Phi}{\Phi_0}} \right| . \tag{2.16}$$

The periodicity of the oscillations is set by the flux $\Phi = A_{JJ} \times B$ threading the junction, with $A_{JJ} = (l + 2\lambda_L) \times w$ being the effective junction area. Figure 2.6 b) plots the characteristic interference pattern in red, which is referred to as "Fraunhofer" pattern.

It should be noted that the above considerations have assumed a vanishing self-inductance of the superconducting loop, such that $\Phi_{tot} = \Phi_x$, with Φ_{tot} and Φ_x being the total flux and the externally applied flux through the loop, respectively. In case of a self-inductance L in the system, screening effects of the form $\Phi_{tot} = \Phi_x + LI_s$ have to be taken into account. Inductance effects can distort the CPR strongly but do not change its periodicity [22]. Such an inductive SQUID is studied in detail in Ch. 7.

2.2. Topological properties of WTe_2

A major achievement in solid state physics of the past century has been the classification of material classes according to broken symmetries [55, 56]. This concept was however revealed to be incomplete when von Klitzing *et al.* [57]

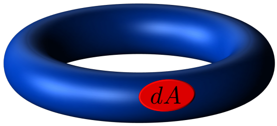

Figure 2.7. Representation of the Gauss-Bonnet formula. The geometry of the torus is directly related to its topology, classified by the integer number $g = 1$. Figure adapted from Ref. [63].

2

experimentally showed that a two-dimensional electron gas (2-DEG) in perpendicular magnetic field reveals a quantized conductance

$$\sigma_{\mathrm{xy}} = \mathcal{N} e^2/h \tag{2.17}$$

with $\mathcal{N}$ being the number of filled Landau levels, e the elementary charge and h the Planck quantum, respectively. The phenomenon is independent of minor device specifics and known today as quantum Hall effect. Indeed, the value $R_{\mathrm{K}} = e^2/h \approx 25.813\,\mathrm{k}\Omega$, established as the von-Klitzing constant, can be determined with such precision that it is used today as the resistance standard in metrology [58, 59].

A description of this novel state, and in particular its precisely quantized value, was achieved by transferring the mathematical concept of topology, a field that attributes every object to an invariant number based on its geometry, to solid state physics. A broadened review of this topic can be found in Refs. [55, 56, 60–62].

Within the following second half of the chapter we introduce the field of topology conceptually and present the TMDC WTe_2. We present the experimental signatures of a topological insulator and review the topological properties of WTe_2 with a focus on induced superconductivity in the material.

2.2.1. Introduction to topology

The goal of topology is to sort objects into equivalent classes, based on their properties that remain preserved under a smooth, i.e. adiabatic, deformation. Gauss and Bonnet stated [63, 64]

$$\frac{1}{2\pi}\int_S K dA = 2(1-g), \tag{2.18}$$

and proved through Eq. 2.18 a direct connection between the topology and the geometry of an object. While the integral of the curvature K over a surface S without boundary is not necessarily quantized, the right hand side of the Eq. 2.18 is. $g \in \mathbb{N}$ is an integer and denotes the number of holes in the object.

2

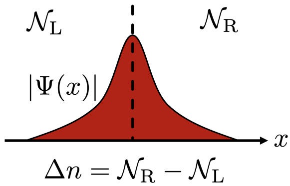

Figure 2.8. Bulk-edge correspondence. A change in topological invariant from $\mathcal{N}_L$ to $\mathcal{N}_R$ at an interface gives rise to conducting edge states, as the gap has to close and re-open between the two systems. Figure adapted from Ref. [65].

In the example of a torus, illustrated in Fig. 2.7, one finds $g = 1$, implying that the surface integral vanishes. Even if the object is deformed by compression or distortion, the topology of the surface S remains the same, as long as no additional holes are created or removed.

In solid state physics, the role of geometric surfaces is adopted by the band structure in reciprocal space [55, 56]. Following Bloch's theorem, the eigenvalues $E_m(\vec{k})$ of the Bloch Hamiltonian $\mathcal{H}(\vec{k})$ are connected to the crystal momentum $\vec{k}$. Two gapped systems, described by the Hamiltonians $\mathcal{H}$ and $\mathcal{H}'$, are considered topologically equivalent if it is possible to transform the initial $\mathcal{H}$ into the final $\mathcal{H}'$ adiabatically via [65]

$$\mathcal{H}(\alpha) = \alpha\mathcal{H}' + (1-\alpha)\mathcal{H}. \tag{2.19}$$

Thouless *et al.* [66] have shown that analogous to the argument of the geometric phase described by Eq. 2.18, similar classes of $\mathcal{H}$ can be categorized by a topological invariant called Chern number n. The Chern number can be related to the Berry phase, which the Bloch wave function $|u_m(\vec{k})\rangle$ picks up when $\vec{k}$ is moved around a closed path. Using the Berry connection $\mathcal{A}_m = i\langle u_m|\nabla_k|u_m\rangle$, the Chern number is connected to the Berry flux $\mathcal{F}_m = \nabla\times\mathcal{A}_m$ through the integral

$$n_m = \frac{1}{2\pi}\int \mathcal{F}_m d^2\vec{k} \tag{2.20}$$

over the complete Brillouin zone [56]. The summation over all N occupied bands

$$n = \sum_{m=1}^{N} n_m \tag{2.21}$$

yields the total Chern number and is equal to the integer $\mathcal{N}$ from Eq. 2.17 [66].

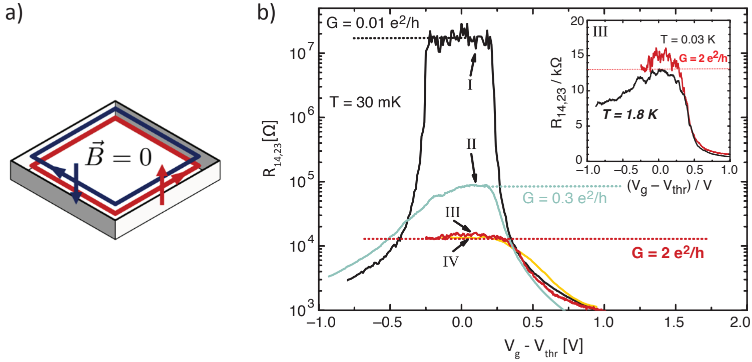

Figure 2.9. Signatures of a two-dimensional topological insulator. a) A two-dimensional topological insulator (TI) remains insulating in its bulk while hosting helical edge states at its boundary where the topological invariant changes. In comparison to the QHE, no external magnetic field $\vec{B}$ is required for the quantum-spin Hall effect (QSHE). b) Experimental signatures of a TI in a transport measurement, displaying the in the presence of helical edge states expected quantized conductance value $G = 2e^2/h$ for devices labelled III and IV. Panel b) adapted from Ref. [69].

The topological classification of the band structure has a direct consequence for an interface between two gapped systems where the topological invariant changes by $\Delta n = \mathcal{N}_\mathrm{R} - \mathcal{N}_\mathrm{L}$. Figure 2.8 illustrates such situation at the interface between two systems classified by the topological invariants $\mathcal{N}_\mathrm{L}$ and $\mathcal{N}_\mathrm{R}$. As it is not possible to transfer $\mathcal{H}$ into $\mathcal{H}'$ adiabatically without closing the band gap, conducting edge states emerge at the interface as the gap closes and re-opens. The number of edge states is directly related to the topological properties of the bulk, a phenomenon known as bulk-edge correspondence [55, 56].

The first discovered quantum Hall effect carries chiral edge states and requires a large external magnetic field that breaks time-reversal symmetry explicitly. The field of topological materials gained momentum when two groups, Kane *et al.* [67] and Bernevig *et al.* [68], predicted independently the existence of topologically protected edge states in materials without the need for an externally applied magnetic field. The so-called quantum spin Hall (QSH) effect is time-reversal invariant and was proposed to exist in certain two-dimensional materials with strong spin-orbit coupling. It established the novel material class of topological insulators (TI).

Shortly after, mercury-telluride (HgTe) quantum wells were predicted [70] and found experimentally to be a two-dimensional TI [69]. Figure 2.9 a) illustrates the two counter propagating, spin-polarized helical edge states [67, 68, 71] that emerge at the boundary of the sample [72], the signature of the QSH effect[1]. Experimentally, the QSH effect manifests itself by quantized conductance plateaus that develop when the Fermi energy is placed inside the gap. Transport is then governed by the helical edge states that carry a resistance quantum $R_{\mathrm{K}} = e^2/h$ each, as shown in the initial paper by König *et al.* [69] in Fig. 2.9 b). A conductance plateau at $G = 2e^2/h$ develops in the small samples III ($(1.0 \times 1.0)\ \mu\mathrm{m}^2$) and IV ($(1.0 \times 0.5)\ \mu\mathrm{m}^2$) that matches the the expected value of two helical edge states in given contact configuration [74].

It should be noted that topological insulators are not restricted to two dimensions, but were predicted [75] and experimentally observed [76–80] also in three dimensions, with conducting surface states developing at the material boundary. The interested reader is referred to references [60, 73] for a detailed introduction.

Originally, the topological classification was thought to be only applicable to systems with a band gap. It was only found recently that topologically protected states can emerge also in gapless systems [81–84], with Weyl semimetals [85, 86] as an example. In crystals with either broken time-reversal or inversion symmetry [81], sets of topologically protected Weyl nodes are connected by conducting surface states, named Fermi arcs, that appear in parallel to the bulk states.

2.2.2. Topological superconductivity

In analogy to a topological insulator, the concept of topological classification of gapped band structures can be transferred to the superconducting state [87–89]. Here, the superconducting gap assumes the role of the energy gap of the band insulator, and it is possible to describe the system by an analogous Bogoliubov-de Gennes Hamiltonian [55]. Following the bulk-edge correspondence, the dimensionality and topological classification of the superconducting state determine the existence of gapless excitations at the interface to a topologically different material.

The present research interest is focused in particular on time-reversal breaking topological superconductors that are predicted to host Majorana zero modes as their zero-energy excitations [55]. Majorana fermions are predicted to be the building block for fault tolerant quantum computing, due to their non-Abelian statistics and the possibility to store information nonlocally [90]. In contrast to the standard s-wave pairing in trivial superconductors, the emergence of unpaired Majorana fermions requires a spinless topological superconductor with complex $p_{\mathrm{x}} + ip_{\mathrm{y}}$ pairing [91]. Such systems were studied for

[1] The vacuum state is considered a trivial insulator with an energy gap equal to the energy cost of creating an electron (in the conduction band) - positron (in the valence band) pair [73].

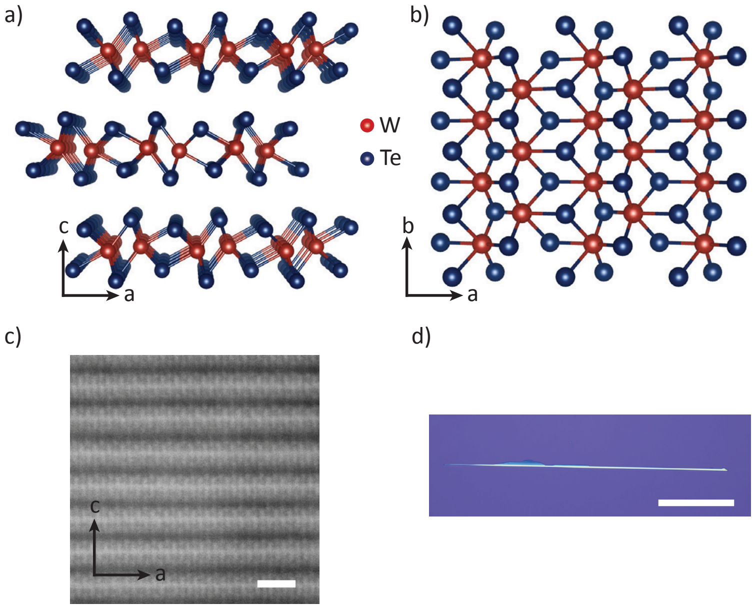

Figure 2.10. WTe_2 crystal structure. a) Td crystal phase of WTe_2 displayed in the ab-plane and b) ac-plane, respectively. c) Scanning transmission electron microscopy (STEM) image of a WTe_2 crystal, with single vdW-layers visible. Scale bar is 1 nm. d) Optical image of an exfoliated WTe_2 crystal with a pronounced needle shape as it is used in the experiments. The scale bar is 50 µm.

example by Kitaev [51] and Read *et al.* [92] in one- and two-dimensions, respectively, with Majorana zero modes residing at the ends of a one-dimensional wire and the center of vortex cores. While it is still under debate if such a pairing state exists naturally, several theoretical approaches have been developed to engineer it artificially.

A potential recipe relies on the finely tuned interplay of spin-orbit coupling, superconductivity and magnetism. It was predicted, that Majorana fermions could emerge in platforms of one-dimensional nanowires [9–11] or topological insulators [12, 13] that are proximitized by an s-wave superconductor.

2.2.3. Crystal structure of WTe_2

WTe_2 belongs to the material class of layered TMDCs that are characterized by the stoichiometry MX_2, where M denotes the transition metal and X the chalcogenide. The majority of TMDCs crystallizes either in the 1H structure, with single layers of the form X-M-X [93], stacked in Bernal fashion ABA [94], or the 1T structure [93], in which M atoms are aligned octrahedrally due to a shift of one X layer, resulting in a rhomboedral stacking ABC [94].

WTe_2, in contrast, stabilizes in the Td phase [93, 95] with space group $Pnm2_1$, a distorted form of the T phase, shown in Fig. 2.10 a) and b) for two different crystal orientations. Tellurium (Te) atoms surround the tungsten (W) atom in a buckled octahedron configuration with its center in the a-b plane [96]. Single layers are stacked on top of each other along the c-axis of the crystal. The layered van der Waals (vdW) structure of the single layers is well visible in scanning transmission electron microscopy (STEM) image presented in Fig. 2.10 c). A detailed summary of crystallographic parameters can be found in [97].

The Td structure further constitutes the semi-metallic nature of WTe_2 as it lowers the Madelung energy compared to a hypothetical 1H structure of the same material [93, 98]. Electronic bandstructure calculations have shown that electron and hole concentrations in transport participating bands are close to perfectly compensated and they are responsible for the observed non-saturating magneto-resistance [98, 99]. In experiment, this signature is often used as a indicator for high quality crystals. In this thesis, we use WTe_2 crystals that were grown by the flux method and are oriented along their crystallographic a-axis [100], as shown in Fig. 2.10 d).

2.2.4. Hinge modes in few layer WTe_2

The TMDC WTe_2 has intriguing topological properties that can vary depending on the crystal's thickness or its orientation relative to the current transport direction [101].

Bulk crystals of WTe_2 belong to the novel class of type-II Weyl semi-metals [102, 103] and display a large non-saturating magneto resistance [99]. Thinned down to a mono layer, the material was found to be a two-dimensional TI [104–107], with an extraordinary stability of the quantized conductance up to a temperature of T =100 K, in agreement with an observed inverted energy gap between 45 meV [108, 109] and 100 meV [110].

Further, bulk WTe_2 has recently been predicted [14–16] to belong to the novel class of higher-order TIs. Schindler *et al.* [17] and Benalcazar *et al.* [18] extended the class of three-dimensional TIs by realizing that a TI of dimension d and order n can hold (d-n)-dimensional topological protected hinge or corner states. Depending on the symmetries of the system, these states can be of

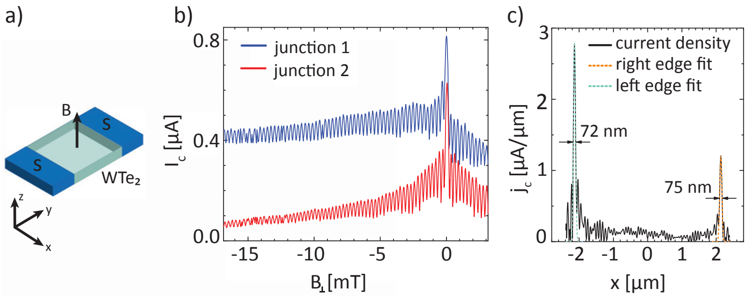

2

Figure 2.11. Signatures of edge transport in the predicted higher-order TI WTe_2. a) Illustration of a Josephson junction with WTe_2 as the weak link. b) Critical current I_c versus perpendicular magnetic field $B_\perp$ of two different Josephson junctions. Visible are fast oscillations that decay only slowly with increasing field amplitude. The interference pattern can be related to the current density j_c in c) via a Fourier transformation. $j_c(x)$, with x being the space coordinate as indicated in a), appears to be highly localized along the edges of the sample. Panels b) and c) adapted from Ref. [111].

chiral or helical nature.

Experimentally, signatures of conducting edge states, residing at crystal step edges, were found in scanning tunneling microscopy (STM) [15]. A second type of experiment, designed to detect signatures of hinge states, has incorporated WTe_2 as a weak link between two superconducting electrodes into a Josephson junction geometry, as illustrated in Fig. 2.11 a). Placed in a perpendicular magnetic field, the devices studied by Kononov *et al.* [111] show fast oscillations of the critical current I_c that decay only slowly in amplitude with increasing magnetic field. The interference pattern of I_c can be related to the current density j_c inside the junction [112] and is found to be highly localized at both crystal edges. Agreeing results have been obtained by Refs. [16, 101].

2.2.5. Emerging superconductivity in WTe_2

Additionally to its topological properties, WTe_2 was shown to enter the superconducting state when subjected to high pressure [113, 114] or when heavily doped during growth [115]. Mono layer crystals were reported to turn superconducting when the electron density in the material is tuned by an electrical gate above a critical value $n_{\mathrm{e,\,crit}} \sim 5 \times 10^{12}\,\mathrm{cm}^{-2}$ [116, 117]. Further, Kononov *et al.* [111] have shown in their experiment that the material combination of WTe_2 on palladium (Pd) bottom contacts reveals superconductivity when cooled below a critical temperature $T_c \sim 1.2\,\mathrm{K}$.

The above experiments have established WTe_2 as a material with rich topology that presents itself as a platform for novel transport phenomena. In combination with the observed superconductivity it is a promising candidate to host topological superconductivity.

3 Device fabrication

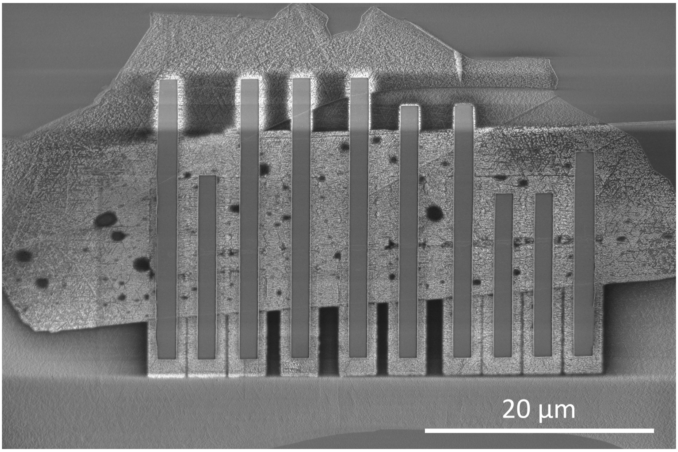

The chapter is focused on the fabrication of van der Waals heterostructures. We begin with the description of the exfoliation process to thin down bulk crystals to the thickness of only a few layers. Afterwards, single flakes can be picked up and stacked on top of each other to form the heterostructure. The process is concluded by electron-beam lithography to deposit on-chip superconducting elements and connect the sample to the measurement setup.

3.1. The prosperous possibilities of van der Waals heterostructures

The field of vdW materials was famously set off by graphene: a single atomic layer of carbon atoms, aligned in a hexagonal lattice [118]. Ever since, a large variety of 2D materials has moved into focus of research [119–121], covering a wide range of electronic properties ranging from insulating to superconducting [122]. Beside the possibility to study thickness dependent phenomena in the materials [123–126], the great potential of this material class lies in the possibility to stack different vdW crystals on top of each other, forming heterostructures with novel properties. This approach of close fabrication control has in recent years been extended by the unique possibility to twist single vdW layers relative to each other, resulting in large superlattice structures that give rise to correlated physics phenomena [127–130].

In the following chapter we describe the fabrication process of the vdW heterostructures used in this thesis. We begin with the preparation of palladium bottom contacts, followed by the exfoliation of WTe_2 and hexagonal boron-nitride (hBN) crystals. We continue to outline the stacking process and the following electron-beam (e-beam) lithography. A detailed description of all fabrication parameters and recipes can be found in appendix A.

3.2. Preparation of Pd bottom contacts

Palladium (Pd) bottom contacts are fabricated on a p-doped silicon wafer with 285 nm SiO_2 layer on top. This type of wafer is used throughout the complete fabrication process and is referred to as Si/SiO_2 wafer. The structure is written via e-beam lithography, followed by metal deposition in an e-beam evaporator of 3 nm titanium (Ti) and 15 nm Pd. The lift-off of excess metal is done in acetone at 50 °C for 1 hour.

3.3. Exfoliation

At the beginning of every device fabrication lies the mechanical exfoliation [118] of bulk crystals down to the desired thickness of several layers. Cleavage of the bulk crystals along single layers is possible due to strong covalent in-plane bonds, while layers on top of each other are held together weakly by van der Waals forces [119]. The devices presented in this thesis consist of the two vdW materials, hBN and WTe_2. While hBN remains inert under ambient conditions, WTe_2 is prone to oxidation [131–133] and requires handing in an inert N_2 atmosphere of a glovebox until it is fully encapsulated and protected from the ambient atmosphere by hBN.

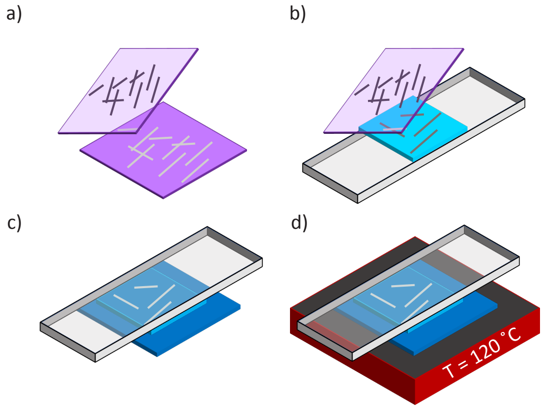

Figure 3.1. Exfoliation process of WTe_2. a) Needle-shaped bulk WTe_2 crystals are mechanically exfoliated via an adhesive tape. b) Once a uniform coverage is obtained, one half of the tape is brought in contact with a PDMS stamp, pushed down and quickly peeled off. c) The PDMS stamp with WTe_2 flakes is brought in contact with the Si/SiO_2 substrate and d) is heated for at 120 °C for 5 min.

hBN is exfoliated in ambient conditions on untreated Si/SiO_2 wafers using adhesive tape. Suitable flakes with a thickness between 10 nm and 30 nm are selected via optical contrast under the microscope [134] and are checked to be uniform in dark-field mode.

Next, we use flux grown WTe_2 crystals with a needle shape that are preferably oriented along their crystallographic a-axis [100]. The process begins with cleaning Si/SiO_2 wafers for 5 minutes in a 30 W oxygen plasma and quickly transferring them into the glove-box. The crystals are exfoliated using adhesive tape which is pressed onto a polydimethylsiloxane (PDMS) stamp, as shown in Fig. 3.1 a) and b). This additional step, compared to the standard hBN exfoliation, was included because we experienced that WTe_2 crystals shatter into small fragments when the adhesive tape is placed directly on the Si/SiO_2 substrate. After quickly separating the PDMS from the adhesive tape, the stamp is brought in contact with the Si/SiO_2 substrate (Fig. 3.1 c)) and the package is placed on a hotplate at 120 °C for 5 minutes (Fig. 3.1 d)). After a cool down time of $\sim$ 15 minutes, the PDMS is peeled off from the substrate and fitting flakes of needle shape and thickness between 10 nm and 30 nm are selected using their optical contrast and dark field imaging.

3.4. Stacking of vdW layers

After all vdW materials are exfoliated and proper flakes for the experiment selected, the single flakes can be stacked on top of each other to form the vdW heterostructure. As mentioned before, this technique allows to systematically engineer novel device properties by combining materials with different characteristics on top of each other. Furthermore, encapsulating the vdW heterostructure with hBN was shown in case of graphene to greatly enhance the mobility [136, 137], protect the device from unintended doping by adsorption of water molecules or similar residues from the fabrication process [138–140]. For the present case of WTe_2, hBN encapsulation is additionally used to protect the active transport layer from oxidation [131–133].

In our fabrication process, we have adapted the dry transfer technique [137, 141]. In the following sections we outline the basic concepts of this fabrication technique.

3.4.1. Preparation of the polymer transfer stamp

In order to stack single flakes on top of each other, they have to be picked up and precisely aligned with respect to each other by a polymer transfer stamp. Fabrication begins with coating a glass slide with a polycarbonate (PC) film, as shown in Fig. 3.2 a). An adhesive tape, illustrated in blue in Fig. 3.2 b), in which a cut out window has been prepared, is pressed onto the PC film and used to lift off a small, suspended patch that is then placed on top of a small PDMS pad on top of a glass slide, illustrated in Fig. 3.2 c). The layered structure is fixed to the glass slide by adhesive tape.

The role of the soft PDMS pad is to absorb mechanical shear forces during the stacking process in order to keep the brittle flakes intact, while the adhesive PC film is used to pick up the vdW materials.

3.4.2. Pick-up process of single flakes

Using the glass slide, the readily prepared stamp is mounted upside-down onto the remotely controlled stacking apparatus inside the glovebox. PDMS and PC are translucent, allowing to look with a microscope through the stamp on the flakes underneath and coordinate the stacking procedure. As the entire stacking takes place inside the glovebox, the movement of all mechanical elements involved is electronically controlled from outside, guaranteeing a high level of precision in the process.

The substrates containing the previously selected flakes are placed on a heatable stage underneath the stamp, that can move in (x, y)-direction and rotate freely. The stamp is mounted under a small angle relative to the substrate on a mechanical arm that allows the movement in (x, y, z)-direction. The small

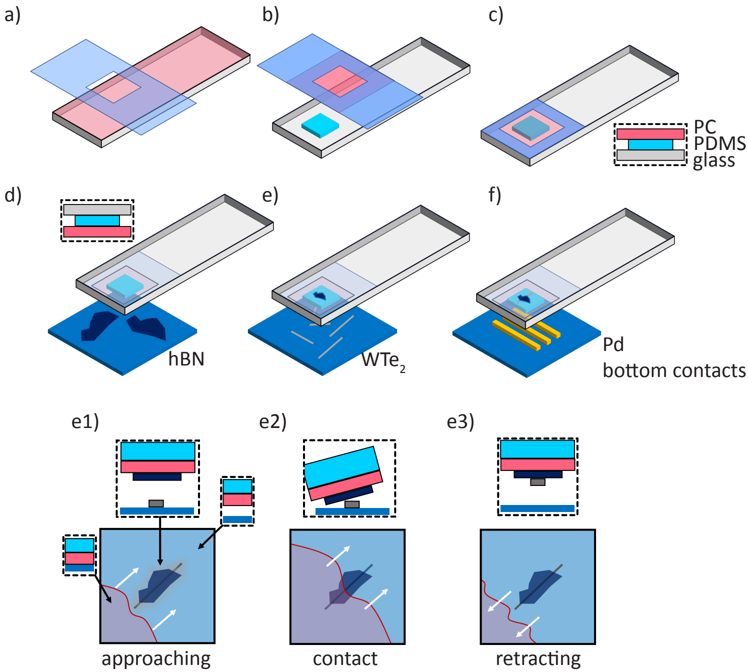

Figure 3.2. Stacking process of the vdW heterostructure via the dry transfer method. Preparation of the polymer stamp begins with a) the coating of a glass slide with a PC film. b) A small patch of the PC film is cut out and c) transferred on top of a PDMS pad. The finished stamp is used to pick up successively d) the selected hBN and e) WTe_2 flakes. In order to pick up a flake, the PC stamp is brought carefully in contact with the heated substrate under a small angle. The contact zone (red) in e1) is slowly driven (e2) over the flake that is thought to be picked up until the flake is fully enclosed by the contact zone. The stamp is then slowly lifted up from the substrate, such that the contact zone retracts (e3) while the flake sticks to the stamp. f) Once all vdW layers have been picked up, the stack can be deposited onto the prepatterned Pd bottom contacts. Figure adapted from Ref. [135].

angle $\sim 1°$ - $2°$ enables a slow and controllable movement of the interface between PC and the substrate in the (x, y)-plane as the stamp is moved in z-direction. During the stacking process, the stage is heated to $T = 80\,°\mathrm{C}$ and kept there constantly.

The pick-up of single flakes is initiated by placing the stamp over a selected flake (Fig. 3.2 d)) and lowering it until the stamp makes contact with the substrate, as illustrated in Fig. 3.2 e1) by the red area in the bottom left corner. The contact zone is then slowly pushed forward by continuously lowering the stamp, until it encloses the selected flake completely (e2)). After residing in this contact position for a few minutes, the pick-up is started by rising the stamp and therefore retracting the contact zone. The flake is peeled off the substrate and sticks to the PC film or vdW flake (depending on the process step in the procedure) due to stronger adhesion or vdW forces compared to the adhesion to SiO_2, respectively.

3.4.3. Deposition of the stack on the bottom structure

When all successive layers have been picked up, the finished vdW stack can be placed on top of the prepared Pd bottom contacts, shown in f). We follow the method of Purdie *et al.* [142], by heating the stage with the bottom structure to T=120 °C before it is getting in contact with the stamp. Next, the stack is aligned with the Pd bottom structure before contact is initiated between the stamp and the substrate, such that the stack does not touch the leads, yet. The temperature of the stage is increased to T=155 °C, the maximum temperature possible at the setup, and thermal expansion of the PDMS is used to drive the contact zone between stamp and substrate slowly over the bottom contacts and to deposit the stack. The increased heat and the slow crawling speed with which the stack moves over the bottom contacts push encapsulated residues out from the vdW layers towards the edges of the stack and result in clean interfaces. Once the stamp is fully in contact with the substrate and the vdW stack is deposited, the system is kept in contact at maximum temperature for $\sim 10\,\mathrm{min}$.

At T=155 °C, PC begins to melt and firmly sticks to the substrate surface. The stamp is slightly lifted from the substrate, detaching the PC film with the vdW stack from the PDMS pad. Through careful (x, y, z)-motion of the stamp relative to the substrate, the film is ripped and separated from the stamp. The melted PC film remains behind on the substrate and covers the vdW heterostructure and Pd bottom contacts.

3.4.4. PC residue removal

At this point, WTe_2 is fully encapsulated by hBN and safe to be taken out of the inert N_2 atmosphere. Remaining PC residues on top of the stack are dissolved for 1 h in dichloromethane at room temperature.

3.5. Electrical contact to the device

In order to conduct electrical transport measurements, contacts to the heterostructure have to be made that form the connection to the measurement setup. Depending on the experiment, we use normal metallic or superconducting contacts that are patterned with standard electron beam (e-beam) lithography.

Normal contacts

After patterning the contact structure via e-beam lithography on top of the Pd bottom contacts, a sticking layer of $\sim 5\,\text{nm}$ titanium (Ti), followed by $\sim 100\,\text{nm}$ gold (Au) is deposited in a e-beam evaporator.

Superconducting contacts

Patterning of the contact design is conducted analogue to the normal metal contacts via e-beam lithography. However, the superconducting contact has to be made directly to the WTe_2 flake and the hBN flake on top has to be removed. We use an etching step in an reactive ion etcher (RIE) with CHF_3/O_2 to expose the bare WTe_2 crystal. Before sputtering the superconductor niobium (Nb) or molybdenum-rhenium (MoRe) as contact material, a short argon (Ar) plasma is ignited inside the sputtering machine itself to clean the contact area and remove potential oxides that might have formed during the transfer of the sample between machines. The contacts are made by either $\sim 100\,\text{nm}$ sputtered Nb or MoRe. Alternatively to the sputtering process, aluminium (Al) with a same thickness is evaporated in a separate e-beam evaporator, including a similar Ar plasma cleaning before deposition of the material.

In all cases, the excess metal is removed in a lift-off process in warm acetone at T=50 °C.

4 Superconducting properties of WTe_2 on palladium normal contacts[1]

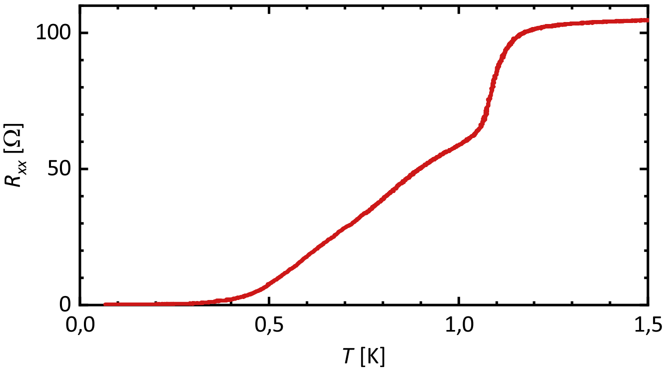

In Sec. 2.2.4 we have briefly introduced the phenomenon of WTe_2 turning superconducting when the crystal is brought in contact with palladium contacts. This effect makes WTe_2 a promising platform for topological superconductivity as it combines topological properties with superconductivity in a single material system. In the following chapter we characterize the properties of the emerging superconducting state by investigating its stability in elevated temperature and magnetic field.

[1] This chapter has been published in similar form in A. Kononov, M. Endres *et al.*[143]

4.1. Introduction

Topological superconductors are subject to extensive research interest due to their prospective application in fault-tolerant topological qubits [8]. A potential route to engineer such a novel pairing state in a superconductor was predicted by Fu *et al.* [12] by proximitizing a topological insulator to a normal s-wave superconductor. This proposal drives the fascination in hybrid structures of topological materials, such as WTe_2, and superconductors.

It is therefore of great interest, that WTe_2 on palladium bottom contacts was found to turn superconducting [111] as it combines these two fundamental states of matter in a single material system. Several novel states of topological superconductivity have been proposed theoretically on the basis of proximitized Weyl and Dirac materials. They include Fulde-Ferrell-Larkin-Ovchinnikov superconductors [144–146], chiral non-Abelian Majorana fermions [147] and time-reversal invariant topological superconductors [148].

4

In the following chapter we present the emerging superconductivity at the interface between WTe_2 and palladium bottom contacts. The main focus is placed on characterizing the fundamental superconducting properties in this material system by means of transport experiments.

4.2. Emerging superconductivity in WTe_2 on palladium contacts

We begin with the fabrication of vdW stacks on palladium (Pd) bottom contacts, as described previously in Ch. 3. Figure 4.1 displays an optical image of the finished sample. An elongated WTe_2 flake with high aspect ratio is aligned with the vertical Pd bottom contacts in the center and is encapsulated by a thin hBN on top, visible by a faint blue contrast through the image. The contact configuration resembles that of a standard Hall-bar, and the longitudinal resistance $R_{\mathrm{xx}} = V_{\mathrm{xx}}/I$ is measured as indicated by the schematics. The sample is sourced by a current I while the voltage V_{xx} is measured in four-terminal configuration.

Figure 4.2 a) shows the measurement of R_{xx} as a function of perpendicular magnetic field $B_\perp$ at a temperature of the cryostat $T = 4\,\mathrm{K}$. $\mathrm{R_{xx}}$ does not saturate up to high magnetic fields [99], which is an indicator of high quality of the crystal [149]. The small magneto-resistance is given by the thin WTe_2 crystal (7 layers) [150]. Another evidence for high quality of our samples is provided in Fig. 4.2 b) which shows the presence of Shubnikov–de Haas oscillations developing at low temperature. The frequency of the oscillations $f_{1/\mathrm{B}} \sim 100\,\mathrm{T}$ corresponds to an electron density $n_{\mathrm{2D}} = e/(\pi\hbar f_{1/\mathrm{B}}) \sim 5 \times 10^{12}\,\mathrm{cm}^{-2}$ and a Fermi wavevector $k_{\mathrm{F}} = \sqrt{\pi n_{\mathrm{2D}}} \sim 0.4\,\mathrm{nm}^{-1}$. In this calculation, the two electron pockets of WTe_2 have been taken into account [150]. The on-

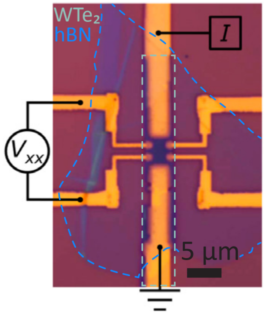

Figure 4.1. Optical image of sample with an illustration of the measurement scheme. Pd bottom contacts are reaching from outside the image into the center. A WTe_2 flake is placed on top in vertical orientation. A faint blue shade is discernible around the center of the image, belonging to the thin hBN flake that covers the WTe_2 crystal and protects it from oxidation.

set of oscillations around $B_\perp \sim 5\,\mathrm{T}$ suggest a carrier mobility of at least $\mu > 1/B \sim 2000\,\mathrm{cm^2\,V^{-1}\,s^{-1}}$ [151], corresponding to an electron mean free path of $\ell = k_\mathrm{F}\hbar\mu/e \sim 50\,\mathrm{nm}$.

At low temperature, additional features develop in $R_\mathrm{xx}(B_\perp)$, as shown in Fig. 4.3 a): at zero field, the resistance goes to zero, while at small fields, it transitions to an intermediate state that lies in between the low- and high-temperature values. $R_\mathrm{xx}(B_\perp)$ is hysteretic with the sweep direction. The feature is connected with the heating effects in the system during magnetic field sweeps as it can be reduced by lowering the sweep rate.

The intermediate resistance state in Fig. 4.3 a) is a result of the formation of a superconducting state in WTe_2 above the Pd leads. Furthermore, these superconducting regions could be connected by the Josephson effect, as illustrated in Fig. 4.3 b), leading to a zero longitudinal resistance. The zero resistance state appears only for smaller distances between the contacts, excluding therefore intrinsic superconductivity in our WTe_2 samples. This explanation is further supported by the measurement of the $R_\mathrm{xx}(T)$ dependence in Fig. 4.3 c). With decreasing temperature, the first transition takes place in the range of $1.05\,\mathrm{K}$ - $1.2\,\mathrm{K}$ when WTe_2 on top of Pd turns superconducting, followed by the steady decrease in resistance down to $\sim 350\,\mathrm{mK}$ when the Josephson effect emerges and zero resistance is observed.

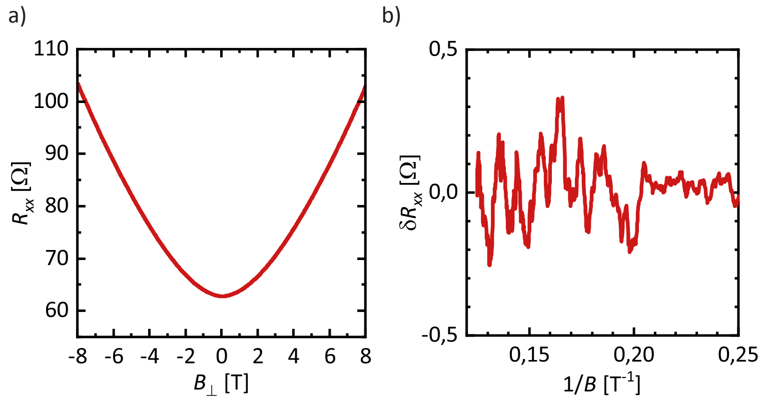

4

Figure 4.2. Signatures of high crystal quality. a) Characteristic non-saturating magneto-resistance $R_{\mathrm{xx}} = V_{\mathrm{xx}}/I$ in perpendicular magnetic field $B_\perp$ at 4 K. b) Onset of Shubnikov-de-Haas oscillations above $B_\perp \sim 5$ T. The data was obtained through subtraction of the quadratic background from the magneto-resistance data acquired at $T = 60$ mK.

4.3. Critical magnetic field B_{c2}

A fundamental property of a superconductor is the expulsion of a magnetic field from its inside up to a critical field strength B_{c}, known as Meissner-Ochsenfeld effect.

In order to characterize the superconducting state further, we study the evolution of $R_{\mathrm{xx}}(B_\perp)$ with increasing temperature, as shown in Fig. 4.4 a). Upon temperature increase, both transitions in the resistance are shifting towards zero field. The zero resistance state connected to the Josephson coupling disappears first above 0.75 K, and the second transition connected to the suppression of superconductivity by magnetic field B_{c2} persists up to 1.1 K. We define $B_{\mathrm{c2}}(T)$ as the magnetic field where $R_{\mathrm{xx}}(B_\perp)$ crosses the fixed resistance value $R_{\mathrm{xx}} = 45\,\Omega$, which approximately corresponds to half of the resistance step. Figure 4.4 b) shows the extracted dependence of the critical magnetic field as a function of temperature T. The $B_{\mathrm{c2}}(T)$ dependence is linear as expected for a 2D superconductor [22],

$$B_{\mathrm{c2}}(T) = \frac{\Phi_0}{2\pi\xi_{\mathrm{GL}}^2}\left(1 - \frac{T}{T_{\mathrm{c}}}\right), \tag{4.1}$$

with $\Phi_0 = h/2e$ being the magnetic flux quantum, ξ_{GL} the Ginzburg-Landau coherence length at zero temperature and T_{c} the critical temperature

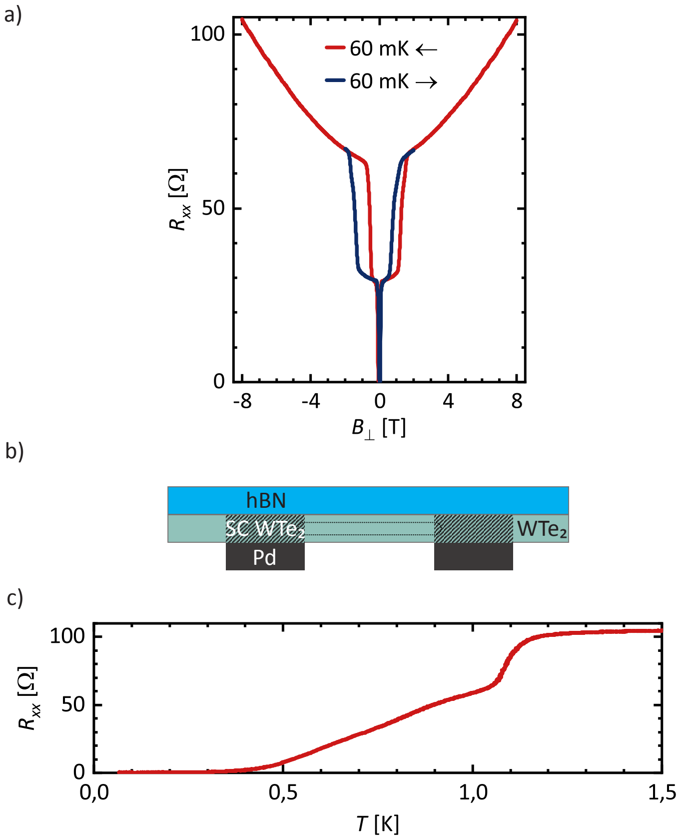

Figure 4.3. Superconductivity at low temperatures. a) Longitudinal resistance R_{xx} as a function of perpendicular magnetic field $B_\perp$. At $T = 60\,\mathrm{mK}$, transitions in R_{xx} appear. Starting from zero field, with increasing field amplitude a first transition occurs when the Josephson effect is suppressed, followed by a second transition at $B_\perp \sim 1\,\mathrm{T}$ when superconducting WTe_2 on Pd turns normal. The asymmetry in $R_{\mathrm{xx}}(B_\perp)$ is likely connected to heating during the magnetic field sweep since it depends on the sweep direction and gets reduced with a lower sweep rate. b) Illustration of the cross-sectional view through the device. The regions of WTe_2 above the Pd leads turn into superconducting regions (gray shaded). These regions can be connected by the Josephson effect if the space between them is not too long. c) Longitudinal resistance R_{xx} as a function of temperature. Superconducting transition takes place in the range of 1.05 K - 1.2 K. The Josephson effect gradually develops at a lower temperature reaching the zero resistance state below 350 mK.

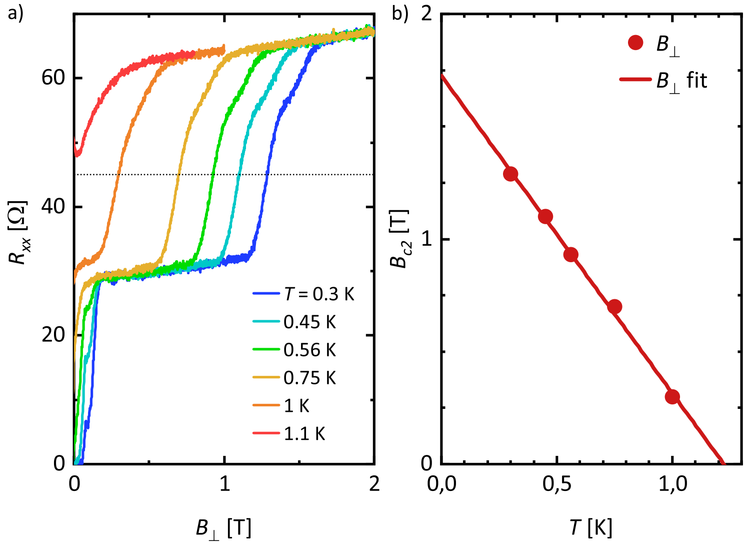

Figure 4.4. Superconductivity in perpendicular magnetic field. a) Longitudinal resistance as a function of perpendicular magnetic field $B_\perp$ at various temperatures. The dotted line indicates the resistance value used to determine $B_{c2}(T)$. The increase in the resistance near $B_\perp = 0$ is connected to heating of the sample during field sweeps. b) Critical magnetic field B_{c2} as a function of temperature. Extracted data from the measurements in a) and fit to the formula $B_{c2} \propto (1 - T/T_c)$. Panel a) reprinted with permission from Kononov *et al.*, Nano Lett. **20**, 4228 (2020). Copyright 2020 American Chemical Society.

at zero magnetic field. Fitting the experimental data with Eq. 4.1, we obtain $T_c \sim 1.2\,\mathrm{K}$ and a relatively short $\xi_{GL} \sim 14\,\mathrm{nm}$.

Disorder can cause the reduction of the coherence length, but we do not think this is the case in our samples since we have found $\ell > \xi$ and a non-saturating magnetoresistance as indication of high crystal quality. In the clean limit at low temperatures, the Ginzburg–Landau coherence length is similar to the Bardeen–Cooper–Schrieffer (BCS) coherence length $\xi_{GL} \sim \xi$. Knowing the coherence length and the critical temperature, we can estimate the Fermi velocity $v_F = \xi\pi\Delta/\hbar$, where we take for Δ the BCS relation $\Delta \sim 1.76 k_B T_c$, resulting in $v_F \sim 1.2 \times 10^4\,\mathrm{m\,s^{-1}}$.

We further investigate the superconducting properties by measuring R_{xx} as a function of in-plane magnetic field $B_\parallel$, as shown in Fig. 4.5 a). Compared

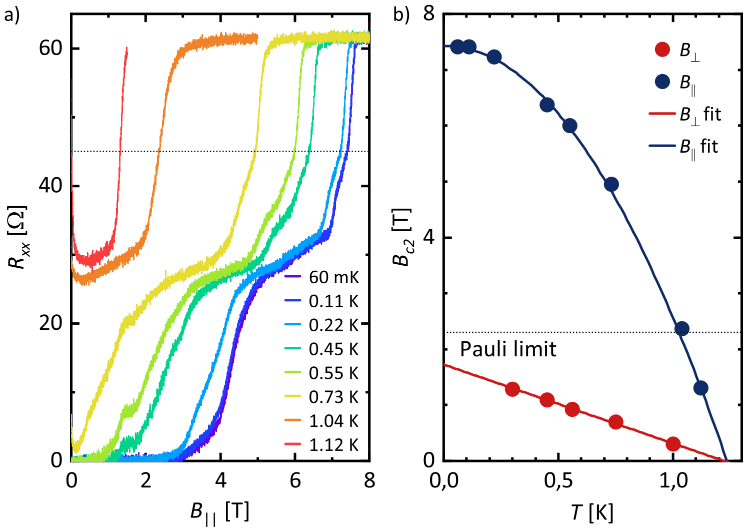

Figure 4.5. Superconductivity in parallel magnetic field. a) Longitudinal resistance R_{xx} as a function of in-plane magnetic field $B_\parallel$. B_{c2} is evaluated at the intersection of the dotted line with the data curves. The increase in resistance at $B_\parallel = 0$ is connected to heating of the sample during the field sweeps. b) Critical field $B_{c2}(T)$ as a function of temperature T. The dotted horizontal line indicates Pauli pair breaking field B_{P}, which is clearly exceeded by the given data.

with the perpendicular field, both the transitions in resistance have shifted to higher magnetic fields. Figure 4.5 b) shows the extracted critical field values as a function of temperature. $B_{c2}(T)$ is well described by the empirical formula for superconductors [22]

$$B_{\mathrm{c2}}(T) = B_{\mathrm{c2}}(0)\left[1 - \left(\frac{T}{T_{\mathrm{c}}}\right)^2\right]. \tag{4.2}$$

Both fits for the data as a function of $B_\perp$ and $B_\parallel$ converge to the same critical temperature $T_{\mathrm{c}} = 1.2\,\mathrm{K}$.

A notable feature in the data of the parallel critical field is its large value which exceeds the Pauli paramagnetic limit B_{P}. The limit is given in the BCS theory for weak coupling by $B_{\mathrm{P}} \sim 1.76 k_{\mathrm{B}} T_{\mathrm{c}} \sqrt{2}/(g\mu_{\mathrm{B}}) \sim 1.86 T_{\mathrm{c}} \sim 2.3\,\mathrm{T}$ [22, 152], with $g = 2$ being the free electron g-factor. The same effect has also been reported in case of gated mono-layer[116, 117] and bulk WTe_2 crystals

[115] as well as in thin films of other materials [153, 154]. An explanation for this effect could be given by different mechanisms, such as Ising-type superconductivity [152] or an effectively diminished g-factor due to strong spin-orbit interaction [155].

4.4. London penetration depth

Directly connected to the Meissner-Ochsenfeld effect is the London penetration depth λ_L, the length scale on which an external magnetic field can enter the superconductor before it is fully screened.

One method to measure the penetration depth is through RF-experiments [156], but it can alternatively also be estimated from the critical current oscillations in an applied perpendicular magnetic field. The oscillation period of $I_\mathrm{c}(B_\perp)$ is related to a single flux quantum Φ_0 that penetrates the effective junction area $A_\mathrm{eff} = w \times l_\mathrm{eff} = W \times (l + 2\lambda)$. Here, w and l denote the physical width and length of the junction, respectively, and λ is the magnetic field penetration depth [22], as illustrated in Fig. 4.6 a). In case of a bulk superconductor $\lambda = \lambda_\mathrm{L}$, yet for a thin superconducting film of thickness d, the penetration depth is a function of the thickness $\lambda(d) = \lambda_\mathrm{L} \coth(d/\lambda_\mathrm{L})$ [156]. In the limit of small thickness $d \ll \lambda_\mathrm{L}$, $\lambda(d)$ reduces to the Pearl's length $\lambda_\mathrm{P} = \lambda_\mathrm{L}^2/d$ [22].

Figure 4.6 b) displays the dependence $I_\mathrm{c}(B_\perp)$ for multiple Josephson junctions J_i, with i = 1,2,3. Junctions $J_{1,2}$ are $w = 4.2\,\mu\mathrm{m}$ wide and $l = 1\,\mu\mathrm{m}$ long, while for J_3 $w = 4.2\,\mu\mathrm{m}$ and $l = 0.5\,\mu\mathrm{m}$. Visible is a combination of SQUID-like oscillations that originate from the hinge states [111] and a fast decaying Fraunhofer contribution that can be attributed to Fermi-arc surface states [102, 103, 157, 158] or conducting bulk states. The extent of SQUID-oscillations in magnetic field allows to determine their period with good precision. We find for junctions J_1 and J_2 a period $\delta B = 0.27\,\mathrm{mT}$, corresponding to an effective junction length $l_\mathrm{eff} = 1.77\,\mu\mathrm{m}$ and a penetration depth $\lambda = 380\,\mathrm{nm}$. For junction J_3, the oscillation period is found to be $\delta B = 0.41\,\mathrm{mT}$, resulting in $\lambda = 350\,\mathrm{nm}$. Since the penetration depth is much larger than the flake thickness $d \sim 7\,\mathrm{nm}$, equivalent to approximately 10 crystal layers, the penetration depth is given by the Pearl's length $\lambda = \lambda_\mathrm{P} = \lambda_\mathrm{L}^2/d$. With this expression we can estimate the London penetration depth $\lambda_\mathrm{L} \sim 50\,\mathrm{nm}$. The ratio of London penetration depth and coherence length $\kappa = \lambda_\mathrm{L}/\xi$ is $\kappa \sim 3 > 1/\sqrt{2}$ and therefore suggest type-II superconductivity [22].

The obtained London penetration depth is in accordance with typical values for metals and therefore surprisingly small considering the semi-metallic nature of WTe_2. This provides further evidence against the presence of disorder in our samples, since the penetration depth is expected to increase for dirty compared to clean superconductors [22]. An estimate of the superconducting electron

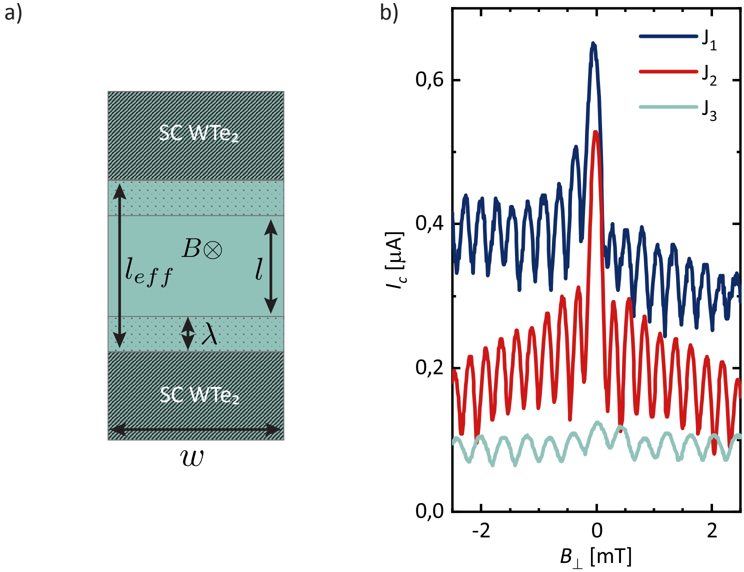

Figure 4.6. Flux focussing and penetration depth. a) Illustration of flux focussing in the JJ. The magnetic field threads the effective junction area $A_{\text{eff}} = L_{\text{eff}} \times W = (L + 2\lambda) \times W$ with the penetration depth λ of the magnetic field into the superconductor. b) Critical current as a function of perpendicular magnetic field for three different junctions J_1, J_2, J_3. Data in b) are used with permission from Kononov *et al.*, Nano Lett. **20**, 4228 (2020). Copyright 2020 American Chemical Society.

density yields a relatively high value of $n_{\text{s}} = m/(\mu_0 \lambda_{\text{L}}^2 e^2) \sim 3 \times 10^{21}\,\text{cm}^{-3}$, with $m \sim 0.3 m_{\text{e}}$ being the effective electron mass in WTe_2 [159]. The value for n_{s} exceeds the carrier density typically reported $n \sim 10 \times 10^{19}\,\text{cm}^{-3}$ [160] for WTe_2. n_{s} can be connected to the single layer density $n_{\text{s}}^{\text{1L}} \sim 2 \times 10^{14}\,\text{cm}^{-1}$, exceeding the reported electron density of WTe_2 that is gated into superconductivity [116, 117] by an order of magnitude. Though, n_{s}^{1D} is close to the theoretically predicted value for maximum superconducting pairing stability [161]. Associated with the high carrier density, we find a high density of states at the Fermi level $g(E_{\text{F}}) = n_{\text{s}}/(2\Delta) \sim 8 \times 10^{24}\,\text{cm}^{-3}\,\text{eV}^{-1}$.

4.5. Conclusion

In this chapter we have presented superconductivity emerging in WTe_2 when the crystal is brought in contact with palladium bottom contacts. By means of transport measurements, we were able to deduce the fundamental properties such as the critical temperature T_c, the coherence length ξ and the London penetration depth λ_L of the novel superconducting state. Interestingly, we found that the in-plane critical field exceeds the Pauli limit.

In the following chapters we will continue to investigate the properties of this superconducting state and the properties of Josephson junctions formed out of it.

4.6. Comment on the data analysis in the superconducting clean limit

4

At the time of publication of the above paper, the origin of superconductivity in WTe_2 on Pd was not known, yet. The analysis was conducted under the assumption that WTe_2 itself becomes superconducting and that it can be treated in the superconducting clean limit. This conclusion was drawn from the evaluation of the Shubnikov-de-Haas oscillations of the WTe_2 flake in magnetic field. The determined mean-free path ℓ of WTe_2 was compared to the superconducting coherence length and we found $\ell > \xi$. However, we discovered only recently that superconductivity originates not from WTe_2 but from the novel compound $PdTe_x$, which forms through the diffusion of Pd from the bottom contact into the WTe_2 crystal. The process is investigated in detail in Ch. 6.

It is therefore necessary to take into account the material properties of the newly formed crystal and anticipate the possibility that $\ell_{\mathrm{PdTe_x}} \ll \xi$. The analysis in this so called superconducting dirty limit is governed by the mean-free path $\ell_{\mathrm{PdTe_x}}$ [22], a quantity that is not known at the moment. It remains therefore subject to future experiments to determine the framework in which the superconductor $PdTe_x$ can be treated.

5 Tunnelling spectroscopy on superconducting WTe_2

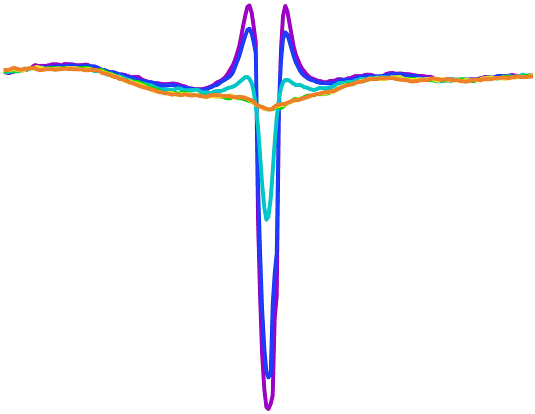

In this chapter we introduce the concept of tunnelling spectroscopy to locally investigate the superconducting density of states in WTe_2 on Pd. We have fabricated samples with a thin hBN flake acting as a tunnel barrier between superconducting WTe_2 on Pd and a metallic tunnel contact. We investigate the tunnelling conductance in a magnetic field and as a function of WTe_2 flake thickness. The observed data complements the results from the transport measurements and further highlights the role of the underlying Pd bottom contact together with the diffusion of Pd in WTe_2.

5.1. Introduction

En route to discover novel superconducting materials it is helpful to understand the mechanisms behind the breakdown of the pairing state. Disorder, low electron density and interactions often compete against each other in destroying superconductivity in low dimensional superconductors [162], turning them into an active research field to study these mechanisms. Superconducting TMDCs provide in this regard an ideal platform, because the evolution of their superconducting properties can be studied all the way from the bulk to the mono-layer limit [163, 164]. Compared to strongly disordered superconducting thin films [165], TMDCs preserve their high quality even in the few layer limit and can additionally be well isolated from substrate interactions.

In the following chapter we use tunnel spectroscopy as a measurement technique to extend our understanding of the superconducting state in WTe_2 gained from transport measurements in the previous chapter. Compared to transport measurements, tunnel spectroscopy allows probing directly the local density of states in the material.

5

5.2. Theory of tunnel spectroscopy on a superconductor

In the following section we introduce the fundamental concept of tunnelling spectroscopy and show that at low temperatures it allows to directly map the density of states $\mathcal{D}_{\mathrm{S}}(E)$ (compare Eq. 2.1) [166, 167] of the superconductor.

Tunnel spectroscopy relies on the quantum mechanical tunnelling of electrons through an insulating barrier [168]. The transmission probability $t \propto \exp(-2d\sqrt{2mU}/\hbar)$ [169] for an electron of mass m to tunnel through the potential barrier depends exponentially on the barrier's height U and width d. Together with details about the insulating material, the transmission probability is phenomenologically described by the transmission matrix element M [22].

We consider a junction of two normal metals (N) with densities $\mathcal{D}_{\mathrm{N},1}$ and $\mathcal{D}_{\mathrm{N},2}$ that are separated by an insulating tunnel barrier (I). A voltage V is applied across the junction, such that an energy difference eV is created between the chemical potentials of the two metals relative to each other. The net current I

$$I(V) = A|M|^2 \int_{-\infty}^{\infty} \mathcal{D}_{\mathrm{N},1}(E)\mathcal{D}_{\mathrm{N},2}(E+eV)[f(E) - f(E+eV)]dE \quad (5.1)$$

is composed of the difference in tunnel currents $I_{1\to 2}$ and $I_{2\to 1}$ flowing from metal 1 to 2 and vice versa [22, 166, 169]. In Eq. 5.1, f denotes the Fermi distribution function, A is a proportionality constant and M is the energy independent tunnel matrix element. In the following, we apply the previous equation to two possible configurations, the N-I-N and a N-I-S (superconductor) junctions.

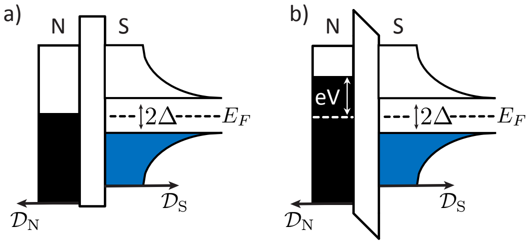

Figure 5.1. Quasiparticle tunnelling at a normal metal (N) superconductor (S) interface. Density of states for a normal metal $\mathcal{D}_\mathrm{N}(E)$ and a superconductor $\mathcal{D}_\mathrm{S}(E)$ at zero temperature. The occupied states for the metal and superconductor are drawn in black and blue, respectively. a) In equilibrium, no quasiparticles can tunnel from the normal metal contact into the superconductor due to lack of available states. b) An onset of a tunnel current is observed when an applied voltage U between the NS interface reaches $eV \geq \Delta$. Figure adapted from Ref. [170].

Beginning with the N-I-N junction, it is possible to approximate the density of states in the normal metallic contact as constant and equal to the value at the Fermi energy $\mathcal{D}_\mathrm{N}(E + E_F) = \mathcal{D}_\mathrm{N}(E_F)$, provided that the temperature $k_\mathrm{B}T \ll E_\mathrm{F}$ is low and the applied voltage $V \ll E_\mathrm{F}/e$ is small [169]. The tunnelling current can then be written as [22]

$$\begin{aligned} I_\mathrm{NN}(V) &= A|M|^2 \mathcal{D}_{\mathrm{N},1}(E_\mathrm{F})\mathcal{D}_{\mathrm{N},2}(E_\mathrm{F}) \int_{-\infty}^{\infty} [f(E) - f(E+eV)]dE \\ &= A|M|^2 \mathcal{D}_{\mathrm{N},1}\mathcal{D}_{\mathrm{N},2} eV \\ &= G_\mathrm{NN} V. \end{aligned} \tag{5.2}$$

The junction is in its ohmic state with its characteristic conductance G_NN, such that the current depends linearly on the applied voltage across the tunnel barrier.

In the second case, one of the tunnel contacts is considered to be a superconductor, with its density of states described by Eq. 2.1, as illustrated in Fig. 5.1. The resulting current $I_\mathrm{NS}(V)$ can be written as [22]

$$\begin{aligned} I_\mathrm{NS}(V) &= A|M|^2 \mathcal{D}_\mathrm{N}(E_F) \int_{-\infty}^{\infty} \mathcal{D}_\mathrm{S}(E)[f(E) - f(E+eV)]dE \\ &= \frac{G_\mathrm{NN}}{e} \int_{-\infty}^{\infty} \frac{\mathcal{D}_\mathrm{S}(E)}{\mathcal{D}_\mathrm{S,N}(E_\mathrm{F})} [f(E) - f(E+eV)]dE. \end{aligned} \tag{5.3}$$

Here, $\mathcal{D}_{\mathrm{S,N}}(E_{\mathrm{F}})$ denotes the normal state density of states of the superconducting contact. Recalling the energy dependence of $\mathcal{D}_{\mathrm{S}}(E)$, Eq. 5.3 yields zero at zero temperature for $e|V|< \Delta$, as illustrated in Fig. 5.1 a). Depicted in Fig. 5.1 b) for $e|V|\geq \Delta$, charge carriers can tunnel from the normal metal into the superconductor, resulting in a symmetric onset in tunnel current around zero bias at $|V|= \Delta$.

For $T \to 0$, the differential conductance [22]

$$\begin{aligned} G_{\mathrm{NS}} &= \frac{dI_{\mathrm{NS}}}{dV} \\ &= G_{\mathrm{NN}} \int_{-\infty}^{\infty} \frac{\mathcal{D}_{\mathrm{S}}(E)}{\mathcal{D}_{\mathrm{S,N}}(E_{\mathrm{F}})} \left[\frac{\partial f(E+eV)}{\partial (eV)} \right] dE \overset{T\to 0}{=} G_{\mathrm{NN}} \frac{\mathcal{D}_{\mathrm{S}}(E_{\mathrm{F}}+e|V|)}{\mathcal{D}_{\mathrm{S,N}}(E_{\mathrm{F}})} \end{aligned} \tag{5.4}$$

directly relates the experimentally obtained dI/dV curve to the density of states in the investigated superconductor. For finite temperatures $T \neq 0$, $\mathcal{D}_{\mathrm{S}}(\Delta)$ deviates from a step like function as it begins to soften up, causing G_{NS} to measure a superconducting density of states that is blurred over a range $\pm 2k_{\mathrm{B}}T$ [22].

5

5.3. Sample fabrication

Fabrication of the tunnel devices begins with the exfoliation and stacking of single vdW layers as described in Ch. 3. We have chosen a WTe_2 with multiple step edges, shown in Fig. 5.2, to study thickness dependent effects. Figure 5.2 b) shows the selected hBN flake with thickness of either mono- or bi-layer to act as a tunnel barrier.

In order to create a uniform superconducting state in WTe_2, the flake is placed entirely on a large Pd bottom contact, with WTe_2 covered by a thin hBN that serves as both, a tunnel barrier and a protection against oxidation of the flake. The tunnel contacts are made out of titanium (Ti) and gold (Au) and are insulated from Pd through 50 nm thick, evaporated SiO_2 that is patterned via standard e-beam lithography, such that the later tunnel contact area on hBN is spared. Afterwards, tunnel contacts to the vdW stack and Pd are deposited by e-beam evaporation. An image of the finished device is shown in Fig. 5.2 c) together with a cross-sectional schematic of the layers in d).

A big challenge of these devices is the low yield $\sim 10\%$ of tunnel junctions that are not shortened to ground. The problem is ascribed to the fact that the metal leads have to overcome several step edges of the Pd bottom contact and the SiO_2 layer. Additionally, the e-beam evaporated SiO_2 layer might be inhomogeneous such that shorts are created.

For the measurement of such device, a dc voltage V, superimposed with a small ac voltage V_{AC}, is applied between the metallic tunnel contact and

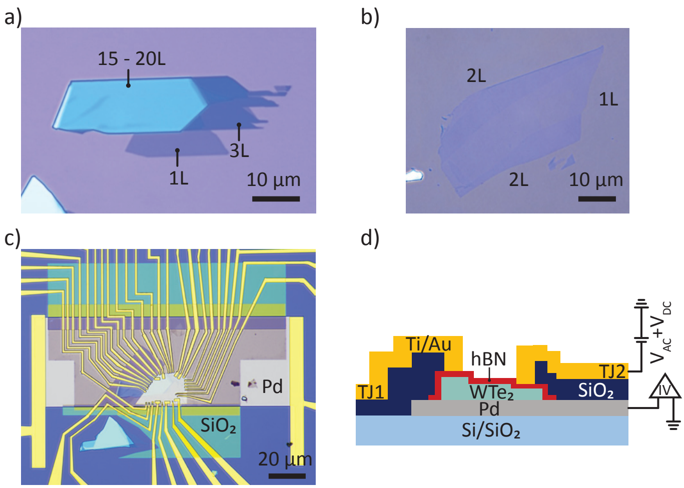

Figure 5.2. Layout of the tunnelling device. a) Optical image of the used WTe_2 flake with multiple thickness steps. b) Optical image of the hBN flake used as tunnel barrier. It consists of a mono-layer part in its center, framed by bi-layer stripes on the top and bottom. c) Optical image of the finished device. Visible is the rectangular Pd bottom contact that is connected to electrical ground through two vertical Ti/Au electrodes on the left and right, respectively. In order to insulate the tunneling contacts from the Pd bottom contact, a thin layer of SiO_2 has been selectively evaporated on top of the sample. d) Cross sectional schematic of the device including the measurement configuration. Multiple tunnel contacts are brought from the outside to the hBN/WTe_2 at their end where they are in direct contact with the hBN tunnel barrier. Two exemplary junctions are indicated by the labels TJ1 and TJ2, respectively.

the grounded Pd bottom contact as shown in the schematics Fig. 5.2 d). We measure the differential conductance of the tunnel current as a function of applied voltage V across the tunnel junction.

5.4. Spectroscopy on a thick WTe_2 crystal

We begin with the data obtained from a tunnel junction TJ3 with a junction area $A_\square = 4\,\mu\text{m}^2$, which is placed on the 15-20 layer-thick part of the WTe_2 crystal in Fig. 5.2 a). Figure 5.3 a) plots the dependence of the tunnel current I on the applied voltage V across the junction. The $I(V)$ data follows

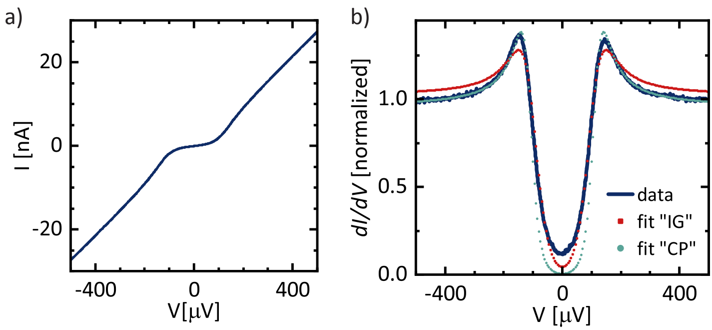

Figure 5.3. Tunnel spectroscopy on a thick WT$_2$ crystal. a) Characteristic $I(V)$ curve of a tunnel junction demonstrating a current suppression when $e|V| < \Delta$. b) dI/dV data of the same junction in a), effectively probing $\mathcal{D}_\mathrm{S}$ of superconducting WTe$_2$ on Pd. The data is normalized to the value at $V = 500\,\mathrm{mV}$. Two fit curves to the data based on Eq. 5.4 are plotted, focussing either on the low spectrum inside the gap ("IG") or the high conductance values of the coherence peaks and outside the gap ("CP").

5

the previously introduced characteristics of a tunnel junction, with a distinct suppression of the tunnel current when $e|V| < \Delta$.

The differential conductance dI/dV across the tunnel interface of TJ3 is presented in Fig. 5.3 b). The data is normalized to its normal conductance value $G_\mathrm{N} = 1.5G_0$ outside the gap at $V = 500\,\mu\mathrm{V}$. $G_0 = e^2/h$ denotes the conductance quantum. A well defined gap with a suppression factor $G_\mathrm{N}/G_{\mathrm{V}=0} \sim 8$ is visible, with $G_{\mathrm{V}=0}$ being the conductance at $V = 0$. Distinct conductance peaks reside at each side of the gap. We fit the differential tunnel conductance by Eq. 5.4, with the superconducting density of states

$$\mathcal{D}_\mathrm{S}(E, \Gamma, \Delta) = \mathrm{Re}\left[\frac{E - i\Gamma}{\sqrt{(E - i\Gamma)^2 - \Delta^2}}\right], \tag{5.5}$$

expressed by the Dynes formula [163, 171]. Here, Γ accounts for the lifetime broadening of quasi-particles in the superconductor, resulting in a smearing out of the gap. It is not possible to fit the data in the whole voltage range using Eqs. 5.4 with 5.5 due to the remaining conductance at zero bias. We therefore focus on two regimes, labelled "IG" for inside the gap and "CP" for the coherence peaks, respectively, that aim to fit best the data inside the gap and at high conductance values of the coherence peaks and beyond. The residual conductance $G_{\mathrm{V}=0}$ can potentially originate from tunnelling of the electrons from the metallic contact into the Pd bottom contact, as we later

	fit “IG”	fit “CP”
Γ[µeV]	17	17
Δ[µeV]	103	115
T[mK]	198	93

Table 5.1. Fit parameters to the tunnel conductance in Fig. 5.3 b). Γ denotes the quasi-particle lifetime broadening, Δ the superconducting gap and T the system temperature.

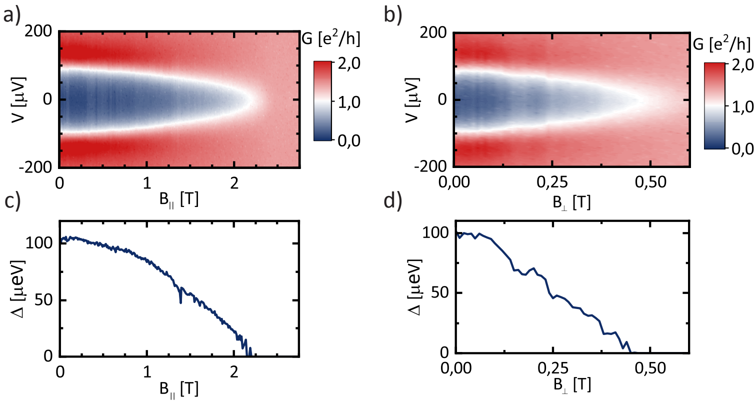

Figure 5.4. Magnetic field dependence of the tunnel conductance. Shown is the conductance across the N-I-S interface as a function of applied bias voltage and magnetic field in a) in-plane $\parallel$ and b) out-of-plane $\perp$ direction to the junction plane. c) and d) plot $\Delta(B)$, extracted from the fit to the data for the above data.

observe an increasing parasitic conductance at $V = 0$ with decreasing WTe_2 thickness. Additionally it is possible, that a thin crystal of WTe_2 remains on top of the $PdTe_x$ diffusion layer, as we show in Ch. 6, such that we observe a proximitized rather than the real superconducting gap. The two fits are obtained with the parameters summarized in table 5.1. Both fits yield comparable values, although the fit to the high conductance values is considered more reliable due to the remaining in-gap conductance.

Magnetic field dependence

We next focus on the magnetic field dependence of the spectra. Figures 5.4 a) and b) present the tunnel conductance across the N-I-S interface as a function

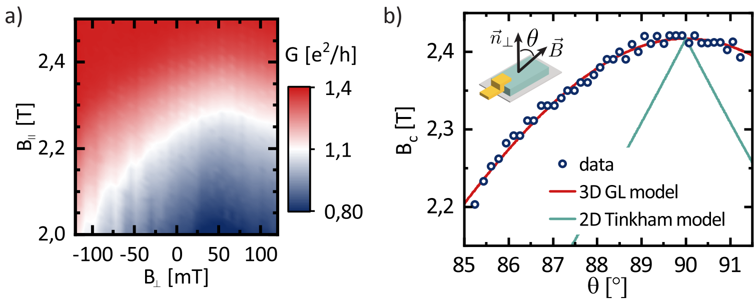

Figure 5.5. Angular dependence of the critical field B_c. a) Conductance measurement as a function of parallel $\|$ and perpendicular $\perp$ magnetic field. b) Extracted critical field value B_c as function of angle relative to the junction normal, as illustrated by the insert. $B_c(\theta)$ is well described by the anisotropic Ginzburg-Landau model in three dimensions in contrast to the Tinkham model for a 2D superconductor.

of bias voltage and magnetic field in the direction parallel $\|$ and perpendicular $\perp$ to the junction plane, respectively. Analogue to the fitting of the conductance data before, we use Eqs. 5.4 with 5.5 to extract Δ from the bias sweeps at different magnetic fields and plot the dependence $\Delta(B)$ in Figs. 5.4 c) for the parallel and d) for the perpendicular field direction, respectively. The obtained critical field values, at which Δ vanishes, are $B_{\|,c} \sim 2.15\,\mathrm{T}$ and $B_{\perp,c} \sim 0.45\,\mathrm{T}$.

Angular dependence of the critical field

We study the angular dependence of the critical field B_c. Due to the limitations of the available magnetic fields in the cryostat, the sample is mounted such, that we investigate the transition close to in-plane fields parallel to the junction, as illustrated by the inset in Fig. 5.5 b). Figure 5.5 a) plots the measured tunnel conductance as a function of $B_\perp$ and $B_\|$ at $V = 0$. The extracted $B_c = \mu_0 H_c$ is shown in Fig. 5.5 b) as a function of angle $\theta = \arctan(B_{c,\perp}/B_{c,\|})180/\pi + 90°$, measured relative to the junction normal, as illustrated by the inset. The critical field B_c is defined as the field value at which the conductance reaches 0.95 G_N, evaluated at the vector sum of the fields $B_{c,\perp}$ and $B_{c,\|}$. Contrary to the low dimensionality of the system, the data does not follow the dependence of a two-dimensional superconductor, described by the Tinkham model [22]

$$\left|\frac{H_c(\theta)\cos(\theta)}{H_{\perp,c}}\right| + \left(\frac{H_c(\theta)\sin(\theta)}{H_{\|,c}}\right)^2 = 1, \tag{5.6}$$

and plotted in green in Fig. 5.5 b). Instead, the data is well described by the anisotropic Ginzburg-Landau model [22]

$$\left(\frac{H_{\mathrm{c}}(\theta)\sin(\theta)}{H_{\perp,\mathrm{c}}}\right)^2 + \left(\frac{H_{\mathrm{c}}(\theta)\cos(\theta)}{H_{\parallel,\mathrm{c}}}\right)^2 = 1 \tag{5.7}$$

for three-dimensional superconductors, plotted as red curve in Fig. 5.5 b). The anisotropic Ginzburg-Landau model was developed in the framework of layered superconductors and has found its application in TMDCs [172, 173]. At its core, it assumes an arrangement of stacked two-dimensional superconducting layers that are tunnel coupled to each other [22]. The model yields $B_{\perp,\mathrm{c}} = 0.46\,\mathrm{T}$ and $B_{\parallel,\mathrm{c}} = 2.42\,\mathrm{T}$, in agreement with the previously extracted values.

From the above angle dependence we see that the sample clearly follows the expected dependence for a layered bulk superconductor, rather than the theory for a two-dimensional superconductor. Latter is valid for materials with thickness $d \ll \xi$. This observation can be explained by the diffusion of Pd into WTe_2 and the formation of a possibly dirty superconducting $PdTe_x$ with a small ξ. The argument is in line with sections 4.6 and 5.6.

5

5.5. Thickness dependence

We continue with making use of the various step edges in the WTe_2 flake and address the thickness dependence of the tunnel conductance for various junctions. Figure 5.6 combines the data obtained from four different tunnel junctions, ranging in WTe_2 thickness from 15-20 layers down to mono-layer. Temperature dependent measurements up to 4 K highlight the superconducting contribution to the curves.

With decreasing WTe_2 thickness, the overall conductance across the N-I-S interface increases. Additionally, the thin junctions plotted in Fig. 5.6 c) and d) develop a non-linear background that remains almost independent of the temperature.

We use the high temperature data at 4 K to subtract the non-linear background from the data obtained at 30 mK, as plotted in Fig. 5.7 a) and b) for the thick and thin WTe_2 crystals, respectively. Due to the low suppression factor, a fit to the data obtained from the thin flakes becomes unreliable and we proceed to discuss the development in Δ quantitatively, based on the evaluation of the coherence peak positions. Table 5.2 summarizes the junction parameters.

In general, the conductance outside of the gap G_{N} increases with decreasing WTe_2 thickness, while the ratio of $G_{\mathrm{N}}/G_{\mathrm{V=0}}$ inside the gap decreases. Comparing tunnel junctions of the same hBN thickness, the normal conductance per area $G_{\mathrm{N}}/A_{\square}$ increases from $\sim 0.3\ G_0/\mu\mathrm{m}^2$ for TJ3 with thick WTe_2 to $\sim 24\ G_0/\mu\mathrm{m}^2$ for TJ9 with a mono-layer. We attribute this effect to the sample

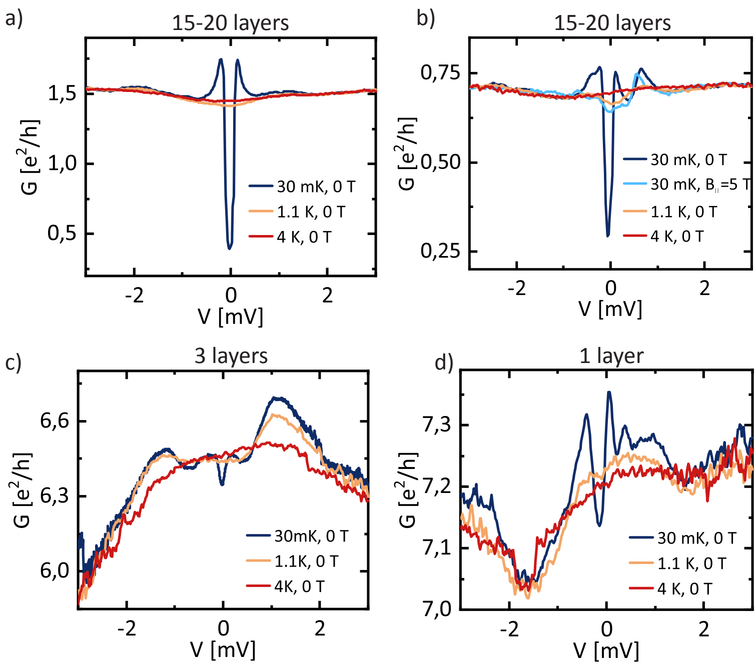

Figure 5.6. Thickness dependent tunnel spectroscopy. Tunnel spectra for four different junctions, ranging in WTe_2 thickness from a) and b) 15-20 layers, c) three layers to d) mono-layer. The feature at positive bias voltages in b) does not originate from superconductivity as indicated by the absence of magnetic field dependence. The thin WTe_2 junctions develop a non-linear conductance background that is temperature independent in measurements up to $T = 4\,\mathrm{K}$.

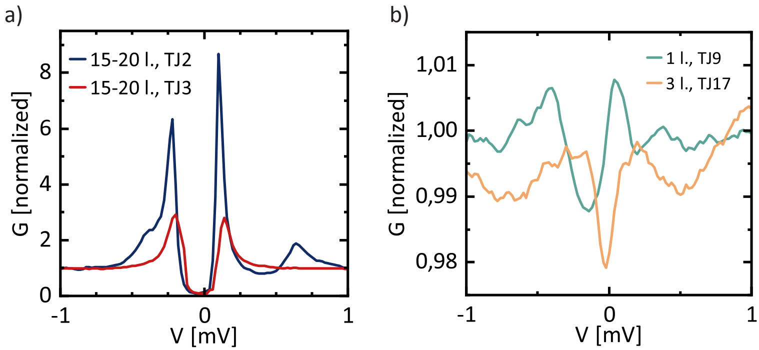

Figure 5.7. Dependence of Δ on WTe_2 thickness. Normalized tunnel spectra for four different junctions with subtracted conductance at 4 K for a) thick and b) thin WTe_2 crystals. The corresponding crystal thickness is indicated in the plot legends.

design with a metallic bottom contact below the whole stack. With decreasing WTe_2 thickness, electrons tunnel increasingly directly into the underlying metallic Pd contact. Additionally, Δ tends to increase with decreasing WTe_2 thickness, but the limited data does not allow to draw a definite conclusion at this moment.

TJ	$d_{\mathrm{WTe_2}}$ [layers]	d_{hBN} [layers]	$A_\square$ [µm^2]	G_N [G_0]	$G_\mathrm{N}/A_\square$ [G_0/µm^2]	Δ [µeV]
2	15-20	2	4	0.73	0.18	161
3	15-20	2	5	1.5	0.3	172
17	3	1	1	6.45	6.45	186
9	1	2	0.3	7.25	24.2	231

Table 5.2. Summary of tunnel junction parameters. The thickness of the vdW materials is given by d, $A_\square$ is the area of the tunnel junction, G_N is the normal state conductance at high bias voltage and Δ is the superconducting gap extracted from the position of the coherence peaks.

5.6. Comparison between tunnelling spectroscopy and transport measurements

The extracted parameters of the superconducting state gained by the tunnelling spectroscopy on thick WTe_2 allow a comparison with the previously

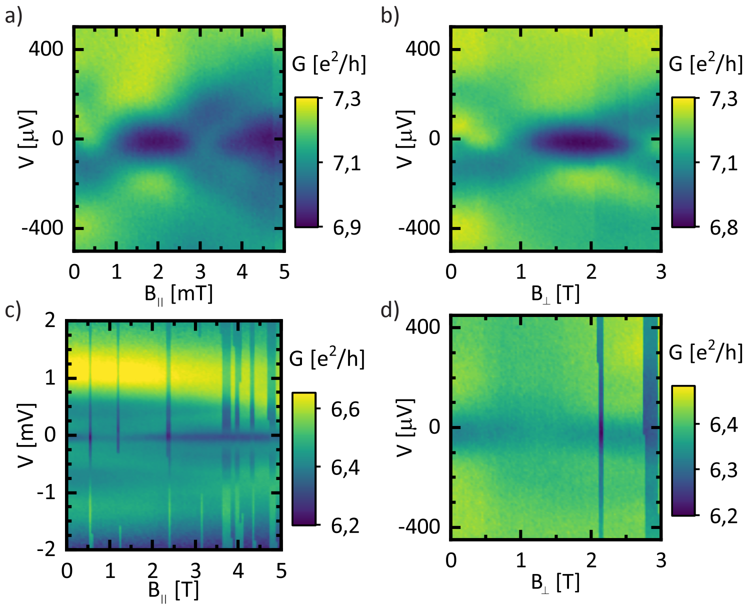

Figure 5.8. Unconventional behavior of thin WTe_2 tunnel junctions in magnetic field. Tunnel conductance as a function of magnetic field and bias voltage for thin WTe_2 with a single layer in a) and b) and three layers in c) and d).

found values from the transport measurements in Ch. 4.

In general, we obtain smaller gap and critical magnetic field values in case of the tunnel junction (TJ), compared to the transport measurement (JJ). Comparing the values, we find $\Delta_{\mathrm{TJ}} = 115\,\mu\mathrm{eV}$ versus $\Delta_{\mathrm{JJ}} = 170\,\mu\mathrm{eV}$ as well as the critical field values $B_{\mathrm{c},\perp,\mathrm{TJ}} = 0.49\,\mathrm{T}$ and $B_{\mathrm{c},\|,\mathrm{TJ}} = 2.45\,\mathrm{T}$ versus $B_{\mathrm{c},\perp,\mathrm{JJ}} = 1.27\,\mathrm{T}$ and $B_{\mathrm{c},\|,\mathrm{JJ}} = 7.41\,\mathrm{T}$, respectively.

The discrepancy can be most likely explained in the framework of Pd diffusion into WTe_2 and the formation of superconducting $PdTe_x$ as presented in detail in Ch. 6. $PdTe_x$ does not form homogeneously throughout a thick WTe_2 crystal, but is limited in its extension perpendicular to the vdW layers. Therefore, an unchanged WTe_2 layer likely remains in between superconducting $PdTe_x$ and the hBN tunnel barrier. Rather than measuring the real superconducting gap of $PdTe_x$, we measure a reduced, proximitized gap of the remaining WTe_2 layer in the tunnel experiment.

5.7. Magnetic field dependence of thin WTe_2

We would like to conclude the chapter with magnetic field measurements on the two thinnest WTe_2 junctions TJ17 and TJ9. Figure 5.8 shows the conductance as a function of magnetic field and bias voltage in in-plane $\|$ and out-of-plane $\perp$ field direction. Plots in Figs. 5.8 a) and b) are obtained from the mono-layer crystal and Figs. 5.8 c) and d) from three layer thick WTe_2. In contrast to the behavior of the thick crystal (compare Fig. 5.4), the data reveals a non-monotonous opening and closing of a gap. The behavior is particularly pronounced in Fig. 5.8 a) where a gap opens around zero bias between $1\,\mathrm{T} < B_{\|} < 3\,\mathrm{T}$.

Such re-entrance of superconductivity is often connected in literature with an exotic superconducting pairing in the material [174]. If the observed gap in the spectra of Figs. 5.8 is indeed of superconducting origin, it could point towards non-singlet order parameter in the system. At this moment, however, the presented data does not allow a conclusive interpretation of this phenomenon, yet, and requires further investigation.

5.8. Conclusion

In this chapter we have successfully fabricated fully integrated vdW tunnel junctions with a hBN tunnel barrier. The observed superconducting gap underlines the emerging superconductivity in WTe_2 on Pd and complements the previous transport measurements. The obtained values for Δ and the critical fields are systematically smaller compared to the values obtained from transport measurements, indicating a proximitized WTe_2 layer on top of $PdTe_x$.We find further an increased tunnelling rate into the underlying Pd bottom contact with decreasing WTe_2 thickness.

Additionally, samples with very thin WTe_2 have revealed novel features in an applied magnetic field that have not been understood so far and require further investigation.

We would like to note that we have also fabricated samples using few-layer MoS_2 as a tunnel barrier. As it turns out, the material becomes conducting in this vdW configuration, potentially through doping by the Pd bottom contact.

6 Origin of superconductivity in WTe_2/Pd heterostructures[1]

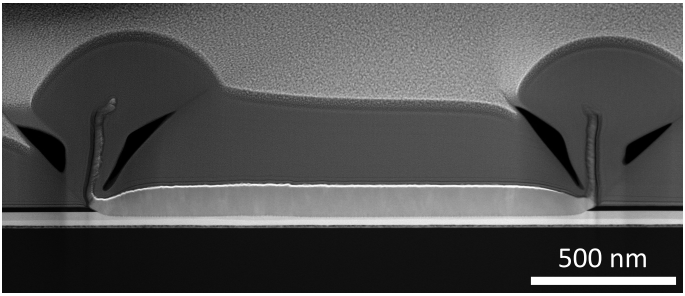

In the previous chapters we have shown that WTe_2 turns superconducting, when the crystal is placed on Pd bottom contacts, establishing the material system as a promising candidate for topological superconductivity. Until now, the macroscopic properties of this phenomenon have been studied but its microscopic origin had not been addressed.

In this chapter we will present the diffusion of Pd into WTe_2 and the formation of superconducting $PdTe_x$ as the origin of superconductivity. We find an atomically sharp interface between the diffusion layer and its host crystal in the direction vertical to the vdW layers. The diffusion is discovered to be non uniform along the width of the WTe_2 crystal, with a greater extent along the edges compared to the bulk.

In the second part, we continue to use the diffusion contact to WTe_2 and develop a contacting method that allows to integrate the vdW structure into an external superconducting circuit. The potential of this contacting method is highlighted in transport measurements on Josephson junctions, that reveal increased device quality in terms of heating effects.

[1] This chapter has been published in a similar form in Ref. M.Endres *et al.* [175]

6.1. Introduction

In the previous chapters we have studied the macroscopic properties of the emerging superconductivity when WTe_2 is brought in contact with Pd. This phenomena has established WTe_2 as an exciting platform on the path to pursue topological superconductivity by proximitizing the topological hinge states of the material with a superconductor [8, 12]. The research field of artificially designed topological superconductors has been met with great interest in recent years, as these material could host Majorana bound states, the elementary building block of fault-tolerant qubits [90].

Fundamental to the approach of engineered topological superconductivity is a highly transparent interface between the superconductor and the topological insulator [176] through which the boundary states are proximitzed. Even with state-of-the-art nano-fabrication it remains challenging to create such pristine material interfaces as oxidation [131–133, 177], contamination and rough crystal interfaces introduce defects and therefore decrease contact transparency [31, 37].

The previous transport and tunnelling experiments in Chs. 4 and 5 have left room for speculation about the origin of superconductivity in WTe_2 in contact with Pd. In the literature, similar effects of observed superconductivity upon contact between non-superconducting materials have been reported amongst others for the Dirac material Cd_3As_2 [178–180] and various Weyl semimetals [181–183]. WTe_2 itself has been reported to enter the superconducting state, as reviewed in Ch. 2.2.5. For the given material combination with Pd, potential explanations could be a structural change at the interface between the materials resulting in a situation similar to the case of pressure induced superconductivity in WTe_2 [113, 114]. Alternatively, electron doping through the Pd contact could be possible, being in accordance with the observation that the in-plane critical field exceeds the Pauli-limit (compare Ch. 4.3), as reported in Refs. [115–117]. Recently, a third option has come forward, as the diffusion of Pd into the tellurium based topological material $(Bi_{1-x}Sb_x)_2Te_3$ [184, 185] has been reported to turn the material superconducting. The discovery led to the systematic investigation of WTe_2/Pd samples by high-resolution imaging techniques on a microscopic level.

In the following chapter, we report the diffusion of Pd into WTe_2, forming superconducting $PdTe_x$, as the origin of superconductivity in the WTe_2/Pd system. The interface between $PdTe_x$ and WTe_2 is found to be atomically sharp in the direction vertical to the vdW layers, eliminating crystal-roughness between the superconductor and the higher-order TI completely. We further investigate the formation of $PdTe_x$ along the width of the WTe_2 host crystal and find it to be non uniform, with greater extent along the edges compared to the bulk.

The potential of this novel contacting method to WTe_2 is highlighted in transport measurements on JJs that show improved quality when contacted externally by an intrinsic superconductor.

6.2. Pd diffusion into WTe_2

The fabrication of the studied samples follows the procedure described in chapter 3 and appendix A. We present in the following chapter two different contacting methods, depending on the intended experiment. One is the previously used normal contact to the Pd bottom contacts, which extend away from the vdW stack. The other method is through superconducting leads that are deposited on top of the sample after etching through the covering hBN. It should be noted that superconductivity is induced into WTe_2 by the Pd contacts alone [111, 143] and that additional superconducting contacts are not required to form Josephson junctions. Figure 6.1 a) demonstrates an optical image of one of the devices. This device was prepared specially for the STEM/EDX measurements, therefore additional top superconducting contacts do not have any practical purpose and are placed to replicate real transport devices.

In order to investigate the origin of superconductivity in WTe_2 in contact with Pd, we conduct high resolution scanning transmission electron microscopy (STEM) imaging of the interface region. Crucial for this technique is the fabrication of a thin lamella of the sample that has to be carefully extracted from the finished device and mounted on a holder for the STEM. Figure 6.1 b) shows a scanning electron microscopy (SEM) image of the device presented in Fig. 6.1 a). Visible are horizontal lines of deposited platinum (Pt) covering the sample and protecting it from potential damage in the cutting process. The lamella is extracted by a gallium ion beam of a field ion beam (FIB) microscope, as illustrated in Fig. 6.1 c) and d). Once finished, the lamella is lifted-off from the original sample and mounted on a STEM holder in e). Discernible is the Si/SiO_2 substrate at the bottom, followed by a brighter layer that consists of the vdW stack in the middle, topped by the darker Pt protection layer. Detailed fabrication parameters can be found in appendix B.

The illustration in Fig. 6.2 a) indicates the direction of the extracted lamella by a dashed line and the viewing direction by a perpendicular arrow. Figure 6.2 b) presents the STEM image taken with a high-annular angular dark field detector (HAADF) at the edge of a Pd bottom contact, reaching into the weak link of the junction. Visible at first glance is a bright layer that has formed at the interface between the Pd bottom contact and the WTe_2 crystal on top. Moreover, the original Pd contact in the bottom right corner of Fig. 6.2 b) appears hollow and faded out, suggesting that the bright layer in WTe_2 is a result of Pd diffusion from the contact.

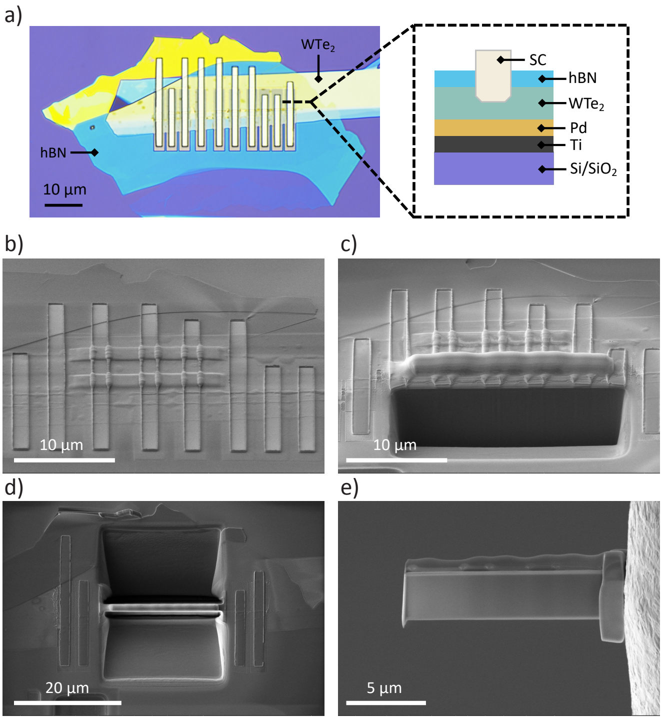

Figure 6.1. Preparation of the STEM lamella. a) Left: Optical image of the elongated WTe_2 flake covered with hBN on top of Pd contacts. Additional superconducting contacts (niobium) to WTe_2 are deposited on top. Right: A schematic crosssection of the device in a region of single Pd contact. b) SEM image of the same device. Visible are horizontal platinum (Pt) stripes that have been deposited on top of the device, at the place where the lamella will be extracted. The Pt layer protects the material underneath from the gallium (Ga) ions of the focused ion beam (FIB) microscope. c) and d) Extraction of the lamella from the vdW stack on the Si/SiO_2 substrate. e) The finished lamella was transferred and attached to the STEM holder.

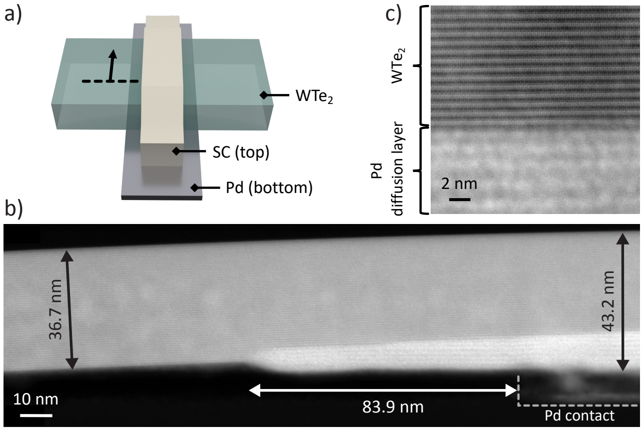

Figure 6.2. Pd diffusion inside the WTe_2 crystal. a) Illustration of the WTe_2 crystal on a single Pd bottom contact including a superconducting edge contact from the top. The direction of the cut lamella for the STEM image is indicated by the dashed line, and the viewing direction of the image is indicated by the arrow. b) High resolution STEM image taken at the edge of the Pd bottom contact (indicated by the gray dashed line at the bottom right). A bright diffusion layer at the interface between the Pd bottom contact and the WTe_2 crystal has formed. Black arrows indicate the thickness of the WTe_2 crystal, and the white arrow shows the lateral extent of diffusion in WTe_2 from the edge of the original Pd contact. c) Zoom-in STEM image of the interface between the WTe_2 crystal and the diffusion layer.

6

The presence of the diffusion layer in WTe_2 creates a pronounced swelling of the crystal, as highlighted by two thickness measurements of the WTe_2 flake in Fig. 6.2 b): inside the junction and on top of the Pd bottom contact. For pristine WTe_2 we extract an inter-layer spacing of $c \sim 7.4\,\text{Å}$ that agrees with the literature value [186, 187]. Inside the diffusion layer the perceived layer spacing has doubled to $c \sim 14.8\,\text{Å}$. We connect the change in the layer spacing with the formation of a new crystal structure at the interface of WTe_2 and Pd, rather than the mere intercalation of the original crystal by Pd. The formation of a new structure is further supported by Fig. 6.2 c), where we see that the transition between the newly formed crystal and WTe_2 is very sharp and takes place on a single layer scale. We also would like to note that the diffusion forming the new structure is quite anisotropic. Laterally, along the vdW layers, the diffusion layer extends $\sim 84\,\text{nm}$ while vertically, perpendicular to the vdW layers, it only reaches $\sim 16\,\text{nm}$ at its maximum.

The lateral diffusion inside the JJ can diminish the length of the JJ, which could be especially prominent for the shorter junctions.

In the next section we analyze the atomic composition of the diffusion layer using energy dispersive x-ray (EDX) analysis. Figure 6.3 a) on the left shows a STEM image taken at the position of a superconducting niobium (Nb) top-contact in this device. For better orientation, the location is illustrated in b). From the bottom to the top, the faded Pd bottom contact, the Pd diffusion layer adjacent to the pristine WTe_2 crystal, and the Nb top contact are visible. Towards the right, EDX spectra of the elements in this slab are shown. Nb (turquoise) and the sticking layer for the Pd bottom contacts, titanium (Ti) are at their expected positions. Qualitatively, the concentration of tungsten (W) and tellurium (Te), represented in red and yellow, respectively, are maximal in the unchanged WTe_2 crystal but reduced in the diffusion layer. Pd (in blue) has diffused through the entire WTe_2 crystal and is the dominating element inside the structurally changed layer. The concentration of Pd at the position of the original bottom contact is diminished, suggesting that depletion of the available material stopped the further growth of the diffusion layer.

A quantitative analysis of the crystal composition is shown in Fig. 6.3 b), following a trace indicated by the red arrow in the STEM image in Fig. 6.3 a). The ratio of W:Te is $\sim$ 1:2 and remains the same throughout most of the thickness. For Pd, two distinct concentration levels are visible, a high level of $\sim$ 60% that coincides with the structurally changed lattice and a second low level of $\sim$ 20% inside the preserved WTe_2 crystal. The ratio of Pd:Te $\sim$ 3:1 suggests that the diffusion layer is not one of the known superconductors PdTe or $PdTe_2$ [188–191]. In the unchanged WTe_2 crystal above, Pd likely intercalates the vdW layers. So possibly, a threshold concentration of Pd is required to trigger the crystallographic change, such that the vertical extention of the diffusion layer is determined by the interplay of available Pd and thermal activation energy. The remaining Pd concentration above the $PdTe_x$ layer quickly decays in the direction parallel to the vdW layers and extends $\sim 50\,\mathrm{nm}$ laterally beyond the structurally changed diffusion layer, as shown in Fig. 6.4.

6.3. Heat mediated diffusion during the stacking process

Having shown that Pd does indeed diffuse from the bottom contact into the WTe_2 crystal above, the question remains when the diffusion takes place. The process can most likely be narrowed down to a fabrication step that involves heating. Possible steps include the release of the PC/PDMS stamp after stacking, the baking out of the PMMA mask for e-beam lithography or more subtle situations during the etching or deposition of metals. In the following we provide evidence that the diffusion of Pd into WTe_2 must happen already during the stacking process of the device.

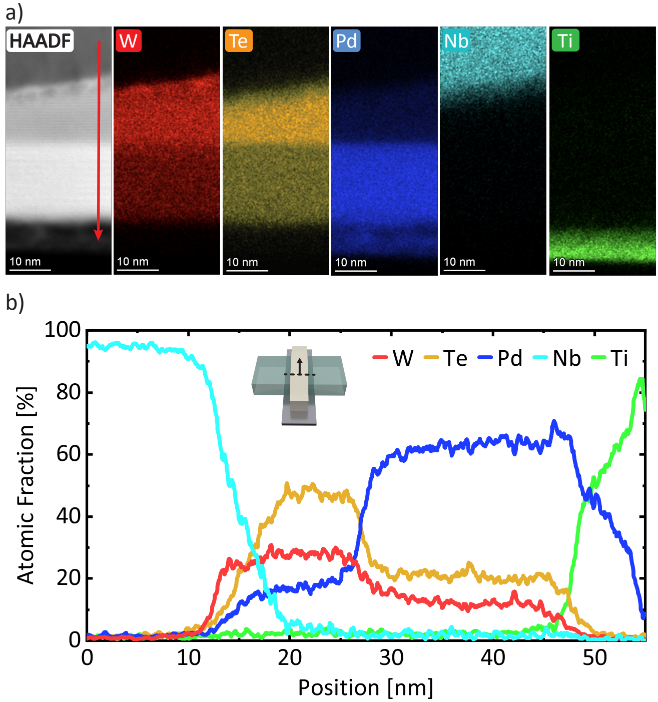

Figure 6.3. EDX analysis of the Pd diffusion. a) STEM image with the direction of the line cut in panel b) indicated by a red arrow. Presented towards the right is the EDX analysis with elements existent in the device. Moving from the bottom to the top, the Pd bottom contact is followed by a highly Pd interspersed WTe_2 layer that has structurally changed. Above, the crystal transitions sharply into the original crystal structure. b) EDX line cut along the direction indicated in panel a), with the position of the investigated lamella marked in the insert. Pd has diffused in the vertical direction through the entire WTe_2 crystal, with a sharp concentration increase in the structurally changed area that coincides with the STEM image.

6

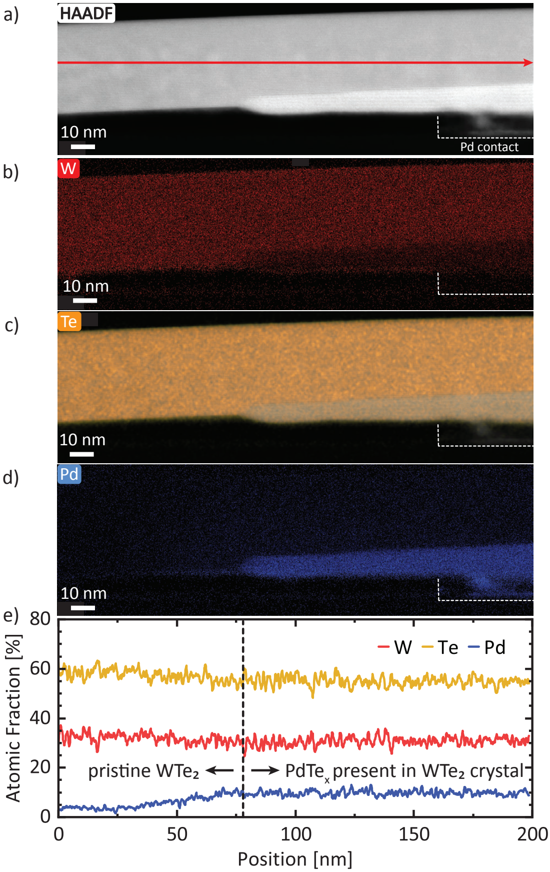

Figure 6.4. Horizontal diffusion of Pd inside the pristine WTe_2 crystal. a) - d) HAADF image and EDX spectra for the elements W, Te and Pd. The extend of the former Pd bottom contact is indicated by the white dashed line. e) Horizontal line-cut through the EDX spectra taken along the direction of red arrow in a) inside the pristine WTe_2 crystal above the $PdTe_x$ layer. The extend of the $PdTe_x$ layer is marked by a vertical dashed line. The diffused Pd concentration inside pristine WTe_2 decreases close to zero at $\sim 50\,\text{nm}$ beyond the $PdTe_x$ diffusion layer.

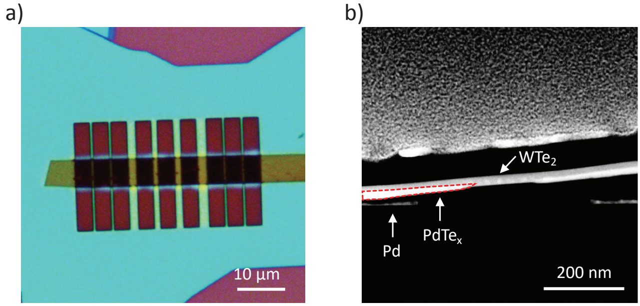

Figure 6.5. Diffusion of Pd during the stacking process of the vdW stack. a) Optical image of the finished vdW stack after PC removal. WTe_2 is lifted from the Pd bottom contacts, as seen by the color change of hBN in the large spacing between Pd bottom contacts. b) HAADF image of the same device, showing the WTe_2 being lifted off the Pd bottom contacts. A swollen $PdTe_x$ crystal structure has visibly formed inside the WTe_2 crystal, implying that Pd diffusion must happen already during the PC release at $T = 155\,°\mathrm{C}$ after the stacking process.

Figure 6.5 a) shows an optical image of a finished stack after the removal of PC resides but before etching and deposition of the superconducting contacts. The color change of hBN in between the Pd bottom contacts, compared to the outer edges, indicates that the WTe_2 flake is lifted off the bottom contacts at this stage. Figure 6.5 b) presents a HAADF STEM image of the same stack, taken along a JJ. Visible are the two Pd bottom contacts at the left and right end of the image, with the WTe_2 spanning across them above. The WTe_2 flake is confirmed to be lifted off the Pd bottom contacts, as seen by the rising slope relative to the horizontal bottom contacts. Yet, a $PdTe_x$ diffusion layer has clearly formed inside the crystal and is outlined by a red dashed line for the left side of the crystal. Therefore, Pd diffusion must happen already at the end of the stacking process when the finished stack is being released on top of the Pd bottom contacts and heated up to $T = 155\,°\mathrm{C}$ for $\sim 10\,\mathrm{min}$.

6.4. Pd diffusion along crystal edges

Next we investigate the uniformity of the $PdTe_x$ diffusion layer along the width of the Josephson junction. For this, we have analyzed several lamellas that are oriented perpendicularly to the direction of the current in the JJ. The regions near the physical edges of WTe_2 are of particular interest, since additional Pd is available there due to the Pd bottom contacts extending beyond the crystal.

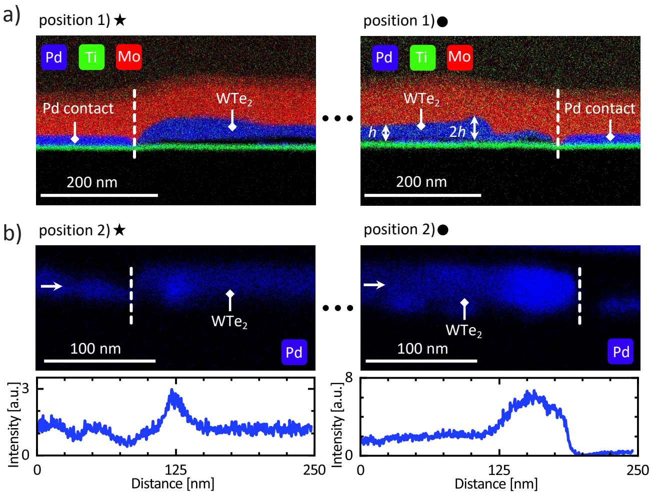

Figure 6.6. Enhanced Pd diffusion along the edges of the WTe_2 crystal. a) EDX analysis of a cross section taken on the Pd contact along position 1), as indicated in the schematics of Fig. 6.7 a). The given sample was equipped with a superconducting MoRe contact, evidenced by the Mo EDX signal in red. The left and right image correspond to the crystal edges marked by $\star$ and $\bullet$ in the schematics, respectively. Visible is the swelling of WTe_2 to a thickness of $\sim$ 2h at the edge, compared to the bulk thickness $\sim$ h, indicated in the right panel. b) EDX signal and extracted intensity profile taken towards the inside of the junction, indicated by position 2) in Fig. 6.7 a). The left and right image correspond to positions $\star$ and $\bullet$ of the WTe_2 crystal, respectively. Visible in the EDX data is an increased intensity of the Pd signal at the edges of the crystal compared to the bulk. The increased Pd concentration is also visible by the enhanced EDX signal in the line cuts taken along the direction pointed out by the horizontal arrow.

The first lamella was cut out through the middle of the bottom Pd contact in a sample with additional, this time molybdenum-rhenium (MoRe), top contacts, as illustrated by position 1) in Fig. 6.7 a). Figure 6.6 a) presents two EDX spectra obtained at the two edges marked by $\star$ and $\bullet$ in the previous illustration. Outside the WTe_2 flake we observe a layer of Pd with uniform thickness sandwiched between the MoRe top and the Ti bottom layer. Interestingly, inside WTe_2 near the edges, the thickness h of the $PdTe_x$ diffusion layer increases within a region of $\sim$ 100 nm away from the edge, as marked in the right spectrum of Fig. 6.6 a). Further from the edges, Pd is evenly

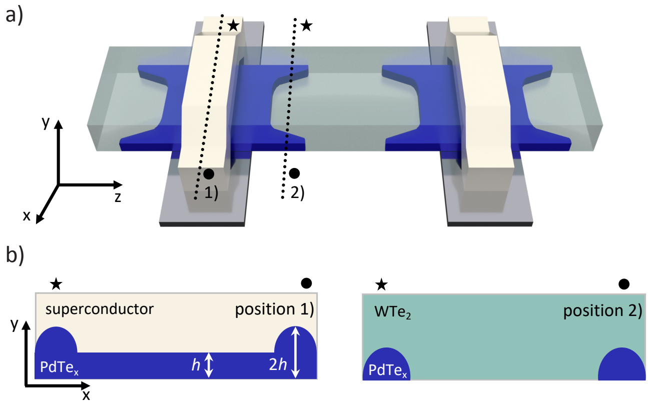

Figure 6.7. Effective diffusion model of PdTe$_x$. a) Illustration of the inhomogeneous diffusion profile of PdTe$_x$ inside the WTe$_2$ host crystal. The self-formed PdTe$_x$ layer is drawn in blue inside the host crystal. b) Cross sectional cuts through the illustration along position 1) and 2) in a). The edges are marked by $\star$ and $\bullet$ for orientation (compare to Fig. 6.6).

distributed throughout the WTe$_2$ crystal. The difference of PdTe$_x$ thickness on the edges and in the middle of WTe$_2$ reaches a factor of ~ 2.

The increase in thickness of PdTe$_x$ near the edges can be intuitively explained taking into account the fabrication procedure. During the last step of stacking, when the substrate is heated up to 155 °C to release the hBN/WTe$_2$ stack, the formation of the PdTe$_x$ takes place. In WTe$_2$ far away from the edges, this process stops before reaching the full thickness of the flake due to the depletion of available Pd. Near the edges, due to the availability of additional Pd, this process continues potentially even through the whole thickness of WTe$_2$. Afterwards, the top WTe$_2$ layers, not transformed to PdTe$_x$, are etched away during CHF$_3$/O$_2$ plasma etching of hBN prior to the deposition of the superconductor. This explanation is further corroborated by the uniform Pd concentration in Fig. 6.6 a) in contrast with the step in concentration in Fig. 6.3 b).

The increased Pd availability on the edges of the WTe$_2$ has the potential not only to increase the PdTe$_x$ thickness, but also to provide further diffusion inside the Josephson junction. To check this, we fabricated a second lamella from another sample, which is cut inside the Josephson junction, close to the end of Pd bottom contact, as shown as position 2) in Fig. 6.7 c). Visible in the EDX spectrum in Fig. 6.6 b) is an elevated intensity of Pd compared to the bulk at both ends of the crystal, highlighted by line cuts through the spectra along the horizontal arrows. This indicates that $PdTe_x$ is indeed penetrating further inside the junction along the edges of WTe_2, as visualized in Fig. 6.7 a).

We can roughly estimate the extent of the $PdTe_x$ diffusion along the edges, assuming that an increase by a factor of 2 in thickness h of $PdTe_x$ on the edges, as compared to the bulk (see Fig. 6.7 b)), yields the same increase in the diffusion inside the JJ along the edge. Taking from Fig. 6.2 b), that the $PdTe_x$ layer extends ~ 85 nm inside the junction in the bulk, we would expect it to extend ~ 170 nm along the edges. This diffusion could generate signatures of "artificial" edge supercurrents which are not due to a topological state. Nonetheless, evidence of topological hinge states in WTe_2 has been observed in combination with superconducting niobium contacts [16, 101], where no edge diffusion is expected.

6.5. Josephson junctions with fully superconducting contacts

During the formation of $PdTe_x$ in WTe_2, the majority of the Pd from the bottom contacts is depleted (see Figs. 6.2 - 6.6), thus creating a low quality interface between bottom contacts and the newly formed Josephson junction. In this section we demonstrate a method to harness the full potential of the high quality Josephson junction formed in WTe_2 with Pd diffusion by employing additional superconducting contacts from the top.

6

The fabrication process follows the description in chapter 3 and appendix A. After obtaining the stack, superconducting leads are patterned via standard e-beam lithography and sputtered onto the sample, after etching through the top hBN with CHF_3/O_2 plasma. Prior to the deposition of MoRe superconducting leads we perform a short Ar milling inside the sputtering chamber to remove the oxide layer from WTe_2. In order to avoid degradation of the JJs due to etching, the superconducting top contacts are separated by a distance of l_{Pd} $\sim$0.5 µm from the edge of the Pd bottom contacts, as indicated in the schematics in Fig. 6.8 a) on the right. Figure 6.8 a) shows a finished device with top MoRe leads and its fabricated layer sequence to the right.

Measurement of the device is performed in a quasi four-terminal setup, illustrated in Fig. 6.8 a). In this configuration, the measured differential resistance includes the contribution from the Josephson junction and the resistances of the interfaces between the MoRe and superconducting $PdTe_x$, but excludes the line resistances in the cryostat. Figures 6.8 b) and c) show the $dV/dI(I)$ and $V(I)$ dependencies, measured on a 1 µm long Josephson junction, with their behavior being representative for a number of samples we have studied. The curves reveal several abrupt transitions with current. Steps at $I \sim \pm 11$ µA have minimal hysteresis and correspond to the switching of superconducting $PdTe_x$ to the normal state or alternatively to a Josephson junction that has potentially formed at the interface of the vdW stack with MoRe [192].

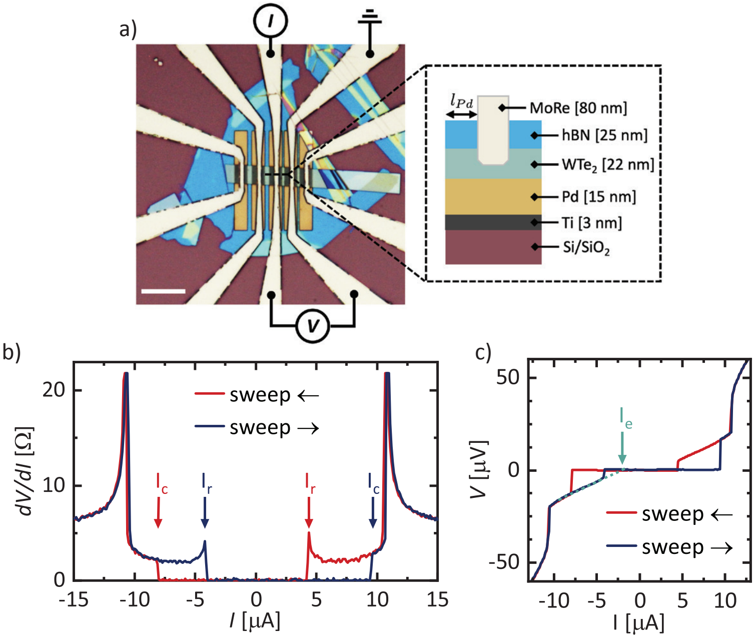

Figure 6.8. Device with superconducting contacts. a) Optical image of the device with an illustration of the quasi four-terminal measurement setup. The fabricated layer sequence is shown on the right. The scale bar is 10 µm. b) dV/dI curves at zero magnetic field of a JJ with superconducting contacts for two different sweep directions of the bias current. The hysteretic switching current depending on the sweep direction is visible from the shift of the critical current I_c and the re-trapping current I_r. c) $V(I)$ curves corresponding to the data in panel b). The excess current I_e is evaluated from the intersection of the extended $V(I)$ curve to zero voltage.

The observed vanishing resistance at low bias currents by itself is not sufficient to ensure that the fabricated device performs indeed as a JJ. Potentially, the inhomogeneous diffusion of $PdTe_x$ could lead to a closed superconducting path through the weak link. In order to rule out this option, we study the dependence of dV/dI on the bias current I and the perpendicular magnetic field B, as shown in Fig. 6.9 a). Visible is a periodic “Fraunhofer”-like interference pattern that is a key signature of the Josephson effect. The oscillation periodicity $\delta B = 0.13\,\mathrm{mT}$ is connected to a flux quantum Φ_0 threading the effective junction area $A_{\mathrm{eff}} = w \times \ell_{\mathrm{eff}}$, with $w = 4.3\,\mu\mathrm{m}$ being the width of

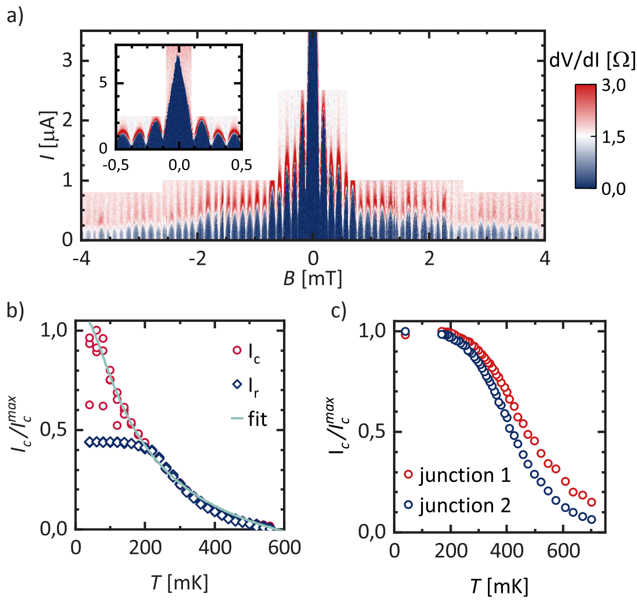

Figure 6.9. Reduced heating effects in JJ with superconducting contacts. a) dV/dI as a function of the bias current I and the perpendicular magnetic field B, following the "Fraunhofer" pattern expected for a Josephson junction. The insert shows the full range of the central lobe around $B = 0$. b) Temperature dependence of the switching and re-trapping currents I_c and I_r, respectively, of the same device as in Fig. 6.8 b). The data $I_c(T)$ is fitted in the scope of a diffusive long junction, plotted in light green. c) Switching current I_c as a function of temperature T for two different JJs that are contacted only through Pd bottom contacts.

the junction and ℓ_{eff} being the effective length. The calculated ℓ_{eff} ~3.8 μm exceeds the physical junction length of ~1 μm. However, it can be explained by the contact geometry, assuming that half of the magnetic flux through the superconducting contacts is screened into the junction [193]. Additionally, a close look at the amplitude of consecutive lobes reveals a non-monotonous behavior, reminiscent of an even-odd effect. A non-sinusoidal current-phase relation of the junction [111] or an inhomogeneous current distribution [193], originating from the diffusion profile of $PdTe_x$, can create this feature.

Having established the Josephson effect through WTe_2, we take a closer look at the lower current behavior observed in Fig. 6.8 b) and c). First, in the superconducting branch of the JJ, the differential resistance is zero, implying that there is no measurable contribution of the MoRe/PdTe$_x$ interfaces. Second, in contrast to the previously studied devices with solely Pd leads [111], the switching behavior is highly hysteretic. The transition from the superconducting to the resistive branch, denoted by the switching current I_c, takes place at absolute current values higher than those of transition in the opposite sweep direction, denoted by the re-trapping current I_r, highlighted in Fig. 6.8 b).

Even though the hysteretic switching of the Josephson junction is most commonly explained by the junction being in the underdamped regime [22], we would argue that in our case overheating [194, 195] plays the dominating role. Starting from the superconducting branch, no heat is dissipated in the Josephson junction before switching to the resistive branch. In contrast, lowering the bias current from the resistive branch includes dissipation of heat in the normal weak link, leading to a higher electron temperature. This explanation is corroborated by the temperature dependence of I_c and I_r shown in Fig. 6.9 b). Moving from high towards low temperatures, I_c and I_r both increase continuously down to $T \sim 220\,\mathrm{mK}$, when I_r begins to saturate while I_c remains increasing. Furthermore, this explanation is additionally supported by the devices with only Pd contacts. There, due to the normal Pd contacts remaining dissipative at all times, I_c saturates at low temperatures, as shown in Fig. 6.9 c).

Next, we characterize the quality of the PdTe$_x$/WTe$_2$ interface. Compared to conventional superconducting contacts to WTe$_2$, the Josephson effect in junctions formed by Pd interdiffusion is found to be more robust in terms of junction length and magnetic field resilience [111]. Additionally, due to reduced heating effects, the devices proposed here support a critical current density twice as large compared to conventional contacts [101] at four times the junction length. The 1 µm long junction presented in Fig. 6.8 b) maintains the Josephson effect with a critical current density j_c of up to $j_c > 10^8\,\mathrm{A\,m^{-2}}$ while comparable junctions with an even shorter length of up to 230 nm and conventional superconducting contacts are found to be limited by $j_c \sim 1\times10^7\,\mathrm{A\,m^{-2}} - 5\times10^7\,\mathrm{A\,m^{-2}}$ [101].

Further, from Fig. 6.9 b) we see that I_c is suppressed at 0.6 K, which is lower than the critical temperature $T_c = 1.2\,\mathrm{K}$ [143] of the formed PdTe$_x$. We connect this reduction with the great length of the junction and fit for this reason $I_c(T)$ with an expression for a long diffusive junction [194, 196]

$$I_c = \eta \frac{aE_{\mathrm{Th}}}{eR_{\mathrm{N}}} \left[1 - b\, \exp\left(\frac{-aE_{\mathrm{Th}}}{3.2k_{\mathrm{B}}T}\right)\right]. \tag{6.1}$$

Here, a and b are constants equal to 10.82 and 1.30, respectively, k_{B} is the Boltzman constant and E_{Th} is the Thouless energy. The empirical pre-factor $\eta \in [0, 1]$ can be interpreted as a measure for the interface quality, scaling the maximum I_c. The data in Fig. 6.9 b) are well described by the model which yields $\eta = 0.5$ and $E_{\mathrm{Th}} = 3.87\,\mu\mathrm{eV}$. A similar fit procedure for the data in Fig. 6.9 c), obtained from a junction with only Pd contacts,is not reliable, as $I_c(T < 400$ mK) is limited by heating effects and deviates strongly from the theoretical prediction.

The evaluation of the interface transparency is corroborated by the excess current I_e, extracted from the $V(I)$ curve in Fig. 6.8 c). We extrapolate I_e after the transition from the superconducting to the resistive branch and obtain [184] $I_e R_N/\Delta$ ~0.03, using $\Delta = 1.76 k_B T_c = 182\,\mu\mathrm{eV}$ [143]. In the framework of the Octavio-Tinkham-Blonder-Klapwijk theory [32, 33], this relates to a junction transparency of $T = 1/(1 + Z^2)$ ~0.5, with Z ~1.1.

At this point we would like to comment on the role of R_N in the two analytical models of the preceding analysis yielding a transparency of ~ 0.5. The bulk conductivity of WTe_2 increases with flake thickness [150]. These additional bulk modes in the normal state shunt R_N, but do not participate in superconducting transport of the long junction due to their fast decay $I_{c,\mathrm{bulk}} \propto \ell^2/L_w^3$ compared to ballistic edge modes $I_{c,\mathrm{edge}} \propto 1/L_w$ [48], with ℓ being the electronic mean free path. This phenomenon has also been reported in JJs formed of the topological material Bi_2Se_3 [197]. The extracted transparency is therefore systematically underestimated and serves only as a lower bound to the real value.

6.6. Conclusion

6

We have demonstrated a robust method to form atomically sharp superconducting contacts to WTe_2 mediated by Pd diffusion during stacking. Josephson junctions formed by these contacts are highly transparent. Given recent reports of similar processes in BiSbTe [184, 185] this method could be a promising approach for other topological candidates based on Te compounds. We have further demonstrated that the diffusion inside the host crystal could be non-uniform, generating false signatures of superconducting edge currents. Therefore, caution has to be exercised in the evaluation of a diffusion driven Josephson junction, when assigning it to a topological superconductor. Furthermore, we have proposed a method to avoid overheating in transport through Pd diffusion mediated Josephson junctions by employing superconducting leads.

7 Current-phase relation of a WTe_2 Josephson junction[1]

In the previous chapter we have established the formation of $PdTe_x$ as the origin of superconductivity in the studied WTe_2/Pd heterostructures. Next, we embed two such Josephson junctions into an asymmetric SQUID loop in order to measure the current-phase relation of the a Josephson junction. The measured critical current is highly affected by inductance effects, despite the loop inductance being negligible. We assign the inductive contribution to the superconducting $PdTe_x$. We model our data by maximizing the supercurrent in the SQUID loop and find the 1.5 µm long junction is best described in the short ballistic limit. Our data highlights the complexity of inductance effects that reach beyond the loop inductance and can even give rise to topological signatures in transport measurements.

[1] This chapter has been published in similar form in Ref. M. Endres *et al.* [198]

7.1. Introduction

The fingerprint of a JJ is the current-phase relation (CPR), the dependence of the supercurrent on the phase difference between the superconducting contacts. The CPR directly reflects the transparency of the junction and therefore the underlying transport mechanism with which Cooper-pairs are transferred across the weak-link. In an ideal topological weak-link, perfect Andreev-reflection is expected [199] because spin-momentum locking in the edge states prohibits normal electron-reflection at the interface with the superconductor. In this case, the supercurrent is carried ballistically by protected hinge states that manifest themselves in a sawtooth-shaped CPR, as shown in Ch. 2.1.4.

We have presented in the previous Ch. 6 the inhomogeneous diffusion profile of $PdTe_x$, with an increased extent along the crystal edges compared to the bulk of the WTe_2 host crystal. The open question remains whether the previously observed supercurrent flowing along the crystal edges in WTe_2 flakes [111] originates from topological hinge states or from spatially inhomogeneous $PdTe_x$.

In this chapter, we combine JJs based on Pd-induced superconductivity in WTe_2 with external superconducting leads. We use the fabrication technique that was developed in the previous Ch. 6, which makes it possible to integrate the junctions into an on-chip superconducting circuit architecture. We embed two JJs into an asymmetric superconducting quantum interference device (SQUID), which allows to investigate the CPR of the weak JJ. The observed critical current appears as carried by ballistic edge states and even reveals a 4π periodicity, predicted for a topological JJ [47].

Contrary to a topological explanation, we find that the features originate from strong inductance effects of the self-formed superconducting $PdTe_x$ [175]. In order to include screening effects, we model our data by maximizing the supercurrent in the SQUID loop. The model suggests that the critical current of our 1.5 µm long junction is best reproduced in the short ballistic limit despite its long physical length.

7.2. Inductance effects in single Josephson junctions

We start this chapter with the study of single JJs before we present the more complex data of the SQUID measurement. In the following section, we investigate the magneto-transport in JJs with varying length. We show that transport in short junctions is defined by the kinetic inductance and that it shifts towards the Josephson regime with increasing junction length.

Figure 7.1 a) shows an optical image of the device with its multiple JJs on an elongated WTe_2 flake. The external superconducting contacts are formed by aluminium as described in App. A.4.5. A cross section through the stack is illustrated to the right.

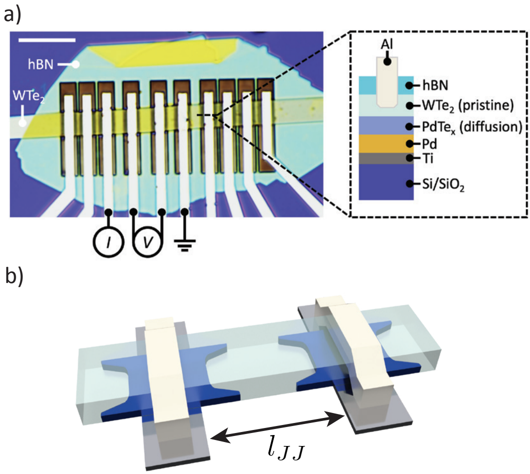

Figure 7.1. Junction array with varying length. a) Optical image of multiple JJs formed in a WTe_2 crystal. An illustration of the quasi four-terminal measurement scheme is illustrated at the bottom of the image. Visible is the elongated WTe_2 flake in horizontal direction, lying on vertically oriented Pd bottom contacts. The scale bar is 10 µm. The fabricated layer sequence of the heterostructure across the black dashed line is shown on the right. b) Illustration of a single Josephson junction with the effective diffusion profile of $PdTe_x$ highlighted in blue.

Figure 7.1 b) recalls the spatial distribution of $PdTe_x$ with its increased extent along the crystal edges of WTe_2 compared to the bulk. In the following chapter we want to focus on the signatures in electronic transport that are attributed to the diffusion crystal. First, the enhanced diffusion length of the compound along the edges of WTe_2 could lead to an increased role of the edges in the Josephson transport. This is beneficial in case of topological edge/hinge states, since it would diminish the contribution from trivial bulk states. Second, the diffusion channels could form a nano-inductor with high kinetic inductance $L_\mathrm{K} \propto l/(wd)$ [200], governed by the length l, width w and thickness d of the diffusion strip.

We have fabricated a series of JJs with different spacing between the Pd bottom contacts, ranging from $l_\mathrm{JJ} = 600\,\mathrm{nm}$ to $2\,\mu\mathrm{m}$. DC-current measurements are performed in four-terminal configuration, as illustrated in Fig. 7.1 a), with a standard lock-in technique at the base temperature of the cryostat $\sim 30\,\mathrm{mK}$. Figures 7.2 and 7.3 summarize the differential resistance as a function of ap-

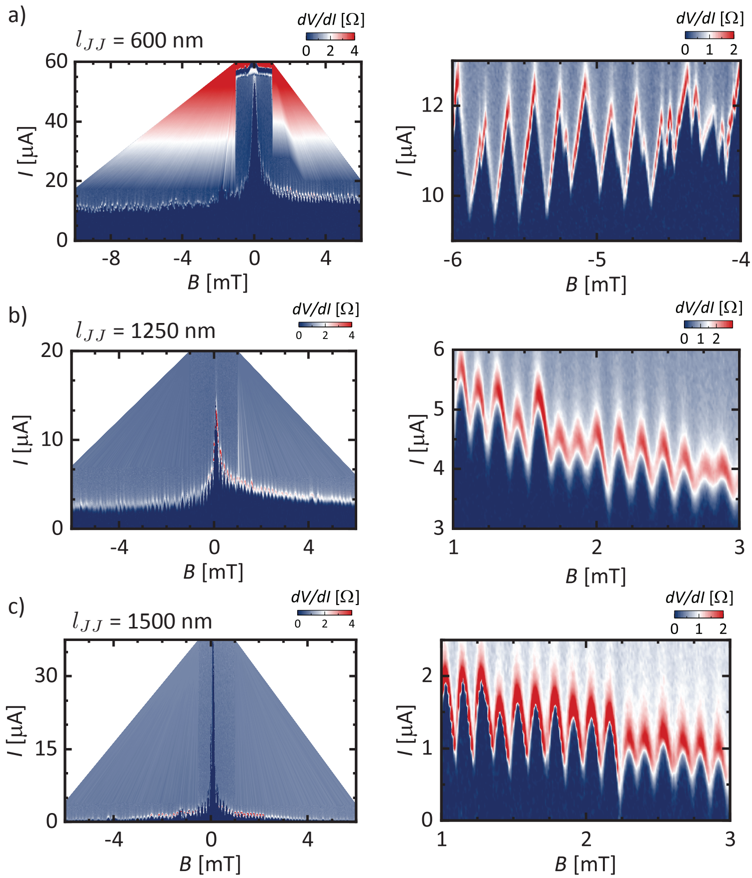

Figure 7.2. Length dependent transport in Josephson junctions. Differential resistance as a function of perpendicular magnetic field and applied bias current for JJs with lengths a) $l_{\mathrm{JJ}} = 600\,\mathrm{nm}$, b) $l_{\mathrm{JJ}} = 1250\,\mathrm{nm}$ and c) $l_{\mathrm{JJ}} = 1500\,\mathrm{nm}$.

plied perpendicular magnetic field and current bias for the different junctions. Each row presents a junction length with the full range data shown on the left and a zoom-in of the data on the right. We begin with the shortest junction length $l_{\mathrm{JJ}} = 600\,\mathrm{nm}$ in Fig. 7.2 a). On a macroscopic scale, the critical current envelope, at which the junction switches from zero to finite

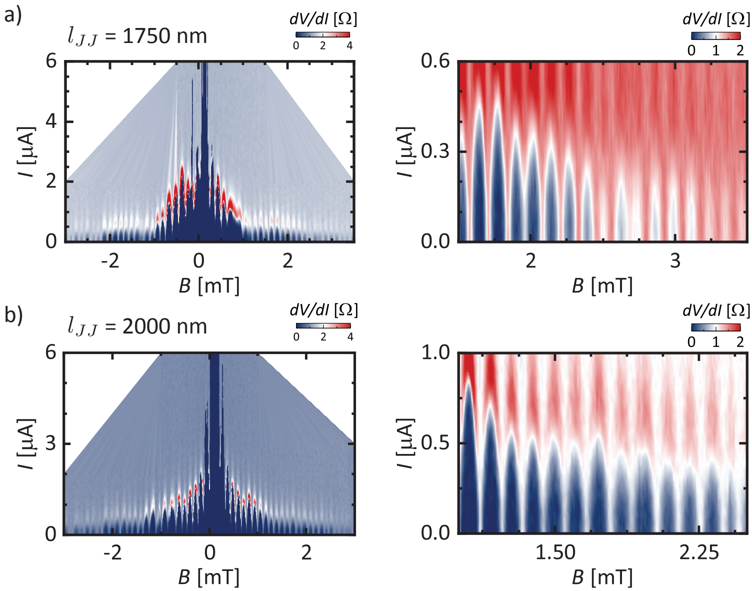

Figure 7.3. Length dependent transport in Josephson junctions. Differential resistance as a function of perpendicular magnetic field and applied bias current for JJs with lengths a) $l_{\mathrm{JJ}} = 1750\,\mathrm{nm}$ and b) $l_{\mathrm{JJ}} = 2000\,\mathrm{nm}$.

7

resistance, peaks sharply around zero magnetic field and decays only slowly towards higher field values. A zoom in to the data, presented in the right panel of Fig. 7.2 a), reveals sharp sawtooth-like oscillations that are aperiodic in magnetic field. The oscillation nodes are lifted from zero. The data resemble the characteristics of an asymmetric SQUID that is formed inside the WTe_2 junction by the spatially inhomogeneous $PdTe_x$ along the edges of the crystal. The asymmetry in critical current of the two junctions, I_c^r/I_c^w, can be quantified by the oscillation range in current amplitude between $I_c^{low} \sim 9.7\,\mu A$ and $I_c^{high} \sim 12.4\,\mu A$. We find $I_c^r/I_c^w = (I_c^{high} + I_c^{low})/(I_c^{high} - I_c^{low}) \sim 8.1 \gg 1$ [111], with I_c^r and I_c^w denoting the high and low critical current of the reference and weak junction , respectively.

With increasing junction length, shown in direction of the lower panels in Fig. 7.2 and continued in Fig. 7.3, the overall shape of $I_c(B)$ resembles a "Fraunhofer" pattern of a single JJ in magnetic field. In more detail, with increasing junction length, the oscillation amplitude reduces and the shape of the oscillations in magnetic field becomes more sinusoidal. Furthermore, the nodal offset from zero vanishes.

In an asymmetric SQUID, such as it is the case for the shortest junction in Fig. 7.2 a), I_c as a function of magnetic field maps the CPR of the weak JJ with smaller critical current [201]. The sawtooth-like CPR could be interpreted as being in the ballistic long junction limit, originating from the topological edge states of the material [48]. We argue, however, that this interpretation is unlikely to be the case in the presented device when the aperiodicity and inconsistent change in amplitude of the oscillations are taken into account. Instead, the linear behavior in magnetic field is attributed to inductance effects in the junction [202–206]. A detailed analysis of an inductive SQUID is performed in the following Sec. 7.5.

The evolution of $I_c(B)$ with junction length, from a sawtooth-like to a sinusoidal interference pattern, can be explained consistently in the framework of a SQUID with flux screening that is formed by the extended $PdTe_x$ arms along the WTe_2 crystal edges. We assume that the $PdTe_x$ diffusion along the edges is similar for all junction lengths and gives a constant contribution to the kinetic loop inductance L_K. As the junction length increases, so does the ratio between Josephson inductance L_J and kinetic inductance of the diffusion layer L_K:

$$\frac{L_J}{L_K} = \frac{\Phi_0}{2\pi L_K I_c}. \tag{7.1}$$

Longer junctions, due to their smaller value of I_c, have an increased Josephson inductance. If L_J exceeds the kinetic inductance that originates from the $PdTe_x$ diffusion crystal, the phase difference over the junction will be determined by the external flux ϕ_x and a sinusoidal interference pattern is observed.

7.3. Asymmetric SQUID devices

We have fabricated asymmetric SQUIDs [201], in which the total critical current reflects the properties of the weak junction, while the phase across the reference junction with high critical current $I_c^r \gg I_c^w$ remains constant. In our experiment, both JJs are formed in the same needle-shaped WTe_2 flake of width $w = 1.5\,\mu m$.

An optical image of the device with superconducting Nb top-contacts is shown in Fig. 7.4 a). The layer sequence of the fabricated vdW stack is illustrated in Fig. 7.4 b). The device includes two separate SQUID loops. In the following sections we will focus on the lower one, enclosed by a dashed line in panel a). The asymmetry in critical current I_c of the two involved junctions is achieved by setting the spacing between the Pd bottom contacts $l_w = 1.5\,\mu m$ and $l_r = 0.5\,\mu m$ for the weak and reference junction, respectively, as sketched in the illustration on the right of Fig. 7.4 a). The superconducting loop, embedding the strong and weak JJs, is formed by etching through hBN and

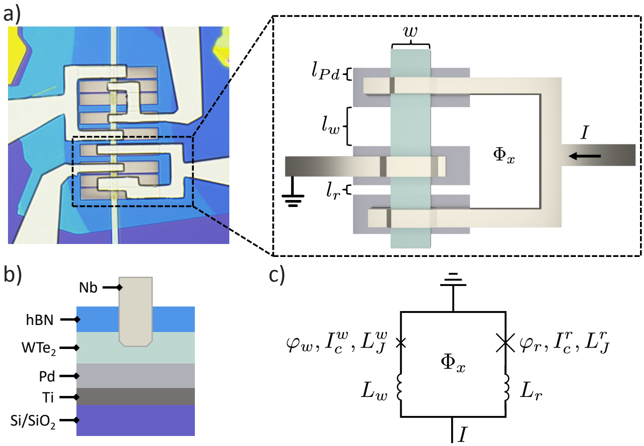

Figure 7.4. Asymmetric SQUID realization in a vdW stack. a) Optical image (scale bar is 10 µm) and illustration of the SQUID loop with both, the reference and the weak junction fabricated on the same WTe_2 flake. The device is sourced by a DC current I and an external magnetic flux Φ_x. b) Fabricated layer sequence of the vdW materials. The exfoliated materials hBN and WTe_2 are stacked on top of pre-patterned Pd bottom contacts. An etching step opens up the top hBN in order to sputter the superconducting Nb contacts that form the embedding SQUID loop. c) Schematic of the SQUID including the junction and loop properties.

sputtering the superconductor niobium (Nb) on top of the stack. The JJ interface is separated by $l_{\mathrm{Pd}} \approx 0.5\,\mu\mathrm{m}$ from the etched superconducting contact to preserve the high contact transparency [175]. The Nb leads are between 2.2 µm and 3 µm wide and 100 nm thick. Figure 7.4 c) provides an effective electrical circuit diagram and specifies the junction phase φ_i, critical current I_{c}^i and Josephson inductance L_{J}^i with $i = w, r$ representing the weak and reference junction, respectively. An additional inductance per SQUID arm L_{w} and L_{r} is explicitly included and used in the later analysis of the experimental data.

The critical current of the device $I_{\mathrm{c}}(\varphi_{\mathrm{w}}, \varphi_{\mathrm{r}}) = I_{\mathrm{c}}^{\mathrm{w}} f_{\mathrm{w}}(\varphi_{\mathrm{w}}) + I_{\mathrm{c}}^{\mathrm{r}} f_{\mathrm{r}}(\varphi_{\mathrm{r}})$ is the sum of the individual currents I_{w} and I_{r} through the two branches of the loop, defined by the critical current I_{c}^i and the normalized CPR f_i of the i^{th} Josephson junction. The total flux threading the loop, Φ_{tot}, connects the phase differences across the two JJs $\varphi_{\mathrm{w}} - \varphi_{\mathrm{r}} = \phi_{\mathrm{tot}} = 2\pi\Phi_{\mathrm{tot}}/\Phi_0$. The asymmetry $I_{\mathrm{c}}^{\mathrm{r}} \gg I_{\mathrm{c}}^{\mathrm{w}}$, pins $\varphi_{\mathrm{r}} = \varphi_{\mathrm{r}}^{\mathrm{max}}$ at a fixed phase, for which $I_{\mathrm{c}}^{\mathrm{r}}$ is maximized [54, 201].

The normalized CPR of the weak junction f_w can be deduced from the measurement of

$$I_\mathrm{c}(\phi_\mathrm{tot}) \sim I_\mathrm{c}^\mathrm{w} f_\mathrm{w}(\varphi_\mathrm{r}^\mathrm{max} + \phi_\mathrm{tot}) + I_\mathrm{c}^\mathrm{r} f_\mathrm{r}(\varphi_\mathrm{r}^\mathrm{max}). \tag{7.2}$$

In the experiment, the external flux $\Phi_\mathrm{x} = BA_\circ$ is controlled by applying a perpendicular magnetic field B, that threads the effective loop area $A_\circ = 186\,\mu\mathrm{m}^2$. The Meissner screening of the enclosing superconductor was taken into account by including half of its width into the loop area. In general, the total flux threading the loop

$$\phi_\mathrm{tot} = \phi_\mathrm{x} + \frac{2\pi(L_\mathrm{r}I_\mathrm{r} - L_\mathrm{w}I_\mathrm{w})}{\Phi_0}, \tag{7.3}$$

can differ strongly from ϕ_x, due the contribution of the currents I_r and I_w passing through the inductances in the SQUID arms, L_r and L_w. We note that, while a screening current can distort the flux dependence of the critical current, it does not change its periodicity [22].

7.4. Counter measurement technique

The devices are probed in a quasi four-terminal configuration by sourcing a sawtooth current and monitoring the voltage drop over the SQUID. We use the counter technique, outlined in Fig. 7.5, to measure I_c and map the switching statistics of the device [54].

7

The sawtooth current I is created by applying an sawtooth-shaped voltage V_bias with frequency f ($\sim$ 5 Hz – 2 kHz), amplitude V_pp and off-set voltage V_off from zero (upper panel) to a resistor R_bias ($\sim 10\,\mathrm{k}\Omega$) in series with the device. The voltage drop over the SQUID V_SQUID (lower panel) is measured and forwarded to a counter. For $I < I_\mathrm{c}$, the device resides in a dissipationless state and V_SQUID equals zero. Once $I = I_\mathrm{c}$ is exceeded, transition to the resistive state sets in sharply and a voltage is detected. I_c is calculated through

$$I_\mathrm{c} = \frac{1}{R_\mathrm{bias}}\left(V_\mathrm{off} + \frac{V_\mathrm{pp}f}{x}\left(t_\mathrm{meas} - \frac{1}{2f}\right)\right), \tag{7.4}$$

with the time t_meas, taken between 50% of the falling slope of V_bias and V_SQUID exceeding a defined trigger level V_trig, when the junction switches into the resistive state. x denotes the ratio of rising to falling slope per period $T = 1/f$ of the drive signal. The routine is repeated 200 times for every magnetic field value with all critical current values being recorded.

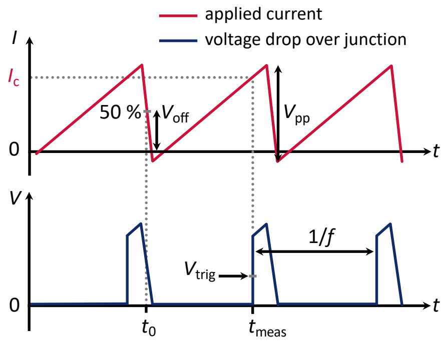

Figure 7.5. Counter measurement technique A sawtooth-shaped voltage V_{bias} is applied to a resistor R_{bias} in series with the device, effectively creating an alternating current I (upper panel). Simultaneously, the voltage V_{SQUID} (lower panel) over the device is measured and a non-zero value is detected when $I > I_{\mathrm{c}}$, the critical current of the SQUID. From the known input parameters of the ac-current it is possible to calculate the switching current.

7.5. CPR measurement

7.5.1. Large magnetic field range

Figure 7.6 a) presents the switching behavior of the SQUID device in a large magnetic field range at base temperature $T = 30\,\mathrm{mK}$ of the cryostat. Visible are multiple aperiodically oscillating branches with linear slope on a curved background which peaks around $B \sim -3.5\,\mathrm{mT}$ due to an offset in magnetic field arising from the measurement setup. With increased field resolution in Fig. 7.6 b), fast SQUID oscillations appear that are superimposed on top of the slow, large-scale branches. We attribute the large scale behavior to the reference junction, which by itself acts as a SQUID due to the edge transport and non-uniform PdTe_x diffusion [175]. These transport characteristics are particularly pronounced in short JJs, as was shown in the previous Sec. 7.2. The observed multivalued switching behavior is common for inductance dominated SQUIDs [202–206].

In highest field resolution, shown in Fig. 7.6 c), highly periodic oscillations are detected that are preserved throughout the field range over hundreds of periods. Moving from left to right in the figure, we can see how a second set of SQUID oscillations becomes more prominent in the background. The data visualizes how the occupation of branches of the reference junction changes in larger field range. We note however, that the observed periodicity and

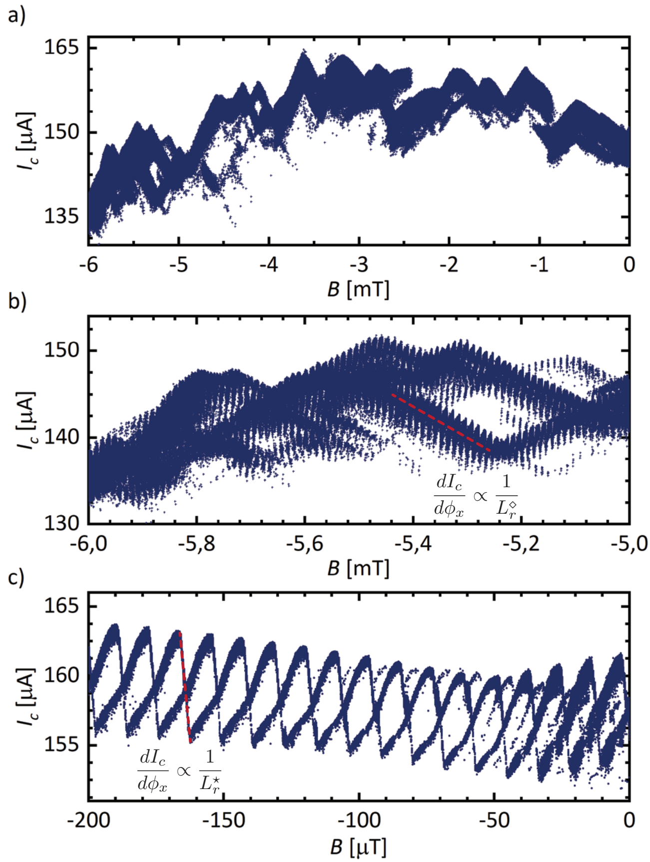

Figure 7.6. Switching statistics of the WTe_2 SQUID loop in magnetic field. Switching behavior of the SQUID with increasing magnetic resolution from top to bottom. a) On a large scale, multivalued switching of the device is observed, oscillating aperiodically in magnetic field. The characteristics are attributed to the short reference junction. b) Increasing the resolution in magnetic field reveals that the individual branches are broadened by fast SQUID oscillations. A single reference junction branch is highlighted by a red dashed line for illustration. The slope of the branch is proportional to $1/L_\mathrm{r}^\diamond$. c) High resolution measurement of the periodic SQUID oscillations in a field region with only a single reference junction branch. The falling side of the oscillation is highlighted by a red dashed line and the slope is proportional to $1/L_\mathrm{r}^\star$. Depending on the value of the magnetic field, additional reference junction branches, on which the SQUID oscillations sit on top, may intensify or fade out, as can be seen on the right end of the data.

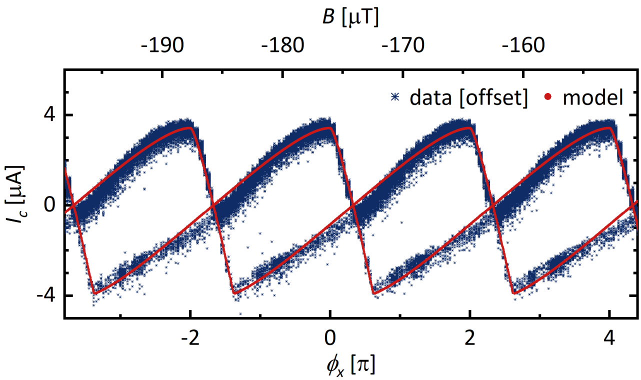

Figure 7.7. SQUID oscillations and model of the critical current as a function of applied flux. a) Experimental data of the SQUID oscillations versus external flux ϕ_x shown in blue. The red data points are a fit to the data based on maximizing the critical current in the SQUID loop. Phase winding in the superconducting loop is responsible for the multivalued supercurrent.

characteristics of the SQUID oscillations remain the same, independent of their hosting reference junction branch. In the following, we focus in detail on the oscillating SQUID behavior.

7.5.2. High resolution SQUID oscillations

Figure 7.7 presents the flux dependence of the critical SQUID current I_c in a magnetic field range where only a single branch of the reference junction is visible. The offset current of the reference junction $I_c^r = 160\,\mu A$ has been subtracted. Visible are oscillations with an extracted magnetic field periodicity $\delta B = 11.6\,\mu T$ that matches well the expected value of $\delta B = \Phi_0 / A_\circ = 11.1\,\mu T$. This observation proves that our contacts between a conventional superconductor and the self-formed $PdTe_x$ create an interface that supports coherent transport, rather than merely a low resistance contact.

From the ratio of the full critical current modulation $\delta I_c \sim 7\,\mu A$ to the average critical current value $\sim 160\,\mu A$, we expect the SQUID to be highly asymmetric and the measured signal to reflect the CPR of the weak Josephson junction. In contrast to a standard CPR measurement, the critical current has a pronounced multivalued pattern consisting of two intertwined branches that form a diamond-shaped structure. The rising sides of the oscillations increase gradually with a non-linear shape, compared to the almost linear dependence of the steep, falling sides.

The multivalued critical current in external flux ϕ_x further confirms the strong contribution of screening effects. The additional inductances L_r and L_w in the SQUID obstruct the direct relation between ϕ_tot and ϕ_x, as described by Eq. 7.3. Deducing the CPR from the inductive SQUID measurement therefore requires the knowledge of the phase dependences of $I_\mathrm{r}(\phi_\mathrm{tot})$ and $I_\mathrm{w}(\phi_\mathrm{tot})$ themselves. In order to bypass this constraint, we make an assumption about the CPRs of the JJs that is based on the experimental data. We use this information in the next step to calculate $\varphi_\mathrm{r}^\mathrm{max}(\phi_\mathrm{tot})$ that maximizes $I_\mathrm{c}(\phi_\mathrm{tot})$ according to Eq.7.2. Last, we include screening effects in the model and obtain the relation $I_\mathrm{c}(\phi_\mathrm{x})$, which we place in context to the experimental data.

Our choice of CPR for the weak junction is based on two experimental observations. First, the rising slope of $I_\mathrm{c}(\phi_\mathrm{x})$ is non-linear, suggesting the same should hold for the CPR. Second, the $I_\mathrm{c}(\phi_\mathrm{x})$ has self-crossings, implying that the phase of the reference junction does not remain fixed, contrary to the expectation from a of a highly asymmetric SQUID. The behavior is possible if the CPR of the weak junction contains abrupt changes, such as it is the case in the ballistic limit of the CPR. We outline the argument for the case in the next Sec. 7.5.3. $I_\mathrm{w}(\varphi_\mathrm{w})$ is modelled to be in the 2π-periodic, ballistic short junction limit [37]

$$I_\mathrm{w}(\varphi_\mathrm{w}) = I_\mathrm{c}^\mathrm{w}\frac{\sin(\varphi_\mathrm{w})}{\sqrt{1-\sin^2(\varphi_\mathrm{w}/2)}}, \tag{7.5}$$

scaled by the amplitude of I_c^w. The exact CPR of the reference junction plays little role in the further discussion, yet since it is formed in the same material, but with reduced length, we also model it as a short ballistic junction, scaled by I_c^r. Independently, we have used length dependent measurements in Sec. 7.2 and the analysis of the $PdTe_x$ diffusion profile in Ref. [175], to verify that both junctions behave indeed as JJs and are not shorted by $PdTe_x$ [207].

The top panel in Fig. 7.8 illustrates a visual method to maximize the critical current as a function of ϕ_tot. The individual currents through the SQUID arms I_r and I_w follow Eq. 7.5. The currents evolve in opposite flux direction, due to the connection $\varphi_\mathrm{r} - \varphi_\mathrm{w} = \phi_\mathrm{tot}$. We start at the configuration $\varphi_\mathrm{r} = \varphi_\mathrm{r}^\mathrm{max}$ and $\varphi_\mathrm{w} = \varphi_\mathrm{w}^\mathrm{max}$, when the currents through the reference and weak junctions I_c^r and I_c^w, respectively, are at their maximum. Moving from this point in negative direction of ϕ_tot, I_c follows I_w, plotted as red curve. In the opposite direction towards positive values of ϕ_tot, I_w faces a sharp drop, such that a higher I_c is obtained by following I_r, drawn in dark blue, until the intersection with I_w. This creates a small flux range $\delta\phi_\mathrm{tot} \propto \pi I_\mathrm{c}^\mathrm{w}/I_\mathrm{c}^\mathrm{r} \ll \pi$, in which I_c is maximized by following I_r rather than I_w, resulting in a changing φ_r, while $\varphi_\mathrm{w}^\mathrm{max} = \pi$ remains fixed. The situation is illustrated in the lower panel of Fig. 7.8. Once the two current branches cross with evolving flux, φ_r returns to its maximum value $\varphi_\mathrm{r}^\mathrm{max} = \pi$ and $I_\mathrm{c}(\phi_\mathrm{tot})$ follows the flux dependence of I_w. The well known behavior of the asymmetric SQUID is restored.

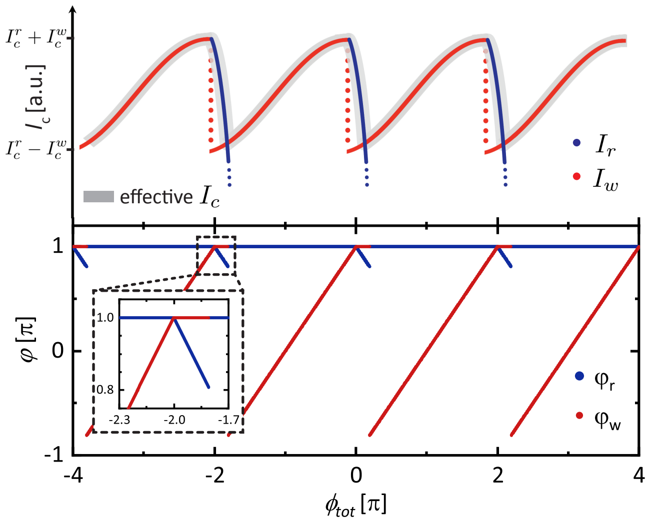

Figure 7.8. SQUID oscillations and model of the critical current as a function of applied flux. Visual method to maximize I_c as a function of total flux ϕ_tot. The upper panel plots the currents I_r and I_w for a short ballistic CPR with an amplitude ratio $I_\mathrm{c}^\mathrm{r}/I_\mathrm{c}^\mathrm{w} = 40$. The two currents evolve in opposite direction with increasing ϕ_tot, due to $\varphi_\mathrm{r} - \varphi_\mathrm{w} = \phi_\mathrm{tot}$. The resulting maximized I_c is highlighted by a gray background and is composed of the weak junction and the reference junction CPR for the rising and falling side, respectively. The lower panel shows the corresponding behavior of the junction phases φ_r and φ_w, obtained through the numerical maximization model described in Sec. 7.5.4. The phases are mapped to the range of the CPR. The switch between the observed weak and reference junction branch in the top panel is accompanied by a shift from a fixed φ_r to φ_w at flux values $\mathrm{mod}[\phi_\mathrm{tot}, 2\pi] = 0$.

While $\delta\phi_\mathrm{tot}$ remains small in the above scenario, it can extend significantly in the experiment, due to the inductance effects, as described by Eq. 7.3.

7.5.3. Instability of the reference junction phase φ_r

We argue in the following section that current crossings in a multivalued $I_\mathrm{c}(\phi_\mathrm{x})$ directly imply that the reference junction phase φ_r in an asymmetric SQUID can not remain fixed at its maximum value.

Let us assume that the initial situation is as observed in Fig. 7.7, such that $I_c(\phi_x)$ has self-crossings. Each crossing would be connected to two values in total flux, called $\phi_{tot,1}$ and $\phi_{tot,2}$, respectively. If φ_r remained fixed and only φ_w evolved, the device would be analogue to an ac-SQUID, containing only a single JJ. The current I circulating in such a device is described by $I = I_c f(\phi_{tot})$, with I_c being the critical current of the JJ and f being its CPR. The total flux in the ac-SQUID with inductance L is given by $\phi_{tot} = \phi_x + 2\pi I(\phi_{tot})L/\Phi_0$. Since I and ϕ_x are identical at the crossing point, the two equations directly imply that $\phi_{tot,1} = \phi_{tot,2}$. For this reason it is not possible to obtain self-crossings in $I_c(\phi_x)$ if only one junction phase evolves.

7.5.4. Numerical fit model

Having established that φ_r does not automatically remain fixed in an asymmetric SQUID, we introduce next a numerical procedure to transfer the above model from the dependence of total flux ϕ_{tot} to the external flux ϕ_x, the quantity applied in the experiment. The slope of $I_c(\phi_x)$ is directly related to the inductance of the current carrying arm in the SQUID, via $dI_c/d\phi_x = \Phi_0/(2\pi(L_i + L_J^i))$, with $i = w, r$, for the ascending and descending slopes of $I_c(\phi_x)$, respectively. In the model we assume a SQUID as shown in Fig. 7.4 c). Inductances additional to the Josephson inductances $L_J^{r,w}$ in the loop are accounted for by a cumulative series inductance in each SQUID branch, L_w and L_r, respectively, resulting in the total flux described by Eq. 7.3. Here, I_r and I_w correspond to the currents through the respective SQUID arms, i.e. $I_r = I_c^r f(\varphi_r)$ and $I_w = I_c^w f(\varphi_r + \phi_{tot})$. The two amplitudes I_c^r and I_c^w are determined from the fixed current background and the oscillation amplitude of the intertwined branches.

First, we evaluate numerically $\varphi_r(\phi_{tot})$, such that the current $I_c(\phi_{tot}) = I_r(\varphi_r(\phi_{tot})) + I_w(\varphi_r(\phi_{tot}) + \phi_{tot})$ is maximized. The lower panel in Fig. 7.8 plots the obtained φ_r and φ_w in blue and red, respectively, mapped to the range of the CPR. Based on the choice of the CPR function in Eq. 7.5, φ_r is mostly fixed at the maximum value $\varphi_r^{max} = \pi$, while φ_w evolves linearly in ϕ_{tot}, according to $\varphi_w = \phi_{tot} + \varphi_r$. However, a small range $\delta\phi_{tot}$ exists where φ_r changes in flux while φ_w remains fixed, in agreement with the above introduced graphical method in the upper panel of Fig. 7.8.

Given $\varphi_r(\phi_{tot})$, it is now possible to extract the inductance effects and recalculate the external flux $\phi_x = \phi_{tot} - 2\pi(L_r I_r - L_w I_w)/\Phi_0$. Depending on the magnitude of the incorporated inductances and critical currents, self-inductance effects in the loop cause the connection $\phi_{tot}(\phi_x)$ to become multi-valued, as it is visible from Fig. 7.9.

Finally, $I_c(\phi_x)$ is plotted in red in Fig. 7.7. Despite the long physical length $l_w = 1.5\,\mu m$ of the junction, we find the bending of the gradually rising slope $dI_c/d\phi_x$ to be well reproduced by f_w being in the 2π periodic ballistic short

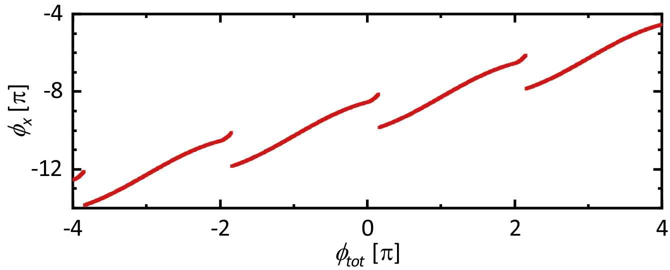

Figure 7.9. Multivalued $\phi_{\mathbf{tot}}$. Numerically calculated ϕ_{x} versus ϕ_{tot} using the model described Ch. 7.5.4. Inductance effects give rise to the multivalued $\phi_{\mathrm{x}}(\phi_{\mathrm{tot}})$, responsible for the intertwined branches visible in Fig. 7.7.

junction limit. We use the fixed current off-set of the data to determine $I_{\mathrm{c}}^{\mathrm{r}} = 160\,\mu\mathrm{A}$. $I_{\mathrm{c}}^{\mathrm{w}} = 3.75\,\mu\mathrm{A}$ is extracted from the amplitude of SQUID oscillations, based on the fact that we do not observe additional switching events below the presented data for any flux value. In both cases, the magnetic field dependencies of the current amplitudes are assumed to be negligible for the given field range. Importantly, despite the great asymmetry in critical currents of the embedded junctions, the model confirms that φ_{r} does not remain fixed in flux, such that the experimental data is composed out of the weak and the reference junction CPR. Even though the CPR of the weak junction is not necessarily uniquely in the short junction limit, it has to be close to ballistic in order to allow the shift between the fixed φ_{r} and φ_{w}.

Further, we extract the inductances $L_{\mathrm{r}} = 60\,\mathrm{pH}$ and $L_{\mathrm{w}} = 220\,\mathrm{pH}$, by matching the rising and falling slope of the fit to the data. An important result is, that L_{r} and L_{w} by themselves exceed the sum of geometrical inductance $L_{\mathrm{geo}} \approx 27.0\,\mathrm{pH}$ [208] and kinetic inductance $L_{\mathrm{kin}} \approx 5.5\,\mathrm{pH}$ [200] for the Nb SQUID loop. Possibly, additional JJs can form at the interface between the sputtered superconducting leads and the self-formed superconducting PdTe_x [192], yet given the fact that their critical current has to be larger than $I_{\mathrm{c}}^{\mathrm{r}}$, little inductance contribution is to be expected. Instead, we attribute the origin of additional inductance and its asymmetry between the SQUID arms to the superconducting PdTe_x that has self-formed at the interface between WTe_2 and Pd.

Consistently, the slope $dI_{\mathrm{c}}/d\phi_{\mathrm{x}}$, attributed to the phase change in the reference junction, yields the same inductance value for the SQUID oscillations ($L_{\mathrm{r}}^{\star}$) in Fig. 7.7 and the long range data ($L_{\mathrm{r}}^{\diamond}$) in Fig. 7.6 b), as illustrated by the red dashed lines in Figs. 7.6 b) and c). We find $L_{\mathrm{r}}^{\star} \sim 81\,\mathrm{pH}$ and $L_{\mathrm{r}}^{\diamond} \sim 166\,\mathrm{pH}$ $\sim 2L_{\mathrm{r}}^{\star}$. The factor of 2 arises when the reference junction is considered a

7

symmetric SQUID itself, due to the inhomogeneous $PdTe_x$ diffusion inside the junction [175]. In one case, the flux threads the area of the large Nb SQUID with an effective inductance $L_r^\diamond/2$, while in the other, it threads the reference junction area. In order to obtain the good agreement of $L_r^\diamond \sim 2L_r^\star$ we used the center-to-center distance between the Nb contacts in the reference junction. The measure can be explained by the sample design where the flux through half of the superconducting contact is screened into the junction [175, 193].

Finally, the multivalued I_c is explained in the framework of excited vorticity states in an inductive SQUID [202, 204–206, 209]. Using the parameters obtained from our fit, we calculate the magnetic screening factor $\beta_L = \pi I_c^w(L_w + L_r)/\Phi_0 > 1$ [22], reflecting that an additional flux quantum can be created by the maximum circulating current through the weak JJ. The result is a multivalued ϕ_{tot} as a function of ϕ_x, as was shown in Fig. 7.9 for given device parameters. The above behavior can differ strongly even on a single sample chip. While the second SQUID loop formed on the same WTe_2 flake (compare Fig. 7.4 a)) reveals the same behavior of the reference junction with multiple branches, we do not observe higher vorticity states in the SQUID oscillations. The absence of the feature is most likely connected to the overall smaller I_c^w, despite the shorter junction length with $l_w = 1.2\,\mu m$.

7.5.5. 2D SQUID potential

The formation of higher vorticity states in the SQUID can be visualised through the motion of a particle with mass in the two-dimensional SQUID potential, as described by Ref. [203]. This two-dimensional potential for an inductive DC SQUID can be understood as an analogue to the standard washboard potential of a single JJ [22].

The two-dimensional potential energy for a sinusoidal CPR is described by

$$U(\mathrm{x,y}) = U_0[-\frac{I}{2I_0}x - \cos(x)\cos(y) - \alpha\ \sin(x)\sin(y) - \eta\frac{I}{2I_0}y + \beta(y - \frac{1}{2}\phi_x)^2], \tag{7.6}$$

with $x = \varphi_r + \varphi_w$, $y = (\varphi_r - \varphi_w)/2$ and the inductance term $\beta = \Phi_0/(2\pi L I_0)$. Further, U_0 denotes the potential energy amplitude and $I = V_{bias}/R_{bias}$ corresponds to the biasing current. $\alpha = (a-1)/(a+1)$, with $a = I_c^r/I_c^w$, describes the asymmetry in critical currents $I_c^r = I_0(1+\alpha)$ and $I_c^w = I_0(1-\alpha)$, while the asymmetry in inductances η is defined as $L_r - L_w = \eta L$. For the sake of better visualization, we describe the model for the case of a symmetric SQUID with $\alpha = \eta = 0$. It should be noted that an asymmetry in critical current and in inductance creates an asymmetry in the potential, but does not change the general idea of the interpretation.

In case of a negligible inductance in the circuit, the two identical junctions are coupled and act as one. The potential has a well defined, 2π periodic

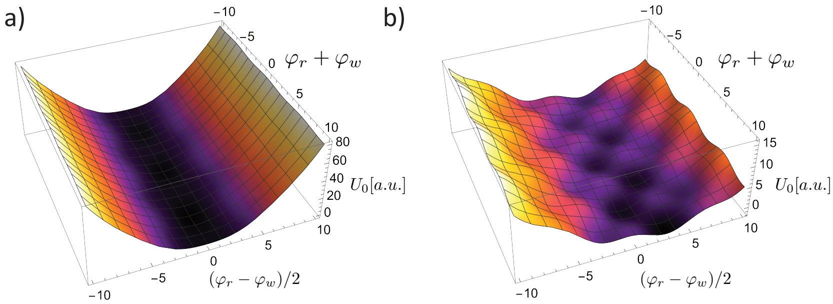

Figure 7.10. 2D potential of the SQUID. Two dimensional potential energy model used to describe the phase dynamics of a symmetric SQUID through the motion of a particle with mass. a) In case of a low inductance $\beta = 0.8$, a global minimum exists that results in a single valued critical current. Used parameters for the plot: $U_0 = 1$, $\phi_\mathrm{x} = 0$, $I/2I_0 = 0.1$, $\beta = 0.8$, $\alpha = \eta = 0$. b) With increasing inductance in the system, local minima appear that give rise to a multivalued critical current. An applied magnetic field can additionally shift the potential energy minimum away from $(\varphi_\mathrm{r} - \varphi_\mathrm{w})/2 = 0$. Used parameters for the plot: $U_0 = 1$, $\phi_\mathrm{x} = 2$, $I/2I_0 = 0.1$, $\beta = 0.1$, $\alpha = \eta = 0$.

global minimum along the $(\varphi_\mathrm{r} + \varphi_\mathrm{w})$ axis, as shown in Fig. 7.10. The motion of the phase particle is analogue to the situation described in the RCSJ model of a single junction [22]. Initially, the phase particle is trapped in the global minimum, corresponding to the zero voltage state of the SQUID. With increasing applied current I, the potential tilts along the $(\varphi_\mathrm{r}+\varphi_\mathrm{w})$ axis. When $I = I_\mathrm{c}$, the particle can escape from the potential well it was trapped in, and move along the slope. An inductance added to the systems decouples the two junctions. As a result, the potential landscape flattens and additional local minima appear in the direction of the axis $(\varphi_\mathrm{r} - \varphi_\mathrm{w})/2$, as plotted in Fig. 7.10 b). These additional minima are distinguished by the circulating current in the SQUID and decrease in depth as the circulating current increases. Each minimum in the direction of $(\varphi_\mathrm{r} - \varphi_\mathrm{w})/2$ can be associated to a number of flux quanta trapped in the SQUID loop. Starting from the zero voltage state of the SQUID, the phase particle can be trapped in any of the stable local minima. As I increases and the potential tilts, the critical current to set the particle free, depends now on the depth of the initial minimum and gives rise to the multivalued I_c states observed in the experiment. Additionally, Fig. 7.10 shows that an applied external flux creates an asymmetry along the axis $(\varphi_\mathrm{r}-\varphi_\mathrm{w})/2$ and therefore changes the escape route for the particle out of the potential wells. The asymmetric potential landscape as a function of ap-

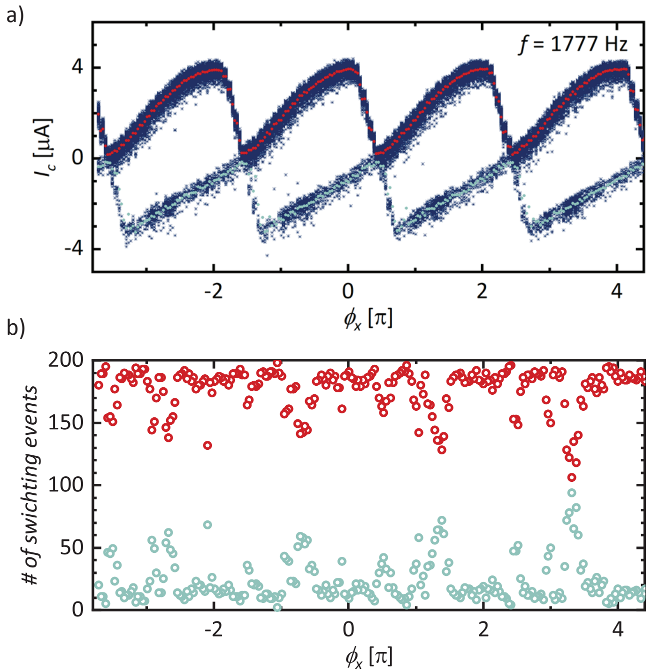

Figure 7.11. Occupation of the zeroth and higher vorticity states at applied ac frequency $f = 1777\,\mathrm{Hz}$. a) SQUID oscillations with color-coded average value for the zeroth and higher vorticity state above and below the current crossing point. b) Number of switching events for the two intertwined branches. Each magnetic field step contains 200 switching events, of which $\sim 13\%$ are occupying the higher vorticity state below the crossing point of I_c values.

plied flux explains the dependence of $I_c(\phi_x)$. The precise potential landscape depends on the specific parameters of the SQUID.

In the following discussion we introduce the nomenclature of a ground state and higher vorticity state of the SQUID to describe the data. These terms denote the I_c values above and below the crossing point of the multivalued $I_c(\phi_x)$ measurement and relate to the circulating current in the system. The previously introduced picture of higher vorticity states in the SQUID is also reflected in the occupation of these states. Figure 7.11 a) plots the average values of the switching distributions for the ground state and the higher vorticity state in red and turquoise, respectively. The frequency of the applied

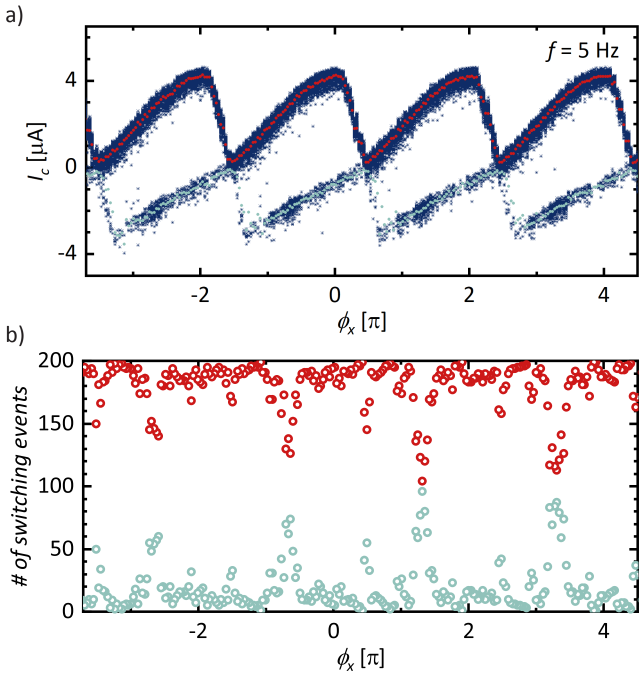

Figure 7.12. Occupation of the zeroth and higher vorticity SQUID states at applied ac frequency $f = 5\,\mathrm{Hz}$. a) SQUID oscillations with color-coded average value for the zeroth and higher-order state above and below the current crossing point. b) Number of switching events for the two intertwined branches. Each magnetic field step contains 200 switching events, of which $\sim 11\%$ are occupying the higher vorticity state below the crossing point of I_c values.

ac-current is $f = 1777\,\mathrm{Hz}$. Following the same color code, Fig. 7.11 b) traces the number of switching events in each of the states. At each magnetic field value, the critical current is measured 200 times in total and the switching events are distributed amongst the two visible states. The mean values of the ground state and higher vorticity state are ~ 177.3 and ~ 22.7 switching events per magnetic field step, relating to a ratio $r \sim 0.128$. We observe the higher vorticity SQUID state down to the lowest applied ac frequency $f = 5\,\mathrm{Hz}$ in Fig. 7.12 a). In this case, the mean value of the higher-order state is reduced to ~ 19.4 switching events per magnetic field value, resulting in $r \sim 0.107$.

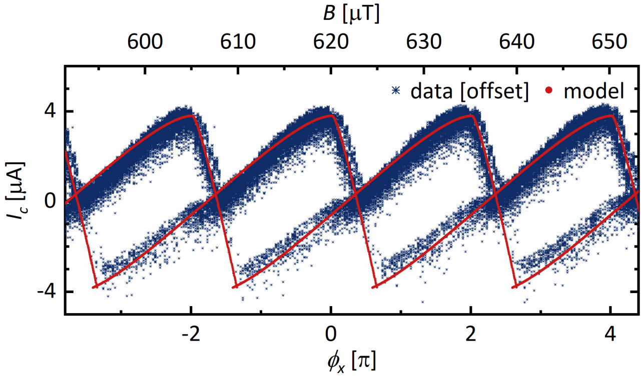

Figure 7.13. $I_c(\phi_x)$ at higher magnetic field values. The offset $I_c^r = 160\,\mu\text{A}$ has been subtracted. The fit parameters are $L_r = 60\,\text{pH}$, $L_w = 220\,\text{pH}$, $I_c^w = 3.9\,\mu\text{A}$ and a short ballistic CPR.

In summary, the introduced model visualizes the metastable states in the two dimensional SQUID potential which arise through the inductance in the loop [203]. Thermal fluctuations reduce the occupation of higher vorticity states and drive the system eventually back into its ground state. In general, Josephson junctions have widely been used in literature to study such transition processes [203, 210, 211]. Such an analysis for the here presented system lies however out of the scope of the current work.

7

7.5.6. Higher magnetic fields

Figure 7.13 plots the dependence $I_c(\phi_x)$ at higher magnetic fields. The offset current of the reference junciton $I_c^r = 160\,\mu\text{A}$ has been subtracted. While the general characteristics of the oscillations remain the same as presented before, the non-linearity in the rising slope is reduced compared to the data presented in Fig. 7.7. The data is fitted by the procedure described above, using the same parameters $L_r = 60\,\text{pH}$, $L_w = 220\,\text{pH}$, $I_c^r = 160\,\mu\text{A}$ and a short ballistic CPR for both junctions. However, the data is best fitted by increasing I_c^w from $3.75\,\mu\text{A}$ to $3.9\,\mu\text{A}$.

The behavior can be explained when the dependence of $I_c^w(B)$ is taken into account. The critical current amplitude of the weak junction, and also of the reference junction, oscillates in magnetic field as the magnetic flux threads the effective junction areas. The effect is well visible in the data of the second SQUID in Fig. 7.19 a). As $I_c^w(B)$ changes with magnetic flux, so does the ratio of L_J/L_K in Eq. 7.1.

The higher I_c^w in the given magnetic field range decreases the ratio and makes the inductance effects more dominant. As a result, the rising slope of the oscillations appears more linear.

7.5.7. Temperature dependence

We continue to study the SQUID oscillations at different temperatures of the measurement system. Figure 7.14 plots the dependence of $I_c(\phi_x)$ at the temperatures $T = 320\,\mathrm{mK}$, $580\,\mathrm{mK}$ and $900\,\mathrm{mK}$ in a), b) and c), respectively. I_c^r and I_c^w decrease with increasing temperature. Additionally, the overall appearance of the oscillations becomes more linear.

We evaluate the slope on the falling side of the oscillations and plot the extracted L_r as a function of temperature in Fig. 7.15. Visible is a monotonous increase of the inductance with increasing temperature. The dependence $L_r(T)$ is well described by [200]

$$L_K = A \frac{h}{2\pi^2 \Delta} \frac{1}{\tanh\left(\frac{\Delta}{2k_B T}\right)}, \tag{7.7}$$

with A being a proportionality constant and h the Planck constant. The temperature dependence of the superconducting gap is approximated as $\Delta(T) \approx \Delta(0)1.74(1 - T/T_c)^{0.5}$ [22], with $\Delta(0) = 1.76 k_B T_c$ being the superconducting gap at zero temperature. A fit to the data yields $T_c = 1.12\,\mathrm{K}$, which is in good agreement with the previous evaluation in Ch. 4.2 and reinforces the used analysis.

In order to evaluate the change in non-linearity of the rising slope with temperature we have to consider the temperature dependence of the product $L_K I_c$ in Eq. 7.1. As we calculate in App. 7.A.1, the product $L_K I_c$ decreases monotonously with increasing temperature in the investigated range, implying that the ratio of $L_K I_c$ should increase. Contrary to the expectation, we observe in the experimental data a transition towards linear slopes with increasing temperature, corresponding to a dominating L_K, equal to a reduced ratio L_J/L_K. A conclusive answer to this contradiction remains subject to future experiments.

7.5.8. Topological signatures

Until now, we have interpreted the data through a 2π periodic JJ in the short ballistic limit. In particular, the multivalued I_c appears due to additional inductances created by $PdTe_x$. It should be noted, that it is also possible to fit the observed 4π periodicity of a single SQUID oscillation branch with correct slopes $dI/d\phi_x$ in the picture of topological superconductivity, as shown in Sec. 7.5.9. Due to the fermion-parity anomaly [47], I_c of a topological

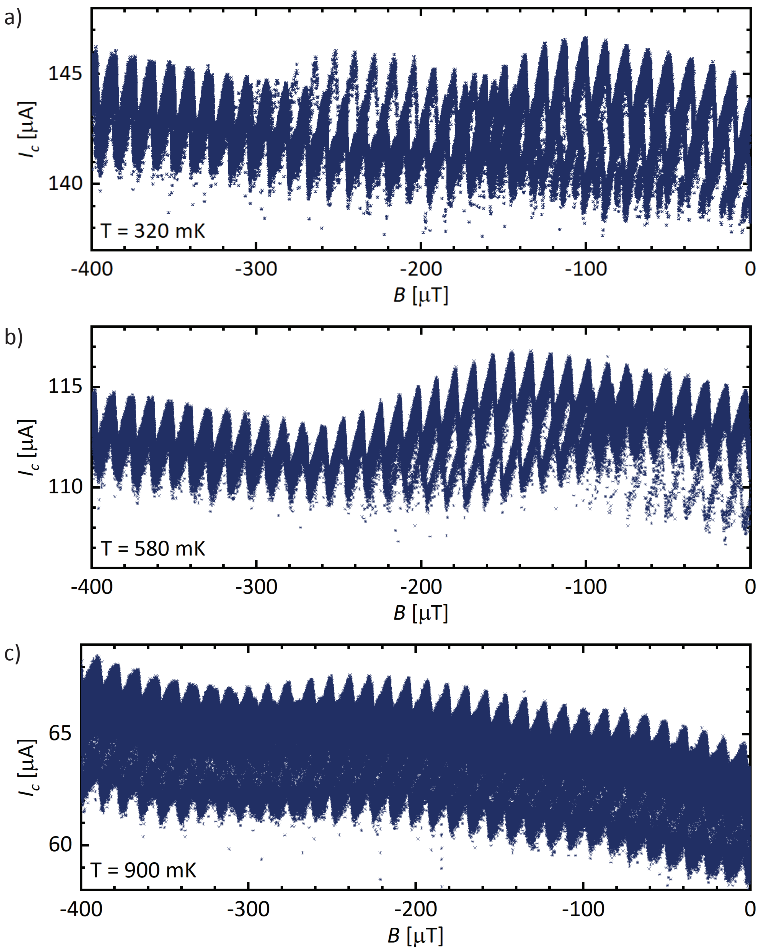

Figure 7.14. Temperature dependent measurements of the SQUID oscillations. $I_c(\phi_x)$ as a function of applied magnetic field for three different temperatures a) $T = 320\,\mathrm{mK}$, b) $T = 580\,\mathrm{mK}$ and c) $T = 900\,\mathrm{mK}$.

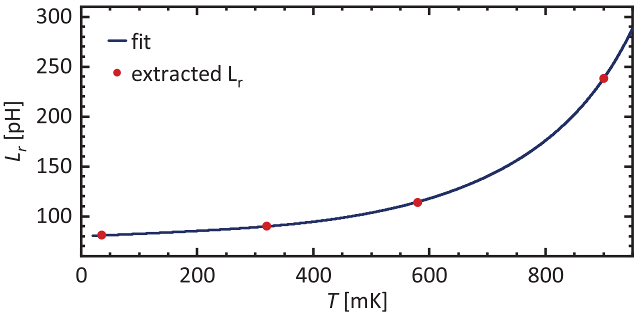

Figure 7.15. Temperature dependence of series inductance. L_{r} as a function of temperature. The inductance was extracted from the falling slope of the SQUID oscillations at various temperatures. The data is fitted by the temperature dependence of the kinetic inductance, yielding a critical temperature $T_{\mathrm{c}} \sim 1.12\,\mathrm{K}$ for PdTe_x.

JJ in the long junction limit displays a doubling in flux-periodicity to 4π and in amplitude to $I_{\mathrm{c},4\pi} = 2I_{\mathrm{c},2\pi}$, with $I_{\mathrm{c},2\pi}$ being the critical current in the topologically trivial case. When incorporated into our model, we find a symmetric inductance distribution $L_{\mathrm{w}} = L_{\mathrm{r}}$ to reproduce matching slopes $dI/d\phi_{\mathrm{x}}$ of the sawtooth-shaped branches. The multivalued current could be explained by two Majorana bound states (MBSs) with opposite parity, shifted by a phase of 2π relative to each other, due to quantum phase slips [212]. It has been shown in Ref. [212] that in case of a SQUID loop with both JJs being topologically non-trivial, the time scale for parity preservation of the MBSs can be dominated by quantum phase slips rather than quasi-particle poisoning [213–215]. We observe the intertwined character of the multivalued I_{c} in a wide frequency spectrum, down to as low as $f = 5\,\mathrm{Hz}$, resulting in a parity lifetime $> 200\,\mathrm{ms}$. A parity lifetime exceeding this time has been reported in Ref. [216].

Despite its possibility, the scenario does seem unlikely compared to our previous interpretation for several reasons. In the data, we observe a pronounced curvature $dI_{\mathrm{c}}/d\phi_{\mathrm{x}} \neq$ const. in the slope of the branches that is not reflected by the linear CPR of a ballistic JJ in the long junction limit. Moreover, a single channel in the topological ballistic long junction can carry a current $I_{\mathrm{c},4\pi} = E_{\mathrm{Th}}e/\hbar = v_{\mathrm{F}}e/l$ [47], with E_{Th} being the Thouless energy, v_{F} the Fermi velocity and l the length of the weak link. I_{c} in our junction would therefore have to be carried by at least $I_{\mathrm{c}}^{\mathrm{w}} l_{\mathrm{w}}/(ev_{\mathrm{F}}) \sim 116$ perfectly ballistic channels in parallel, assuming $v_{\mathrm{F}} = 3.09 \times 10^5\,\mathrm{m\,s^{-1}}$ [125]. It is expected for $\mathrm{WTe_2}$ to host a pair of hinge states on opposite edges of the crystal [101]. Additionally,

f_w / f_r	$\mathrm{Sin}(\varphi)$ / $\mathrm{Sin}(\varphi)$	$\mathrm{Sin}(\varphi)$ / Dayem	Linear 2π / Linear 2π	Long bal. 4π / Long bal. 4π
I_c^w [µA]	60	10	3.8	5
L_w [pH]	450	400	200	80
I_c^r [µA]	104	154	160	160
L_r [pH]	270	-	80	80

Table 7.1. Summary of device parameters used in the fits of Fig. 7.16. f_w and f_r denote to the normalized CPR function of the weak and reference junction used in the fit model. In case of the reference junction being modelled as Dayem bridge, all inductances are incorporated through the slope $1/L = dI/d\phi_x$ of the CPR. “Long bal. 4π” is the abbreviation for a 4π periodic topological JJ in the ballistic long junction limit.

conducting states have been found to reside at step edges in the crystal, where the number of vdW layers changes [111]. We do, however, not observe such crystal steps in optical microscopy for the used flake. It does therefore seem unlikely that the current is carried purely by ballistic hinge states.

7.5.9. Comparison of CPR configurations in the fitting procedure

In the section before, we fitted the experimental data under the assumption that both junctions in the SQUID are in the short ballistic limit. The assumption was based on the non-linearity of $I_c(\phi_x)$ in the rising slope and the fact that the phase φ_r of the reference junction does not remain fixed and therefore requires an abrupt jump in the CPR function.

In Fig. 7.16 we present additional fits to the data $I_c(\phi_x)$, based on different potential CPR functions of the two junctions. Details of the fits are summarized in Tab. 7.1.

Figure 7.16 a) addresses to both junctions a purely sinusoidal CPR function. In order to obtain the instability of the reference junction phase φ_r, the amplitude I_c^w of the weak junction has to be heavily increased compared to the observed data range. The amplitude of the reference junction is adjusted to $I_c^r = 164\,\mu\mathrm{A} - I_c^w$. The increased I_c^w gives rise to additional excited SQUID states that extend below the data. The series inductances of both SQUID arms, L_w and L_r are adjusted to match the slope of the fit with the data. In this case, it is not possible to determine a unique set of parameters to fit the data. Instead, higher excited current branches are potentially not observed in the data set, due to their very low switching probability.

Following a similar argument, Fig. 7.16 b) assumes a sinusoidal CPR for the weak junction, while the reference junction is treated as a Dayem bridge [217] made up of a continuous superconducting weak link. In this case, $PdTe_x$ would

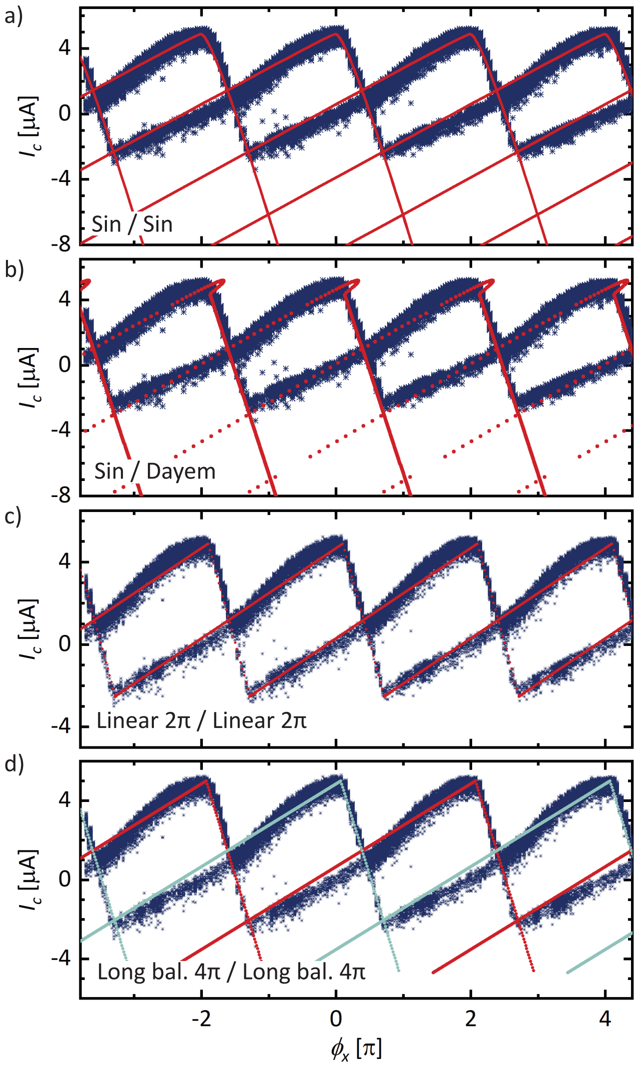

Figure 7.16. Comparison of fit models with different CPR functions. The weak junction and the reference junction, respectively, are assumed to have a) both a sinusoidal CPR, b) a sinusoidal CPR and the behavior of Dayem bridge and c) both a linear CPR of an inductor. d) Topological junction in the ballistic long junction limit with a 4π-periodic CPR. The red and green branch correspond to two parity states that are shifted by a phase of 2π relative to each through quantum phase slips.

have diffused through the entire WTe_2 crystal and created a superconducting short in the reference junction. Here, all inductance effects of L_r are included in the slope of the linear CPR, according to $1/L_\mathrm{r} = dI_\mathrm{c}/d\phi_\mathrm{x}$. This results in a periodicity that exceeds 2π. We obtain an overshoot of I_c around the maximum values that originates from the maximization process of I_c. Due to the shallow slope of the Dayem bridge, I_c continues to be maximized by following I_w, even beyond the maximum of I_w, before it switches to I_r.

A third option is plotted in Fig. 7.16 c), in which both junctions are modelled by a 2π periodic linear sawtooth CPR. In this case, both junctions are dominated by inductance effects, as was observed in the length dependence measurement in Fig. 7.2 a). Most notably, the fit does not reflect the curvature of the rising slope.

Last, Fig. 7.16 d) considers the weak and reference junction to be in the topological regime. Both junctions are modelled to be in the ballistic long junction limit with its characteristic sawtooth CPR. It should be noted that the effective fit does not change significantly, if the reference junction is considered to be in the ballistic short junction limit, as can be seen from the presented panels above. The red and green branches of the fit correspond to the Majorana bound states with opposite parity, shifted by a phase of 2π relative to each other. The extension of the fit below the experimental data originates from the included inductance $L_\mathrm{w} = L_\mathrm{r} = 80\,\mathrm{pH}$ in the SQUID arms.

In conclusion, none of the four alternative scenarios matches the experimental data in all its features. In particular, the curvature of the rising slope is best reproduced by the two junctions being in the short ballistic limit, as presented in the previous section. An uncertainty that remains in all fits is, if the observed data reflects the full range of switching events. Potentially, higher vorticity states at even lower I_c values could exist that are not observed in the experiment, due to their too small switching probability.

7.6. Conclusion

In conclusion, we have embedded two Josephson junctions, formed in WTe_2, into an asymmetric SQUID loop to measure the CPR of a WTe_2 JJ. Even though particular care was taken to minimize the inductance of the SQUID loop itself, we find a multivalued I_c that is explained by the inductive, self-formed $PdTe_x$. For this reason, it is crucial to not only consider the loop inductance by itself, but also the potential contribution from the interfaces between the embedded junctions and the SQUID loop. Additionally, the assumption of a fixed reference junction phase in flux does not hold in case of highly transparent junctions. Signatures of these effects could be falsely attributed to topological superconductivity, and therefore inductance effects have to be evaluated carefully.

We have further developed a fitting routine that reproduces the experimental data closely. The best fit was obtained by placing the weak junction in the short ballistic limit. Our results are related to recent studies on the higher-order TI bismuth [48, 218, 219] and establish WTe_2 as a promising platform for topological superconductivity.

7.A. Supplemental Material

The following section provides supporting information for the analysis presented in the previous main chapter.

7.A.1. Temperature dependence of the product $L_K I_c$

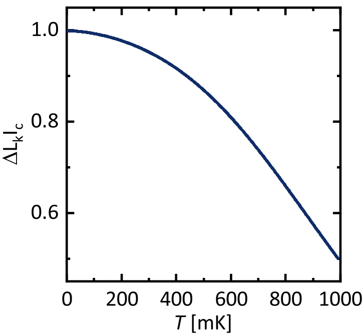

Figure 7.17. Relative change $\Delta L_\mathrm{K} I_\mathrm{c}$ of the product $L_\mathrm{K} I_\mathrm{c}$ as a function of temperature. $I_\mathrm{c}(T)$ is evaluated for a ballistic junction with transparency $\tau = 1$.

In the following section we evaluate the temperature dependence of the product $L_\mathrm{K} I_\mathrm{c}$. In case of a JJ with sinusoidal CPR and contact transparency τ, the temperature dependence of I_c can be described by [37]

$$I_\mathrm{c}(\varphi, T) = \frac{e\Delta}{\hbar} \left(\frac{\tau \sin(\varphi)}{\sqrt{1 - \tau \sin^2(\varphi/2)}} \right) \tanh \left(\frac{\Delta}{2k_\mathrm{B}T} \sqrt{1 - \tau \sin^2(\varphi/2)} \right). \quad (7.8)$$

We evaluate numerically $\varphi(T)$, for which $I_\mathrm{c}(\varphi, T)$ is maximized at a given temperature. Finally, using this value, we calculate the relative change $\Delta L_\mathrm{K} I_\mathrm{c}$ of the product $L_\mathrm{K} I_\mathrm{c}$ as a function of temperature for a ballistic junction with $\tau = 1$. Figure 7.17 shows, that $\Delta L_\mathrm{K} I_\mathrm{c}$ decreases monotonously with increasing temperature. We observe a similar behavior independent of the value of τ.

7.A.2. Measurement in between SQUIDs

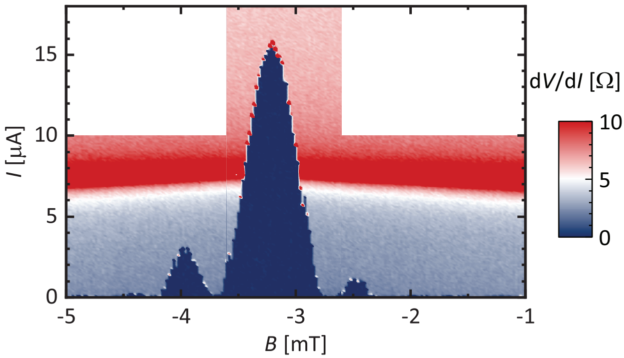

Figure 7.18. Josephson junction in between the SQUID devices. Differential resistance as a function of perpendicular magnetic field and applied bias current for Josephson junction in between the two SQUIDs presented in the main paper. The junction length is $l_{\mathrm{JJ}} = 1\,\mu\mathrm{m}$.

This section provides experimental support that the weak junction in the first SQUID with length $l_{\mathrm{w}} = 1.5\,\mu\mathrm{m}$ is not shorted by $PdTe_x$, but acts as a JJ. Figure 7.18 plots the differential resistance as a function of perpendicular magnetic field and bias current for the junction with length $l_{\mathrm{JJ}} = 1\,\mu\mathrm{m}$, located in between the two SQUID devices. The critical current as a function of magnetic field displays a "Fraunhofer" interference pattern, the hallmark signature of the Josephson effect.

7.A.3. 2nd SQUID

In the following section, we present $I_{\mathrm{c}}(B)$ measurements of the second SQUID on the chip. An optical image of the device is given in Fig. 7.4, located above the black dashed box. The width of the WTe_2 flake $w = 1.5\,\mu\mathrm{m}$ and the reference junction length $l_{\mathrm{r}} = 0.5\,\mu\mathrm{m}$ remain the same, while the weak junction length $l_{\mathrm{w}} = 1.2\,\mu\mathrm{m}$ is slightly shorter, compared to the SQUID presented in the main text.

Figure 7.19 a) plots I_{c} in a long range of applied magnetic field. Visible are multiple reference junction branches with a critical current value $I_{\mathrm{c}}^{\mathrm{r}} \sim 70\,\mu\mathrm{V}$. The fast SQUID oscillations can be seen on top of those reference junction branches. A high resolution measurement of the SQUID oscillations is plotted in Fig. 7.19 b). The oscillations appear single valued and slightly forward skewed towards increasing flux values, resembling at first glance a sinusoidal CPR. We use therefore the procedure described in the main text and fit the data by a purely sinusoidal CPR with an included series inductance $L_\mathrm{w} = 105\,\mathrm{pH}$, which reproduces the skewness well. This fit follows the standard behavior of an asymmetric SQUID, in the sense that the reference junction phase φ_r remains fixed and only φ_w evolves in flux. The skewness is purely created by the inductance effects in the superconducting loop and not due to the transparency of the junction. Similar fit results can, however, be obtained using the CPR of a junction with interface transparency $\tau > 0$.

A closer comparison between the data and the fit on the falling side of the oscillations reveals that the curvature of the data remains constantly negative, in contrast to the requirement for a CPR function to be an odd function (compare Ch. 2.1.4). The observation indicates that φ_r does not remain fixed in flux but evolves. For this reason we repeat the fitting procedure, assuming a ballistic short junction CPR for the weak and the reference junction in the SQUID. The result of the fitting procedure is presented in Fig. 7.19 c). Analogue to the discussion provided in the main text of the chapter, both junction phases φ_r and φ_w evolve in flux, such that the observed oscillations are now composed of the weak junction CPR for the rising side and the reference junction CPR for the falling side. This configuration maps the curvature of the falling slope correctly. A peculiarity remains unsolved at this point, because the fit is calculated with $L_\mathrm{w} = 0$, while the included $L_\mathrm{r} = 200\,\mathrm{pH}$ is comparable to the value found in the SQUID device of the main text. Potentially, this odd behavior could be connected to the fact, that I_c^w in this SQUID is smaller compared to that of the junction presented in the main text, despite its shorter junction length.

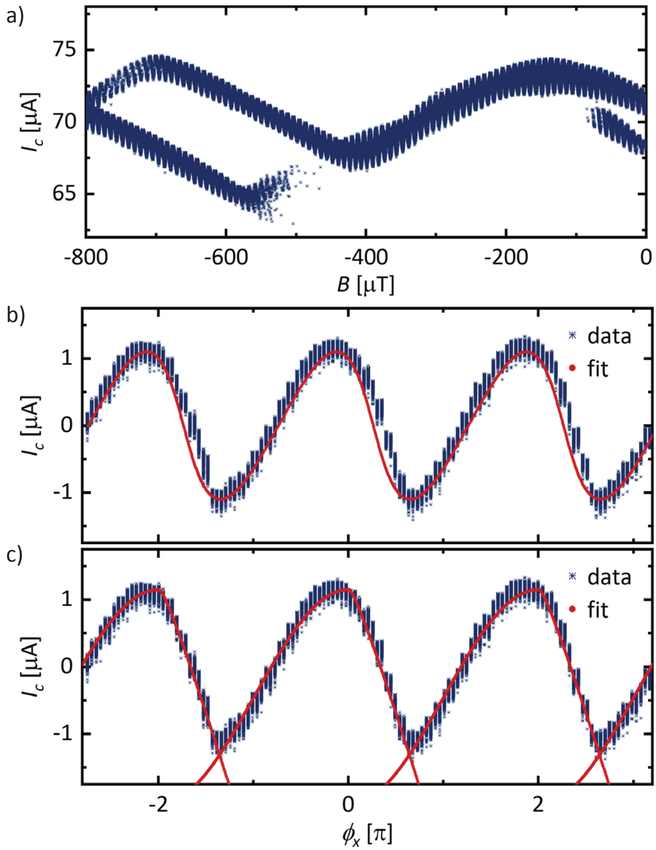

Figure 7.19. Critical current measurement of the second SQUID on the chip. a) I_c as a function of applied magnetic field in a long measurement range. Visible are two reference junction branches with fast SQUID oscillations superimposed on them. b) High-resolution measurement of the SQUID oscillations. The skewed SQUID oscillations are fit with a sinusoidal CPR in the inductive junction model, plotted in red. The reference junction phase φ_r remains fixed and does not evolve with flux. Fit parameters: $I_c^w = 1.1\,\mu A$, $L_w = 105\,pH$, CPR: $Sin(\varphi)$. c) Fit to the SQUID oscillations assuming a ballistic short junction CPR for both junctions. Fit parameters: $I_c^w = 1.6\,\mu A$, $L_w = 0$, $I_c^r = 77\,pH$, $L_r = 200\,pH$, CPR: short ballistic.

8 Conclusion and outlook

The fundamental objective of this thesis was to explore the TMDC WTe_2 as a potential platform for topological superconductivity. Our approach was to combine a topological insulator with a s-wave superconductor and study such hybrid structures in low-temperature transport measurements. The initial starting point for this work was the discovery that WTe_2 in contact with the normal metal Pd becomes superconducting [111], combining two fundamental properties en route to engineer topological superconductivity in a single, promising material system.

Summarizing, we studied in detail the phenomenon of emerging superconductivity in WTe_2 on Pd, by means of Josephson junctions and tunnelling probes. We briefly introduced the theoretical concepts of this thesis in Ch. 2 and the fabrication techniques for high quality samples in Ch. 3. In Ch. 4, we characterized the novel superconducting state in magnetic field and at elevated temperature. Interestingly, we found that the in-plane magnetic field exceeds the Pauli limit. Additionally, the transport measurements were complemented in Ch. 5 by tunnelling spectroscopy using a thin hBN flake as tunnel barrier. After the general characterization of superconductivity in this exciting system, we obtained a comprehensive understanding of its origin in Ch. 6. Through high resolution STEM and EDX analysis we found that Pd diffuses into the WTe_2 crystal and forms superconducting $PdTe_x$. Importantly, the formation of $PdTe_x$ was observed to be inhomogeneous over the width of the WTe_2 crystal, extending further along its edges compared to the bulk. Therefore, caution has to be exercised in diffusion driven junctions when superconducting edge currents are attributed to a topological origin. Furthermore, we demonstrated in this chapter a novel contacting method that benefits from the diffusion of $PdTe_x$ and creates highly transparent contacts to the topological material WTe_2. Finally, our goal was to investigate the transport regime of WTe_2/Pd Josephson junctions through the study of their current-phase relation. We used the newly developed contacting method and embedded Josephson junctions of WTe_2 on Pd in an asymmetric Nb SQUID. In Ch. 7, we presented that $PdTe_x$ gives rise to complex inductance contributions that reach beyond the standard picture of an asymmetric SQUID. We found a multivalued critical current that is composed of the interplay of the weak and reference junction current-phase relation. The data was best fitted by assuming the weak junction to be in the short ballistic limit.

The work presented in this thesis has developed a conclusive picture of the emerging superconductivity in WTe_2 on Pd and the implications $PdTe_x$ has for superconducting transport devices. We have highlighted the potential of Pd diffusion by developing highly transparent superconducting contacts to a topological insulator, an important step en route to engineered topological superconductivity in hybrid devices. At the same time, we have shown that the diffusion layer $PdTe_x$ could generate complex inductance effects, that potentially resemble topological signatures in transport measurements.

Future work with respect to $PdTe_x$ should pursue to determine the composition of the novel compound. Our results suggested, that neither of the two known superconductors PdTe nor $PdTe_2$ [188–191] formed through the diffusion of Pd into WTe_2. Promisingly, we discovered in transport measurements that the Pauli limit in parallel magnetic field is broken for $PdTe_x$. Additionally, we observed an unusual behavior of the gap-like feature in magnetic field in tunnelling spectroscopy on few-layer thin WTe_2 crystals on Pd. These two effects could point towards an unconventional pairing in this novel superconductor and therefore demand further investigation. Finally, control over the $PdTe_x$ diffusion itself would allow to reduce inductance effects in the Josephson junctions and facilitate the search for topological signatures.

Regarding WTe_2, more evidence for its topological character is required. Further insight into potential topological material properties could be gained through the measurement of Josephson radiation [220] and Shapiro steps in the ac Josephson effect [185, 221, 222].

Furthermore, our novel contacting method could be applied to similar topological tellurium-based materials such as $(Bi_{1-x}Sb_x)_2Te_3$ [184, 185]. The contacting method has the potential to reduce heating effects in Josephson junctions formed out of the material and integrate them into a superconducting chip architecture.

On a wider level, a topological qubit has not been achieved, yet. However, the search for topological superconductivity, the underlying building block for a topological qubit, is pursued in multiple material platforms with first promising results [91]. The work of this thesis expanded the insight into fundamental material and transport characteristics of WTe_2 and established it as a potential platform for topological superconductivity.

Bibliography

[1] P. W. Shor, in *Proceedings 35th annual symposium on foundations of computer science* (Ieee, 1994) pp. 124–134.

[2] R. P. Feynman, in *Feynman and Computation* (CRC Press, 2018) pp. 133–153.

[3] R. P. Feynman, Found. Phys. **16**, 507 (1986).

[4] I. M. Georgescu, S. Ashhab, and F. Nori, Reviews of Modern Physics **86**, 153 (2014).

[5] T. D. Ladd, F. Jelezko, R. Laflamme, Y. Nakamura, C. Monroe, and J. L. O'Brien, Nature **464**, 45 (2010).

[6] J. M. Gambetta, J. M. Chow, and M. Steffen, npj quantum information **3**, 1 (2017).

[7] P. W. Shor, Physical Review A **52**, R2493 (1995).

[8] C. Beenakker, Annual Review of Condensed Matter Physics **4**, 113 (2013).

[9] Y. Oreg, G. Refael, and F. Von Oppen, Physical Review Letters **105**, 177002 (2010).

[10] R. M. Lutchyn, J. D. Sau, and S. D. Sarma, Physical Review Letters **105**, 077001 (2010).

[11] J. D. Sau, R. M. Lutchyn, S. Tewari, and S. D. Sarma, Physical Review Letters **104**, 040502 (2010).

[12] L. Fu and C. L. Kane, Physical Review Letters **100**, 096407 (2008).

[13] L. Fu and C. L. Kane, Physical Review B **79**, 161408 (2009).

[14] Z. Wang, B. J. Wieder, J. Li, B. Yan, and B. A. Bernevig, Physical Review Letters **123**, 186401 (2019).

[15] L. Peng, Y. Yuan, G. Li, X. Yang, J.-J. Xian, C.-J. Yi, Y.-G. Shi, and Y.-S. Fu, Nature Communications **8**, 1 (2017).

[16] C. Huang, A. Narayan, E. Zhang, X. Xie, L. Ai, S. Liu, C. Yi, Y. Shi, S. Sanvito, and F. Xiu, National Science Review **7**, 1468 (2020).

[17] F. Schindler, A. M. Cook, M. G. Vergniory, Z. Wang, S. S. Parkin, B. A. Bernevig, and T. Neupert, Science Advances **4**, eaat0346 (2018).

[18] W. A. Benalcazar, B. A. Bernevig, and T. L. Hughes, Science **357**, 61 (2017).

[19] O. H. KAMERLINGH, Commun. Phys. Lab. Univ. Leiden, b **120** (1911).

[20] W. Meissner and R. Ochsenfeld, Naturwissenschaften **21**, 787 (1933).

[21] F. London and H. London, Proceedings of the Royal Society of London. Series A-Mathematical and Physical Sciences **149**, 71 (1935).

[22] M. Tinkham, *Introduction to Superconductivity*, 2nd ed. (Dover Publications, 2004).

[23] V. L. Ginzburg and L. D. Landau, in *On superconductivity and superfluidity* (Springer, 2009) pp. 113–137.

[24] A. A. Abrikosov, Soviet Physics-JETP **5**, 1174 (1957).

[25] J. Bardeen, L. N. Cooper, and J. R. Schrieffer, Physical Review **108**, 1175 (1957).

[26] J. Bardeen, L. N. Cooper, and J. R. Schrieffer, Physical Review **106**, 162 (1957).

[27] R. Gross, A. Marx, D. Einzel, and S. Geprägs, in *Festkörperphysik* (de Gruyter, 2018).

[28] B. Josephson, Advan. Phys **14**, 419 (1965).

[29] R. Haller, *Probing the microwave response of novel Josephson elements*, Ph.D. thesis, University of Basel (2021).

[30] T. Klapwijk, Journal of Superconductivity **17**, 593 (2004).

[31] G. Blonder, M. Tinkham, and T. Klapwijk, Physical Review B **25**, 4515 (1982).

[32] M. Octavio, M. Tinkham, G. Blonder, and T. Klapwijk, Physical Review B **27**, 6739 (1983).

[33] K. Flensberg, J. B. Hansen, and M. Octavio, Physical Review B **38**, 8707 (1988).

[34] J. Pillet, C. Quay, P. Morfin, C. Bena, A. L. Yeyati, and P. Joyez, Nature Physics **6**, 965 (2010).

[35] Y. V. Nazarov and Y. M. Blanter, *Quantum transport: introduction to nanoscience* (Cambridge university press, 2009).

[36] A. M. Zagoskin, *Quantum theory of many-body systems*, Vol. 2nd Edition (Springer, 2014).

[37] P. F. Bagwell, Physical Review B **46**, 12573 (1992).

[38] I. Kulik, Soviet Journal of Experimental and Theoretical Physics **30**, 944 (1969).

[39] E. Prada, P. San-Jose, M. W. de Moor, A. Geresdi, E. J. Lee, J. Klinovaja, D. Loss, J. Nygård, R. Aguado, and L. P. Kouwenhoven, Nature Reviews Physics **2**, 575 (2020).

[40] L. Bretheau, J. I.-J. Wang, R. Pisoni, K. Watanabe, T. Taniguchi, and P. Jarillo-Herrero, Nature Physics **13**, 756 (2017).

[41] P. Samuelsson, J. Lantz, V. Shumeiko, and G. Wendin, Physical Review B **62**, 1319 (2000).

[42] C. Beenakker, in *Transport Phenomena in Mesoscopic Systems* (Springer, 1992) pp. 235–253.

[43] Y. V. Nazarov and Y. M. Blanter, *Quantum transport: introduction to nanoscience* (Cambridge university press, 2009).

[44] C. Ishii, Progress of Theoretical Physics **44**, 1525 (1970).

[45] J. Bardeen and J. L. Johnson, Physical Review B **5**, 72 (1972).

[46] A. A. Golubov, M. Y. Kupriyanov, and E. Il'Ichev, Reviews of Modern Physics **76**, 411 (2004).

[47] C. W. J. Beenakker, D. I. Pikulin, T. Hyart, H. Schomerus, and J. P. Dahlhaus, Physical Review Letters **110**, 017003 (2013).

[48] A. Murani, A. Kasumov, S. Sengupta, Y. A. Kasumov, V. Volkov, I. Khodos, F. Brisset, R. Delagrange, A. Chepelianskii, R. Deblock, H. Bouchiat, and S. Guéron, Nature Communications **8**, 1 (2017).

[49] M. Kayyalha, A. Kazakov, I. Miotkowski, S. Khlebnikov, L. P. Rokhinson, and Y. P. Chen, npj quantum materials **5**, 1 (2020).

[50] I. Sochnikov, L. Maier, C. A. Watson, J. R. Kirtley, C. Gould, G. Tkachov, E. M. Hankiewicz, C. Brüne, H. Buhmann, L. W. Molenkamp, *et al.*, Physical Review Letters **114**, 066801 (2015).

[51] A. Y. Kitaev, Physics-Uspekhi **44**, 131 (2001).

[52] H.-J. Kwon, K. Sengupta, and V. M. Yakovenko, The European Physical Journal B-Condensed Matter and Complex Systems **37**, 349 (2004).

[53] K. Likharev, Reviews of Modern Physics **51**, 101 (1979).

[54] D. I. Indolese, P. Karnatak, A. Kononov, R. Delagrange, R. Haller, L. Wang, P. Makk, K. Watanabe, T. Taniguchi, and C. Schönenberger, Nano Letters **20**, 7129 (2020).

[55] X.-L. Qi and S.-C. Zhang, Reviews of Modern Physics **83**, 1057 (2011).

[56] M. Z. Hasan and C. L. Kane, Reviews of Modern Physics **82**, 3045 (2010).

[57] K. Von Klitzing, Reviews of Modern Physics **58**, 519 (1986).

[58] A. F. Rigosi and R. E. Elmquist, Semiconductor Science and Technology **34**, 093004 (2019).

[59] W. Poirier and F. Schopfer, The European Physical Journal Special Topics **172**, 207 (2009).

[60] M. Franz and L. Molenkamp, *Topological insulators* (Elsevier, 2013).

[61] Y. Ando and L. Fu, Annual Review of Condensed Matter Physics **6**, 361 (2015).

[62] O. Breunig and Y. Ando, Nature Reviews Physics **4**, 184 (2022).

[63] J. E. Avron, D. Osadchy, and R. Seiler, Physics Today **56**, 38 (2003).

[64] M. Nakahara, *Geometry, topology and physics* (CRC press, 2018).

[65] "Online course on topology in condensed matter," `https://topocondmat.org`, Accessed: 2022-09-02.

[66] D. J. Thouless, M. Kohmoto, M. P. Nightingale, and M. den Nijs, Physical Review Letters **49**, 405 (1982).

[67] C. L. Kane and E. J. Mele, Physical Review Letters **95**, 146802 (2005).

[68] B. A. Bernevig and S.-C. Zhang, Physical Review Letters **96**, 106802 (2006).

[69] M. Konig, S. Wiedmann, C. Brune, A. Roth, H. Buhmann, L. W. Molenkamp, X.-L. Qi, and S.-C. Zhang, Science **318**, 766 (2007).

[70] B. A. Bernevig, T. L. Hughes, and S.-C. Zhang, science **314**, 1757 (2006).

[71] C. Brüne, A. Roth, H. Buhmann, E. M. Hankiewicz, L. W. Molenkamp, J. Maciejko, X.-L. Qi, and S.-C. Zhang, Nature Physics **8**, 485 (2012).

[72] A. Roth, C. Brüne, H. Buhmann, L. W. Molenkamp, J. Maciejko, X.-L. Qi, and S.-C. Zhang, Science **325**, 294 (2009).

[73] M. Z. Hasan and J. E. Moore, Annual Review of Condensed Matter Physics **2**, 55 (2011).

[74] M. Büttiker, Physical Review B **38**, 9375 (1988).

[75] L. Fu, C. L. Kane, and E. J. Mele, Physical Review Letters **98**, 106803 (2007).

[76] D. Hsieh, D. Qian, L. Wray, Y. Xia, Y. S. Hor, R. J. Cava, and M. Z. Hasan, Nature **452**, 970 (2008).

[77] D. Hsieh, Y. Xia, D. Qian, L. Wray, F. Meier, J. Osterwalder, L. Patthey, J. G. Checkelsky, N. Ong, A. V. Fedorov, *et al.*, Nature **460**, 1101 (2009).

[78] D. Hsieh, Y. Xia, D. Qian, L. Wray, F. Meier, J. Dil, J. Osterwalder, L. Patthey, A. Fedorov, H. Lin, *et al.*, Physical Review Letters **103**, 146401 (2009).

[79] A. Taskin, S. Sasaki, K. Segawa, and Y. Ando, Physical Review Letters **109**, 066803 (2012).

[80] L. He, F. Xiu, X. Yu, M. Teague, W. Jiang, Y. Fan, X. Kou, M. Lang, Y. Wang, G. Huang, *et al.*, Nano Letters **12**, 1486 (2012).

[81] B. Yan and C. Felser, Annual Review of Condensed Matter Physics **8**, 337 (2017).

[82] S. Wang, B.-C. Lin, A.-Q. Wang, D.-P. Yu, and Z.-M. Liao, Advances in Physics: X **2**, 518 (2017).

[83] P. Hosur and X. Qi, Comptes Rendus Physique **14**, 857 (2013).

[84] S. Rao, arXiv preprint arXiv:1603.02821 (2016).

[85] S. Murakami, New Journal of Physics **9**, 356 (2007).

[86] S. Murakami, S. Iso, Y. Avishai, M. Onoda, and N. Nagaosa, Physical Review B **76**, 205304 (2007).

[87] A. P. Schnyder, S. Ryu, A. Furusaki, and A. W. Ludwig, Physical Review B **78**, 195125 (2008).

[88] A. Kitaev, in *AIP conference proceedings*, Vol. 1134 (American Institute of Physics, 2009) pp. 22–30.

[89] X.-L. Qi, T. L. Hughes, S. Raghu, and S.-C. Zhang, Physical Review Letters **102**, 187001 (2009).

[90] T. Hyart, B. van Heck, I. C. Fulga, M. Burrello, A. R. Akhmerov, and C. W. J. Beenakker, Physical Review B **88**, 035121 (2013).

[91] M. Sato and Y. Ando, Reports on Progress in Physics **80**, 076501 (2017).

[92] N. Read and D. Green, Physical Review B **61**, 10267 (2000).

[93] N. Lu, C. Zhang, C.-H. Lee, J. P. Oviedo, M. A. T. Nguyen, X. Peng, R. M. Wallace, T. E. Mallouk, J. A. Robinson, J. Wang, *et al.*, The Journal of Physical Chemistry C **120**, 8364 (2016).

[94] X. Qian, J. Liu, L. Fu, and J. Li, Science **346**, 1344 (2014).

[95] Y. Wang, E. Liu, H. Liu, Y. Pan, L. Zhang, J. Zeng, Y. Fu, M. Wang, K. Xu, Z. Huang, *et al.*, Nature Communications **7**, 1 (2016).

[96] W. Tian, W. Yu, X. Liu, Y. Wang, and J. Shi, Materials **11**, 1185 (2018).

[97] A. Mar, S. Jobic, and J. A. Ibers, Journal of the American Chemical Society **114**, 8963 (1992).

[98] W. Dawson and D. Bullett, Journal of Physics C: Solid State Physics **20**, 6159 (1987).

[99] M. N. Ali, J. Xiong, S. Flynn, J. Tao, Q. D. Gibson, L. M. Schoop, T. Liang, N. Haldolaarachchige, M. Hirschberger, N. P. Ong, and R. J. Cava, Nature **514**, 205 (2014).

[100] Y. Zhao, H. Liu, J. Yan, W. An, J. Liu, X. Zhang, H. Wang, Y. Liu, H. Jiang, Q. Li, *et al.*, Physical Review B **92**, 041104 (2015).

[101] Y.-B. Choi, Y. Xie, C.-Z. Chen, J. Park, S.-B. Song, J. Yoon, B. J. Kim, T. Taniguchi, K. Watanabe, J. Kim, *et al.*, Nature Materials **19**, 974 (2020).

[102] A. A. Soluyanov, D. Gresch, Z. Wang, Q. Wu, M. Troyer, X. Dai, and B. A. Bernevig, Nature **527**, 495 (2015).

[103] P. Li, Y. Wen, X. He, Q. Zhang, C. Xia, Z.-M. Yu, S. A. Yang, Z. Zhu, H. N. Alshareef, and X.-X. Zhang, Nature Communications **8**, 1 (2017).

[104] S. Wu, V. Fatemi, Q. D. Gibson, K. Watanabe, T. Taniguchi, R. J. Cava, and P. Jarillo-Herrero, Science **359**, 76 (2018).

[105] Z. Fei, T. Palomaki, S. Wu, W. Zhao, X. Cai, B. Sun, P. Nguyen, J. Finney, X. Xu, and D. H. Cobden, Nature Physics **13**, 677 (2017).

[106] W. Zhao, E. Runburg, Z. Fei, J. Mutch, P. Malinowski, B. Sun, X. Huang, D. Pesin, Y.-T. Cui, X. Xu, *et al.*, Physical Review X **11**, 041034 (2021).

[107] X. Qian, J. Liu, L. Fu, and J. Li, Science **346**, 1344 (2014).

[108] S. Tang, C. Zhang, D. Wong, Z. Pedramrazi, H.-Z. Tsai, C. Jia, B. Moritz, M. Claassen, H. Ryu, S. Kahn, *et al.*, Nature Physics **13**, 683 (2017).

[109] Z.-Y. Jia, Y.-H. Song, X.-B. Li, K. Ran, P. Lu, H.-J. Zheng, X.-Y. Zhu, Z.-Q. Shi, J. Sun, J. Wen, *et al.*, Physical Review B **96**, 041108 (2017).

[110] F. Zheng, C. Cai, S. Ge, X. Zhang, X. Liu, H. Lu, Y. Zhang, J. Qiu, T. Taniguchi, K. Watanabe, *et al.*, Advanced Materials **28**, 4845 (2016).

[111] A. Kononov, G. Abulizi, K. Qu, J. Yan, D. Mandrus, K. Watanabe, T. Taniguchi, and C. Schönenberger, Nano Letters **20**, 4228 (2020).

[112] R. Dynes and T. Fulton, Physical Review B **3**, 3015 (1971).

[113] D. Kang, Y. Zhou, W. Yi, C. Yang, J. Guo, Y. Shi, S. Zhang, Z. Wang, C. Zhang, S. Jiang, *et al.*, Nature Communications **6**, 1 (2015).

[114] X.-C. Pan, X. Chen, H. Liu, Y. Feng, Z. Wei, Y. Zhou, Z. Chi, L. Pi, F. Yen, F. Song, *et al.*, Nature Communications **6**, 1 (2015).

[115] T. Asaba, Y. Wang, G. Li, Z. Xiang, C. Tinsman, L. Chen, S. Zhou, S. Zhao, D. Laleyan, Y. Li, *et al.*, Scientific Reports **8**, 1 (2018).

[116] E. Sajadi, T. Palomaki, Z. Fei, W. Zhao, P. Bement, C. Olsen, S. Luescher, X. Xu, J. A. Folk, and D. H. Cobden, Science **362**, 922 (2018).

[117] V. Fatemi, S. Wu, Y. Cao, L. Bretheau, Q. D. Gibson, K. Watanabe, T. Taniguchi, R. J. Cava, and P. Jarillo-Herrero, Science **362**, 926 (2018).

[118] K. S. Novoselov, A. K. Geim, S. V. Morozov, D.-e. Jiang, Y. Zhang, S. V. Dubonos, I. V. Grigorieva, and A. A. Firsov, Science **306**, 666 (2004).

[119] A. K. Geim and I. V. Grigorieva, Nature **499**, 419 (2013).

[120] Y. Liu, N. O. Weiss, X. Duan, H.-C. Cheng, Y. Huang, and X. Duan, Nature Reviews Materials **1**, 1 (2016).

[121] K. Novoselov, o. A. Mishchenko, o. A. Carvalho, and A. Castro Neto, Science **353**, aac9439 (2016).

[122] S. Manzeli, D. Ovchinnikov, D. Pasquier, O. V. Yazyev, and A. Kis, Nature Reviews Materials **2**, 1 (2017).

[123] H. Liu, A. T. Neal, Z. Zhu, Z. Luo, X. Xu, D. Tománek, and P. D. Ye, ACS Nano **8**, 4033 (2014).

[124] K. F. Mak, C. Lee, J. Hone, J. Shan, and T. F. Heinz, Physical Review Letters **105**, 136805 (2010).

[125] P. Li, Y. Wen, X. He, Q. Zhang, C. Xia, Z.-M. Yu, S. A. Yang, Z. Zhu, H. N. Alshareef, and X.-X. Zhang, Nature Communications **8**, 1 (2017).

[126] Z. Fei, T. Palomaki, S. Wu, W. Zhao, X. Cai, B. Sun, P. Nguyen, J. Finney, X. Xu, and D. H. Cobden, Nature Physics **13**, 677 (2017).

[127] E. Y. Andrei, D. K. Efetov, P. Jarillo-Herrero, A. H. MacDonald, K. F. Mak, T. Senthil, E. Tutuc, A. Yazdani, and A. F. Young, Nature Reviews Materials **6**, 201 (2021).

[128] M. Yankowitz, S. Chen, H. Polshyn, Y. Zhang, K. Watanabe, T. Taniguchi, D. Graf, A. F. Young, and C. R. Dean, Science **363**, 1059 (2019).

[129] Y. Cao, V. Fatemi, S. Fang, K. Watanabe, T. Taniguchi, E. Kaxiras, and P. Jarillo-Herrero, Nature **556**, 43 (2018).

[130] A. L. Sharpe, E. J. Fox, A. W. Barnard, J. Finney, K. Watanabe, T. Taniguchi, M. Kastner, and D. Goldhaber-Gordon, Science **365**, 605 (2019).

[131] F. Ye, J. Lee, J. Hu, Z. Mao, J. Wei, and P. X.-L. Feng, Small **12**, 5802 (2016).

[132] F. Hou, D. Zhang, P. Sharma, S. Singh, T. Wu, and J. Seidel, ACS Applied Electronic Materials **2**, 2196 (2020).

[133] H. Liu, N. Han, and J. Zhao, Rsc Advances **5**, 17572 (2015).

[134] P. Blake, E. Hill, A. Castro Neto, K. Novoselov, D. Jiang, R. Yang, T. Booth, and A. Geim, Applied Physics Letters **91**, 063124 (2007).

[135] C. Handschin, *Quantum tranport in incapsulated graphene p-n junctions*, Ph.D. thesis, University of Basel (2017).

[136] T. Völkl, T. Rockinger, M. Drienovsky, K. Watanabe, T. Taniguchi, D. Weiss, and J. Eroms, Physical Review B **96**, 125405 (2017).

[137] L. Wang, I. Meric, P. Huang, Q. Gao, Y. Gao, H. Tran, T. Taniguchi, K. Watanabe, L. Campos, D. Muller, *et al.*, Science **342**, 614 (2013).

[138] G. R. Bhimanapati, Z. Lin, V. Meunier, Y. Jung, J. Cha, S. Das, D. Xiao, Y. Son, M. S. Strano, V. R. Cooper, *et al.*, ACS Nano **9**, 11509 (2015).

[139] P. L. Levesque, S. S. Sabri, C. M. Aguirre, J. Guillemette, M. Siaj, P. Desjardins, T. Szkopek, and R. Martel, Nano Letters **11**, 132 (2011).

[140] A. Politano, G. Chiarello, R. Samnakay, G. Liu, B. Gürbulak, S. Duman, A. Balandin, and D. Boukhvalov, Nanoscale **8**, 8474 (2016).

[141] P. Zomer, M. Guimarães, J. Brant, N. Tombros, and B. Van Wees, Applied Physics Letters **105**, 013101 (2014).

[142] D. Purdie, N. Pugno, T. Taniguchi, K. Watanabe, A. Ferrari, and A. Lombardo, Nature Communications **9**, 1 (2018).

[143] A. Kononov, M. Endres, G. Abulizi, K. Qu, J. Yan, D. G. Mandrus, K. Watanabe, T. Taniguchi, and C. Schönenberger, Journal of Applied Physics **129**, 113903 (2021).

[144] G. Y. Cho, J. H. Bardarson, Y.-M. Lu, and J. E. Moore, Physical Review B **86**, 214514 (2012).

[145] H. Wei, S.-P. Chao, and V. Aji, Physical Review B **89**, 014506 (2014).

[146] G. Bednik, A. Zyuzin, and A. Burkov, Physical Review B **92**, 035153 (2015).

[147] C. Chan and X.-J. Liu, Physical Review Letters **118**, 207002 (2017).

[148] P. Hosur, X. Dai, Z. Fang, and X.-L. Qi, Physical Review B **90**, 045130 (2014).

[149] M. N. Ali, L. Schoop, J. Xiong, S. Flynn, Q. Gibson, M. Hirschberger, N. P. Ong, and R. J. Cava, EPL (Europhysics Letters) **110**, 67002 (2015).

[150] F.-X. Xiang, A. Srinivasan, Z. Du, O. Klochan, S.-X. Dou, A. R. Hamilton, and X.-L. Wang, Physical Review B **98**, 035115 (2018).

[151] T. Ando, A. B. Fowler, and F. Stern, Reviews of Modern Physics **54**, 437 (1982).

[152] Y. Saito, T. Nojima, and Y. Iwasa, Nature Reviews Materials **2**, 1 (2016).

[153] Y. Liu, Y. Xu, J. Sun, C. Liu, Y. Liu, C. Wang, Z. Zhang, K. Gu, Y. Tang, C. Ding, *et al.*, Nano Letters **20**, 5728 (2020).

[154] Y. Liu, Z. Wang, X. Zhang, C. Liu, Y. Liu, Z. Zhou, J. Wang, Q. Wang, Y. Liu, C. Xi, *et al.*, Physical Review X **8**, 021002 (2018).

[155] R. A. Klemm, A. Luther, and M. Beasley, Physical Review B **12**, 877 (1975).

[156] A. Gubin, K. Il'in, S. Vitusevich, M. Siegel, and N. Klein, Physical Review B **72**, 064503 (2005).

[157] O. O. Shvetsov, A. Kononov, A. V. Timonina, N. N. Kolesnikov, and E. Deviatov, JETP Letters **107**, 774 (2018).

[158] A. Kononov, O. Shvetsov, S. Egorov, A. Timonina, N. Kolesnikov, and E. Deviatov, EPL (Europhysics Letters) **122**, 27004 (2018).

[159] V. Fatemi, Q. D. Gibson, K. Watanabe, T. Taniguchi, R. J. Cava, and P. Jarillo-Herrero, Physical Review B **95**, 041410 (2017).

[160] Z. Zhu, X. Lin, J. Liu, B. Fauqué, Q. Tao, C. Yang, Y. Shi, and K. Behnia, Physical Review Letters **114**, 176601 (2015).

[161] W. Yang, C.-J. Mo, S.-B. Fu, Y. Yang, F.-W. Zheng, X.-H. Wang, Y.-A. Liu, N. Hao, and P. Zhang, Physical Review Letters **125**, 237006 (2020).

[162] B. Sacépé, M. Feigel'man, and T. M. Klapwijk, Nature Physics **16**, 734 (2020).

[163] E. Khestanova, J. Birkbeck, M. Zhu, Y. Cao, G. Yu, D. Ghazaryan, J. Yin, H. Berger, L. Forro, T. Taniguchi, *et al.*, Nano Letters **18**, 2623 (2018).

[164] T. Dvir, F. Massee, L. Attias, M. Khodas, M. Aprili, C. H. Quay, and H. Steinberg, Nature Communications **9**, 1 (2018).

[165] A. Yazdani and A. Kapitulnik, Physical Review Letters **74**, 3037 (1995).

[166] J. Nicol, S. Shapiro, and P. H. Smith, Physical Review Letters **5**, 461 (1960).

[167] I. Giaever, Physical Review Letters **5**, 464 (1960).

[168] J. Bardeen, Physical Review Letters **6**, 57 (1961).

[169] T. T. Heikkilä, *The physics of nanoelectronics: transport and fluctuation phenomena at low temperatures*, Vol. 21 (Oxford University Press, 2013).

[170] R. Gross, A. Marx, D. Einzel, and S. Geprägs, in *Festkörperphysik* (de Gruyter, 2018).

[171] R. Dynes, V. Narayanamurti, and J. P. Garno, Physical Review Letters **41**, 1509 (1978).

[172] R. A. Klemm, M. Beasley, and A. Luther, Journal of Low Temperature Physics **16**, 607 (1974).

[173] D. Prober, M. Beasley, and R. Schwall, Physical Review B **15**, 5245 (1977).

[174] Y. Cao, J. M. Park, K. Watanabe, T. Taniguchi, and P. Jarillo-Herrero, Nature **595**, 526 (2021).

[175] M. Endres, A. Kononov, M. Stiefel, M. Wyss, H. S. Arachchige, J. Yan, D. Mandrus, K. Watanabe, T. Taniguchi, and C. Schönenberger, Physical Review Materials **6**, L081201 (2022).

[176] P. Schüffelgen, D. Rosenbach, C. Li, T. W. Schmitt, M. Schleenvoigt, A. R. Jalil, S. Schmitt, J. Kölzer, M. Wang, B. Bennemann, *et al.*, Nature Nanotechnology **14**, 825 (2019).

[177] C. R. Thomas, M. K. Vallon, M. G. Frith, H. Sezen, S. K. Kushwaha, R. J. Cava, J. Schwartz, and S. L. Bernasek, Chemistry of Materials **28**, 35 (2016).

[178] L. Aggarwal, A. Gaurav, G. S. Thakur, Z. Haque, A. K. Ganguli, and G. Sheet, Nature Materials **15**, 32 (2016).

[179] H. Wang, H. Wang, H. Liu, H. Lu, W. Yang, S. Jia, X.-J. Liu, X. Xie, J. Wei, and J. Wang, Nature Materials **15**, 38 (2016).

[180] O. Shvetsov, V. Esin, A. Timonina, N. Kolesnikov, and E. Deviatov, Physical Review B **99**, 125305 (2019).

[181] W. Zhu, X. Hou, J. Li, Y. Huang, S. Zhang, J. He, D. Chen, Y. Wang, Q. Dong, M. Zhang, *et al.*, Advanced Materials **32**, 1907970 (2020).

[182] Y. Xing, Z. Shao, J. Ge, J. Luo, J. Wang, Z. Zhu, J. Liu, Y. Wang, Z. Zhao, J. Yan, *et al.*, National Science Review **7**, 579 (2020).

[183] H. Wang, H. Wang, Y. Chen, J. Luo, Z. Yuan, J. Liu, Y. Wang, S. Jia, X.-J. Liu, J. Wei, *et al.*, Science Bulletin **62**, 425 (2017).

[184] M. Bai, F. Yang, M. Luysberg, J. Feng, A. Bliesener, G. Lippertz, A. Taskin, J. Mayer, and Y. Ando, Physical Review Materials **4**, 094801 (2020).

[185] M. Bai, X.-K. Wei, J. Feng, M. Luysberg, A. Bliesener, G. Lippertz, A. Uday, A. A. Taskin, J. Mayer, and Y. Ando, Communications Materials **3**, 1 (2022).

[186] B. E. Brown, Acta Crystallographica **20**, 268 (1966).

[187] T.-R. Chang, S.-Y. Xu, G. Chang, C.-C. Lee, S.-M. Huang, B. Wang, G. Bian, H. Zheng, D. S. Sanchez, I. Belopolski, *et al.*, Nature Communications **7**, 1 (2016).

[188] A. Karki, D. Browne, S. Stadler, J. Li, and R. Jin, Journal of Physics: Condensed Matter **24**, 055701 (2012).

[189] B. Tiwari, R. Goyal, R. Jha, A. Dixit, and V. Awana, Superconductor Science and Technology **28**, 055008 (2015).

[190] S. Das, A. Sirohi, L. Yadav, S. Gayen, Y. Singh, G. Sheet, *et al.*, Physical Review B **97**, 014523 (2018).

[191] J. Voerman, J. De Boer, T. Hashimoto, Y. Huang, C. Li, and A. Brinkman, Physical Review B **99**, 014510 (2019).

[192] M. R. Sinko, S. C. de la Barrera, O. Lanes, K. Watanabe, T. Taniguchi, S. Tan, D. Pekker, M. Hatridge, and B. M. Hunt, Physical Review Materials **5**, 014001 (2021).

[193] S. Ghatak, O. Breunig, F. Yang, Z. Wang, A. A. Taskin, and Y. Ando, Nano Letters **18**, 5124 (2018).

[194] A. De Cecco, K. Le Calvez, B. Sacépé, C. Winkelmann, and H. Courtois, Physical Review B **93**, 180505 (2016).

[195] H. Courtois, M. Meschke, J. Peltonen, and J. P. Pekola, Physical review letters **101**, 067002 (2008).

[196] P. Dubos, H. Courtois, B. Pannetier, F. Wilhelm, A. Zaikin, and G. Schön, Physical Review B **63**, 064502 (2001).

[197] L. Galletti, S. Charpentier, M. Iavarone, P. Lucignano, D. Massarotti, R. Arpaia, Y. Suzuki, K. Kadowaki, T. Bauch, A. Tagliacozzo, *et al.*, Physical Review B **89**, 134512 (2014).

[198] M. Endres, A. Kononov, H. S. Arachchige, J. Yan, D. Mandrus, K. Watanabe, T. Taniguchi, and C. Schönenberger, arXiv **2211.10273** (2022).

[199] P. Adroguer, C. Grenier, D. Carpentier, J. Cayssol, P. Degiovanni, and E. Orignac, Physical Review B **82**, 081303 (2010).

[200] A. J. Annunziata, D. F. Santavicca, L. Frunzio, G. Catelani, M. J. Rooks, A. Frydman, and D. E. Prober, Nanotechnology **21**, 445202 (2010).

[201] M. L. Della Rocca, M. Chauvin, B. Huard, H. Pothier, D. Esteve, and C. Urbina, Physical Review Letters **99**, 127005 (2007).

[202] A. Murphy and A. Bezryadin, Physical Review B **96**, 094507 (2017).

[203] V. Lefevre-Seguin, E. Turlot, C. Urbina, D. Esteve, and M. H. Devoret, Physical Review B **46**, 5507 (1992).

[204] F. Friedrich, P. Winkel, K. Borisov, H. Seeger, C. Sürgers, I. M. Pop, and W. Wernsdorfer, Superconductor Science and Technology **32**, 125008 (2019).

[205] D. Hazra, J. R. Kirtley, and K. Hasselbach, Applied Physics Letters **104**, 152603 (2014).

[206] H. Dausy, L. Nulens, B. Raes, M. J. Van Bael, and J. Van de Vondel, Physical Review Applied **16**, 024013 (2021).

[207] M. Faucher, T. Fournier, B. Pannetier, C. Thirion, W. Wernsdorfer, J. Villegier, and V. Bouchiat, Physica C: Superconductivity **368**, 211 (2002).

[208] L. F. Shatz and C. W. Christensen, PloS one **9**, e111643 (2014).

[209] D. S. Hopkins, D. Pekker, P. M. Goldbart, and A. Bezryadin, Science **308**, 1762 (2005).

[210] J. M. Martinis, M. H. Devoret, and J. Clarke, Physical Review B **35**, 4682 (1987).

[211] E. Turlot, D. Esteve, C. Urbina, J. M. Martinis, M. H. Devoret, S. Linkwitz, and H. Grabert, Physical Review Letters **62**, 1788 (1989).

[212] B. van Heck, F. Hassler, A. R. Akhmerov, and C. W. J. Beenakker, Physical Review B **84**, 180502 (2011).

[213] D. Frombach and P. Recher, Physical Review B **101**, 115304 (2020).

[214] J. Aumentado, M. W. Keller, J. M. Martinis, and M. H. Devoret, Physical Review Letters **92**, 066802 (2004).

[215] D. Rainis and D. Loss, Physical Review B **85**, 174533 (2012).

[216] D. J. Van Woerkom, A. Geresdi, and L. P. Kouwenhoven, Nature Physics **11**, 547 (2015).

[217] K. Hasselbach, D. Mailly, and J. Kirtley, Journal of Applied Physics **91**, 4432 (2002).

[218] A. Murani, B. Dassonneville, A. Kasumov, J. Basset, M. Ferrier, R. Deblock, S. Guéron, and H. Bouchiat, Physical Review Letters **122**, 076802 (2019).

[219] A. Bernard, Y. Peng, A. Kasumov, R. Deblock, M. Ferrier, F. Fortuna, V. T. Volkov, Y. A. Kasumov, Y. Oreg, F. von Oppen, H. Bouchiat, and S. Gueron, arXiv (2021), 10.48550/ARXIV.2110.13539.

[220] R. S. Deacon, J. Wiedenmann, E. Bocquillon, F. Domínguez, T. M. Klapwijk, P. Leubner, C. Brüne, E. M. Hankiewicz, S. Tarucha, K. Ishibashi, *et al.*, Physical Review X **7**, 021011 (2017).

[221] J. Wiedenmann, E. Bocquillon, R. S. Deacon, S. Hartinger, O. Herrmann, T. M. Klapwijk, L. Maier, C. Ames, C. Brüne, C. Gould, *et al.*, Nature Communications **7**, 1 (2016).

[222] E. Bocquillon, R. S. Deacon, J. Wiedenmann, P. Leubner, T. M. Klapwijk, C. Brüne, K. Ishibashi, H. Buhmann, and L. W. Molenkamp, Nature Nanotechnology **12**, 137 (2017).

A Fabrication recipes and parameters

This section provides detailed information about the fabrication processes of the samples used in the thesis.

A.1. Stacking of vdW materials

A.1.1. Origin of materials

Origin of van der Waals materials used in this thesis to fabricated the devices.

- WTe_2: Oak Ridge Laboratory, Oak Ridge, Tennessee 37831, USA
- hBN: T. Taniguchi et al., National Institute for Material Science, 1-1 Namiki, Tsukuba 305-0044, Japan
- Exfoliation tape: NITTO ELP-150P-LC

A.1.2. Polycarbonate (PC) mixture

Polycarbonate (PC) mixture used to build the stacking stamps.

- 0.75 g of Poly(Bisphenol A carbonate)
- 20 mL of chloroform
- mix both ingredients in a glass vial with magnetic stirrer for $> 12\,\mathrm{h}$

A.1.3. O_2 plasma cleaning of exfoliation substrates

Procedure to clean the Si/SiO_2 substrates prior to WTe_2 exfoliation in an Atto QRS-200 reactive ion etcher (RIE).

- cleavage of Si/SiO_2 waver into pieces of size $\sim 1.5\,\mathrm{cm} \times 3\,\mathrm{cm}$
- O_2 plasma: 30 W/ 0.5 Nl/h / 5 min
- immediate transfer of the substrates into the glovebox

A

A.2. CHF_3/O_2 recipe for hBN

Etching recipe for hBN, developed for the reactive-ion-etcher (RIE) Oxford Plasmalab 80 Plus.

- Gasflow: 80 sccm/4 sccm of CHF_3/O_2
- Pressure: 60 mTorr
- Power: 60 W
- Etching rate:
- Etching rates: (0.3-0.33) nm/s

A.3. E-beam lithography

A.3.1. PMMA mask for Pd bottom contacts

Procedure to fabricate a PMMA mask for Pd bottom contacts on clean Si/SiO_2 substrates.

- PMMA diluted Chlorobenzene
- Spin coating: 4000 rpm / 40 s / ramp rate 1000 rpm/s [thickness ~90 nm]
- Baking: 3 min at 180 °C
- e-beam writing: EHT = 20 kV / dose 900 µC/cm^2
- Development: (1:3) (MIBK:IPA) for 30 s; solution taken directly out of the freezer
- Blow dry with N_2

A.3.2. PMMA mask for electrical contacts

Procedure to fabricate a PMMA mask for standard metallic contacts to the vdW heterostructure.

- PMMA 950k (Allresist AR-P 672.06)
- Spin coating: 4000 rpm / 40 s / ramp rate 1000 rpm/s [thickness ~450 nm]
- Baking: 3 min at 180 °C
- e-beam writing: EHT = 20 kV / dose 450 µC/cm^2
- Development: (7:3) (IPA:H_2O) for 90 s; solution taken from standard refrigerator, development in a beaker submerged in a water ice bath
- Blow dry with N_2

A.3.3. Lift-off process

Lift-off process after metal evaporation on the PMMA mask.

- Acetone at $T = 50\,°\mathrm{C}/\ 30\,\mathrm{min}$
- Lift-off support by pipette or syringe while sample remains submerged
- Rinse with IPA
- Blow dry with N_2

A.4. Metal deposition

A.4.1. Pd bottom contacts

E-beam evaporation of Pd bottom contacts on the structured PMMA mask.

- PMMA mask structured by e-beam lithography (see A.3.1)
- E-beam evaporation of 3 nm Ti, followed by 15 nm Pd (Balzers e-beam evaporator) *

  * The thickness of Pd with 15 nm was found to provide good superconducting contact while at the same time ensures proper encapsulation of WTe_2 by hBN. A problem arising with increasing Pd thickness is that the covering hBN flake is not sealing off the area around the bottom contacts well enough, such that gaps open along the bottom contacts through which oxygen can enter and oxidize the WTe_2 flake.

- Lift-off (see A.3.3)

A.4.2. Au metal contacts

E-beam evaporation of gold (Au) contacts as a electrical connection to the vdW heterostructure through the Pd bottom contacts.

- PMMA mask structured by e-beam lithography (see A.3.2)
- E-beam evaporation of 3 nm Ti, followed by 100 nm Au (Balzers e-beam evaporator)
- Lift-off (see A.3.3)

A

A.4.3. Sputtering of Nb contacts

Sputtering of superconducting niobium (Nb) contacts in a AJA ATC Orion setup.

- PMMA mask structured by e-beam lithography (see A.3.2)
- CHF_3/O_2 etching (see A.2)**

  ** The etching process of the samples was calibrated such that the covering top hBN is safely removed and WTe_2 revealed underneath. Calibration of the etch rate for WTe_2 is more complex, as bare flakes oxidize and potentially behave differently compared to unoxidized flakes. For this reason, the remaining WTe_2 crystal on top of $PdTe_x$ after etching varies slightly between the different samples, as can also be seen from comparison of Figs. 6.3 a) with 6.6 a).
- Sputtering parameters (Ar/Nb/Pt) in AJA ATC Orion:
  - Stage position [mm]: (40/ 20/ 40)
  - Stage rotation: (off/ off/ off)
  - Ar flow [sccm]: (35/ 40/ 30)
  - BG pressure [mTorr]: (3/ 4/ 2)
  - Power [W]: (50/ 140/ 30)
  - Time: (1'/ 13'30"/ 30")
  - Thickness [nm]: (-/ 100 nm/ 4 nm)
- Lift-off (see A.3.3)

A.4.4. Sputtering of MoRe contacts

Sputtering of superconducting molybdenum-rhenium (MoRe) contacts in a AJA ATC Orion setup.

- PMMA mask structured by e-beam lithography (see A.3.2)
- CHF_3/O_2 etching (see A.2)**
- Sputtering parameters (Ar/MoRe) in AJA ATC Orion:
  - Stage position [mm]: (40/ 40)
  - Stage rotation: (off/ on)
  - Ar flow [sccm]: (35/ 30)
  - BG pressure [mTorr]: (3/ 2)

  - Power [W]: (50/ 100)
  - Time: (1'/ 6'15")
  - Thickness [nm]: (-/ 100 nm)

- Lift-off (see A.3.3)

A.4.5. Al contacts

E-beam evaporation of superconducting aluminium (Al) contacts.

- PMMA mask structured by e-beam lithography (see A.3.2)
- CHF_3/O_2 etching (see A.2)**
- Ar plasma: beam current 20 mA/ 500 V for 3 s (Balzer e-beam evaporator)
- E-beam evaporation of 100 nm Al (Balzer e-beam evaporator)
- Lift-off (see A.3.3)

B Sample preparation for STEM microscopy

The following section specifies the parameters used to extract and polish the lamellas used in the STEM and EDX analysis of chapter 6. During the study, we use two different systems to fabricate the lamella and analyse them in the STEM. While both systems work the same conceptually, we provide specific parameters here.

B.1. System 1: Swiss Federal Labs for Material Science and Technology (EMPA)

The lamella was prepared by Michael Stiefel at the Swiss Feral Laboratories for Material Science and Technology (EMPA), Dübendorf. It was used for the following figures: 6.1, 6.2, 6.3 and 6.4.

The TEM-sample preparation has been carried out in a FEI Helios 660 G3 UC FIB/SEM-system. The preparation site was covered with a double layer of platinum in order to protect the underlying layers of interest from any ion induced damage. The first Pt-layer was deposited through the process of electron induced deposition at a beam energy of 3 keV and a beam current of 800 pA. The second layer of Pt was deposited by means of ion induced deposition at a beam energy of 30 kV and a beam current of 230 pA. Cutting and polishing of the specimen was carried out in the FIB at a beam energy of 30 kV and beam currents ranging from 47 nA down to 80 pA. After reaching a sample thickness of $<$ 100 nA, the sample was cleaned first at beam energies of 5 kV (beam current 41 pA) and finally at 2 kV (beam current 23 pA). The transfer of the sample from the FIB to the TEM was conducted under an argon atmosphere. The imaging of the TEM specimen was carried out in a FEI Titan Themis 3510. The machine was operated in the STEM-mode at a beam energy of 300 keV. The EDX data was post-processed using an average filter of six pixels (pre-filter) in the Velox software. The extracted EDS line scan data was further averaged over 50 neighbouring pixels for each measurement point.

B.2. System 2: SNI Nano Imaging Lab

Two lamellas were prepared by Marcus Wyss in the Nano Imaging Lab at the Swiss Nanoscience Institute (SNI), Basel. The samples were used for the following figures: 6.5, 6.6.

B

The TEM-sample preparation was carried out in a FEI Helios NanoLab 650 DualBeam-system. The preparation of the lamella was similar to the description in Sec B.1. The imaging of the TEM specimen was carried out in a JEOL JEM-F200. The machine was operated in the STEM-mode at a beam energy of 200 kV. The EDX data were analysed with the Analysis Station software, thereby the data has not been post-processed.

Curriculum Vitae

Martin Alexander Endres
Born on 22nd May 1994 in Schweinfurt (Germany)

Education

11/2018–10/2022 **PhD in experimental physics at the University of Basel, Switzerland**

- Dissertation in the group of Prof. Dr. C. Schönenberger
  "WTe_2: Potential candidate for topological superconductivity"

08/2015–09/2018 **Master of Science in Nanostructure Technology at the University of Würzburg, Germany**

- Master thesis in the group of Prof. Laurens W. Molenkamp, supervision by Prof. Hartmut Buhmann
  "Manipulation of the electrostatic landscape in order to improve the QSH edge channel transport in HgTe"

08/2015–09/2016 **Exchange year at the University of New Mexico, Albuquerque, USA**

- Master studies in physics
- Stipend awarded by the German Academic Exchange Service (DAAD)

10/2012–08/2015 **Bachelor of Science in Nanostructure Technology at the University of Würzburg, Germany**

- Bachelor thesis in the group of Prof. Laurens W. Molenkamp, supervision by Prof. Hartmut Buhmann
  "Untersuchungen der Kristallqualität und der Oberflächenrauigkeit MBE-gewachsener II-VI Heterostrukturen mittels XRD und AFM"

07/2012 **Abitur** at the Alexander-von-Humboldt-Gymnasium, Schweinfurt, Germany

Positions

11/2018–now	*Teaching assistant for physics at the University of Basel, Switzerland*
09/2017–10/2018	*Scientific assistant at "IJF Initiative Junge Forscherinnen und Forscher e.V."*
10/2016–07/2017	*Teaching assistant for physics at the University of Würzburg, Germany*
08/2015–07/2016	*Teaching assistant for physics at the University of New Mexico, Albuquerque, USA*

Publications

- *"Transparent Josephson Junctions in Higher-Order Topological Insulator WTe_2 via Pd Diffusion"*
  Martin Endres, Artem Kononov, Michael Stiefel, Marcus Wyss, Hasitha Suriya Arachchige, Jiaqiang Yan, David Mandrus, Kenji Watanabe, Takashi Taniguchi and Christian Schönenberger
  Phys. Rev. Materials **6**, L081201 (2022)

- *"Current-Phase Relation of a WTe_2 Josephson junction"*
  Martin Endres, Artem Kononov, Hasitha Suriya Arachchige, Jiaqiang Yan, David Mandrus, Kenji Watanabe, Takashi Taniguchi and Christian Schönenberger
  arXiv.2211.10273 (2022)

- *"Superconductivity in type-II Weyl-semimetal WTe_2 induced by a normal metal contact"*
  Artem Kononov, **Martin Endres**, Gulibusitan Abulizi, Kejian Qu, Jiaqiang Yan, David G. Mandrus, Kenji Watanabe, Takashi Taniguchi and Christian Schönenberger
  Journal of Applied Physics **129**, 113903 (2021)

- *"Approaching Quantization in Macroscopic Quantum Spin Hall Devices through Gate Training"*
  Lukas Lunczer, Philipp Leubner, **Martin Endres**, Valentin L. Müller, Christoph Brüne, Hartmut Buhmann and Laurens W. Molenkamp
  Phys. Rev. Lett. **123**, 047701 (2019)

Talks

- *Josephson Effect in Higher-Order Topological Insulator WTe_2* ***(invited talk)***
  Topological Insulator Devices and Materials Workshop, NPL, London (United Kingdom), June 2022

- *Josephson Junctions in WTe_2*
  QCQT Lunch Seminar, University of Basel, Basel (Switzerland), May 2022

- *Current Phase Relation in WTe_2*
  Graphene Workshop Basel 2021, Basel (Switzerland), November 2021

- *Topological properties in van der Waals heterostructures based on WTe_2*
  QSIT Junior Meeting, Flumserberg (Switzerland), June 2019

Poster Contributions

- *"Current Phase Relation of WTe_2 Josephson Junctions"*
  MESO School 2021, Cargèse, Coarse (France), September 2021

Acknowledgements

It goes without saying that none of the work in this thesis would have been possible without the help of many wonderful people. In the past four years, I did not only have the chance to work in an extremely exciting field of physics, but also to get to know so many great people and form friendships. I would like to use the following lines to express my gratitude for all your support and thank you.

First, I would like to thank my supervisor Prof. Christian Schönenberger for providing me the opportunity to work with him on the project of this thesis. With your leading style, the fascination for physics and the constant support, you create a inspirational work environment. From the first day on, I enjoyed the cordial atmosphere in the group, which is for sure also created through the social group trips each year. Thank you for all your support, expertise and guidance through all these years.

I would like to express my gratitude to Prof. Yoichi Ando, Prof. Thomas Schäpers and my co-supervisor Prof. Patrick Maletinsky. Thank you that you have agreed to be part of the doctoral committee. It is an honor that you have taken your time to evaluate my thesis.

I can not express enough gratitude to Dr. Artem Kononov. You have been my daily mentor over the past four years and I could not have asked for a better one. You taught me everything that is summed up by this thesis and so much more. I admire, that you always keep an analytical view on problems, and your fundamental understanding of the physics. Not only have we worked together, but were also race biking in the country side around Basel. I hope your knee is recovering soon and we can go on many more bike rides together.

Special thanks go to Dr. Paritosh Karnatak and Dr. David Indolese. You both have been colleague, supervisor and friend in one. I was lucky to collaborate with both of you and I am looking forward to do so in the future. Thank you both for reading through this thesis. Besides work, I have enjoyed our free time together a lot. Only recently have we managed to become the “fastest physicists on the water” at the famous boat race of Möhlin, that was organized by David.

Thank you to our collaborators for the STEM study Michael Stiefel and Dr. Marcus Wyss. The work would not have been possible without your skills operating the FIB and STEM.

This work would also not have been possible without the many people across the department that work continuously to keep everything running. Thank you Barbara Kammermann for managing all administrative tasks in our group. No matter how complex and chaotic the bureaucracy might have been, you took care of it. Thank you Dr. Laurent Marot, who was in charge of our cleanroom and fabrication facilities and whom I have worked with a lot over the years. Thank you Dominik Sifrig for constant supply of helium and nitrogen to conduct the measurements.

Special thanks go to my dear friend Dr. Christian Jünger. You have guided me through the years and independent of the topic, I can always count on your advice. After I moved to Basel, you made this new place a home. Thank you for all the great time together, be it in the mountains or down at the river. I am looking forward to seeing again soon!

Thank you so much to my friends Carlo Ciaccia, Olivier Faist, Roy Haller, Matthijs Hermans and Hinrich Mattiat for the great bike rides and the delicious dinners we cooked together throughout the years.

A PhD is tough, but it becomes so much easier with great colleagues and BBQs, ice cream breaks and evening drinks. Thank you to all current and former members of the MESO group, with whom I was able to spend time with over the last years: Prasanta Kumbhakar, Mehdi Ramenzani, Luk Yi Cheung, Ian Sampaio, Rounak Jha, Zarina Mingazheva, Alessia Pally, Deepankar Sarmah, Jann Ungerer, Blessonsam Varghese, Han Zheng, Gulibusitan Abuliz, Arunav Bordoloi, Gergö Fülöp, Simon Zihlmann, Libin Wang, Lujun Wang, Frederick Thomas, Malin Nilsson, Nadine Leisgang, Joost Ridderboos, Lukas Gubser and Jan Overbeck.

I would also like to thank all my friends that have accompanied me through the journey of physics studies. Thank you Bernd, Yannik, Manuel, Tim, Ferdinand, Tim, Milena, Maximilian and Johannes for the great time. I will never forget our years together during the Bachelor and Masters studies. I could not have done it without you!

Thank you also to Rachel Zurbriggen, who was so kind to proofread this thesis for language errors and, I believe, hundreds of missing commas.

Finally, I would like to thank my family for supporting me over all the years. Mum and dad, you are always giving everything for Vicky and me. This thesis would not have been possible without you.

Thank you all!